Energy Technology Division
Energy Technology Division
Energy Technology Division
Energy Technology Division
Energy Technology Division
Energy Technology Division
Energy Technology Division
Energy Technology Division
Energy Technology Division
Energy Technology Division
Energy Technology Division
Energy Technology Division
Energy Technology Division
Energy Technology Division
Energy Technology Division
Energy Technology Division
Energy Technology Division
Energy Technology Division
Energy Technology Division
Energy Technology Division
Energy Technology Division
Energy Technology Division
Energy Technology Division
Energy Technology Division
Energy Technology Division
Energy Technology Division
Energy Technology Division
Energy Technology Division
Energy Technology Division
Energy Technology Division
Energy Technology Division
Energy Technology Division
Energy Technology Division
Energy Technology Division

ANL-03/33

Study of Metal Dusting Phenomenon and Development of Materials Resistant to Metal Dusting:

Final Report

K. Natesan and Z. Zeng
Energy Technology Division

December 2003

Argonne National Laboratory, Argonne, Illinois 60439
operated by The University of Chicago
for the United States Department of Energy under Contract W-31-109-Eng-38

Energy Technology Division
Energy Technology Division
Energy Technology Division
Energy Technology Division
Energy Technology Division
Energy Technology Division
Energy Technology Division
Energy Technology Division

Argonne National Laboratory, a U.S. Department of Energy Office of Science laboratory, is operated by The University of Chicago under contract W-31-109-Eng-38.

Available electronically at http://www.osti.gov/bridge/

Available for a processing fee to U.S. Department of Energy and its contractors, in paper, from:

U.S. Department of Energy
Office of Scientific and Technical Information
P.O. Box 62
Oak Ridge, TN 37831-0062
phone: (865) 576-8401
fax: (865) 576-5728
email: reports@adonis.osti.gov

ANL-03/33

ARGONNE NATIONAL LABORATORY
9700 South Cass Avenue
Argonne, Illinois 60439-4838

Study of Metal Dusting Phenomenon and Development of Materials Resistant to Metal Dusting

FINAL REPORT

K. Natesan and Z. Zeng
Energy Technology Division

December 2003

Work supported at Argonne National Laboratory

by

THE U.S. DEPARTMENT OF ENERGY
Office of Industrial Technologies
Project Manager: C. Sorrell

CONTENTS

FIGURES

TABLES

ABSTRACT

The deposition of carbon from cabonaceous gaseous environments is prevalent in many chemical and petrochemical processes such as reforming systems, syngas production systems, iron reduction plants, and others. One of the major consequences of carbon deposition is the degradation of structural materials by a phenomenon known as "metal dusting." There are two major issues of importance in metal dusting. First is formation of carbon and subsequent deposition of carbon on metallic materials. Second is the initiation of metal dusting degradation of the alloy. Details are presented on a research program that has been conducted at Argonne National Laboratory to study the metal dusting phenomenon from a fundamental scientific base involving laboratory research in simulated process conditions and field testing of materials in actual process environments. The project has participation from the U.S. chemical industry, alloy manufacturers, and the Materials Technology Institute, which serves the chemical process industry.

PROJECT DESCRIPTION

Project Title: Study of Metal Dusting Phenomenon and Development of Materials Resistant to Metal Dusting

Principal Investigators: K. Natesan (Argonne National Laboratory)
K. Baumert (Air Products and Chemicals Inc.)

ANL Participants in the Project: K. Natesan, Z. Zeng, W. K. Soppet, D. L. Rink, A. Purohit, V. Maroni, and M. Grimsditch

Organizations Participating in the Project:
Materials Technology Institute
Air Products and Chemicals Inc.
ExxonMobil Chemical Company
DuPont Chemical Company
Allied Signal (part of Honeywell)
Haynes International
AvestaPolarit
Sandvik Steel
Duraloy Technologies
Special Metals
Krupp VDM
Schmidt & Clemens
Alon Surface Technologies
MetalTek International
Spectrum Metals
Allegheny Ludlum

OBJECTIVES

The overall objective of this project is to study metal dusting phenomenon from a fundamental scientific base involving laboratory research in simulated process environments and field-testing of materials in actual process environments with participation from the U.S. chemical industry, alloy manufacturers, and the Materials Technology Institute (MTI), which serves the chemical process industry. Another objective is to develop a user-friendly knowledge base of materials/corrosion information for application in the chemical and petrochemical industries.

The effort at Argonne National Laboratory (ANL) involves testing off-the-shelf and surface-engineered materials in simulated process environments, developing long-term data on candidate materials as a function of key process variables, and gaining a fundamental understanding of the metal dusting and associated carburization phenomenon. As part of this effort, alloy manufacturers contributed materials for both laboratory and field testing, participated in a Steering Committee for the project, and conducted in-house evaluation of materials.

APPROACH

The technical approach involved several steps conducted either sequentially or in parallel and included participation of MTI members and Argonne National Laboratory in the organization of the work plan and in the conduct of the proposed research to address the metal dusting issue. MTI member companies supplied their in-house metal-dusting data collected over the years and made complementary exposures of candidate alloys for evaluation and assessment.

The approach involved characterization, using thermodynamic modeling, of environments prevalent in several process streams in terms of their chemical activities for carbon, oxygen, and other elements. The results were used to assess the chemical potential and temperature windows for metal dusting to initiate and propagate in metallic materials. The thermodynamic assessment established the consequences of equilibrium and nonequilibrium gas chemistries on the metal dusting process.

The corrosion behavior of commercial alloys in chemical process industries was evaluated to identify conditions in which metal dusting occurs in practice. MTI has collected metal dusting data (both proprietary and published data from the open literature) for several materials from its member companies. This information was used to establish the effects of alloy chemistry, temperature range, pressure range, exposure time, and exposure environment on the corrosion process by metal dusting.

Bench-scale laboratory experiments were conducted at Argonne with candidate commercial alloys, developmental alloys, and surface-engineered materials, including coatings. Surface modification included development of oxide scales on candidate alloys by exposures in air and environments with low oxygen partial pressure (low-pO_2). Surface engineering included

development of pack diffusion coatings and claddings. Experiments were conducted in a wide range of gas chemistries and temperatures that encompass the environments prevalent in various process systems, such as in reformers for the production of hydrogen, ammonia, and methanol. Results were used to establish the conditions for the onset of metal dusting and to evaluate the influence of alloy chemistry on the occurrence of metal dusting. The effect, if any, of system pressure was evaluated by performing several short- and long-term experiments in a high-pressure test facility that was designed and constructed for this program.

PROJECT TASKS

Project research focused on the following tasks:

- Characterization of chemical process environments using computer modeling of gas phase reactions
- Corrosion testing of off-the-shelf candidate alloys in simulated metal dusting environments
- Development of surface-engineered materials based on results from corrosion tests
- Evaluation of the role of system pressure in the initiation of corrosion/metal dusting of materials
- Corrosion testing on surface-engineered materials in simulated chemical environments over a wide temperature and pressure range
- Development of a database on metal dusting and corrosion performance of materials

BACKGROUND

The predominant process for hydrogen production is steam reforming of light hydrocarbons e.g., natural gas, liquefied petroleum gas, naphtha, or refinery off-gases. This process has been used extensively in the past for hydrogen production and is expected to continue in most of the installations required to meet the increasing demand for hydrogen in the future. The demand for hydrogen is growing in many industries. Refineries, in particular, must increase hydrogen use to make products acceptable to the environment and to limit production of very heavy resid. Refiners consider hydrogen a utility, and they emphasize availability, trouble-free response to changing demand, and low-cost investment.

Production capacity in hydrogen plants may range from <100 $N \cdot m^3/h$ to $>100{,}000$ $N \cdot m^3/h$. For larger capacities, from 1000 $N \cdot m^3/h$ and upward, hydrocarbons are the predominant feedstocks. The production processes may be partial oxidation or steam reforming; for both types of processes, the primary process step is followed by shift conversion and final purification of product hydrogen.

Production of synthesis gas (mixtures of carbon monoxide and hydrogen) is an important first step in the manufacture of numerous chemicals. The most common process for producing synthesis gas is steam reforming, where hydrocarbons are converted by reaction with steam over a nickel catalyst at high temperatures. The synthesis gas from the steam reformer is purified in order to meet the requirements of the downstream process. It can be separated into pure H_2, pure CO, H_2/CO mixtures, etc. Pure CO is required for the production of isocyanates, polycarbonates, and acetic acid, while for example, synthesis of oxo-alcohols requires an H_2/CO mixture with a molar ratio close to 1. By decreasing the steam/carbon ratio and by increasing the outlet temperature from the reformer furnace, great savings can be obtained in feedstock consumption and in investment.

The steam reformer is the heart of the unit for production of synthesis gas. In the steam reformer, hydrocarbon feedstock is reacted with steam to synthesis gas by the reactions:

$$C_nH_m + n\ H_2O = n\ CO + (n + m/2)\ H_2 \quad (1)$$

$$CH_4 + H_2O = CO + 2H_2 \quad (2)$$

$$CO + H_2O = CO_2 + H_2 \quad (3)$$

All higher hydrocarbons ($n \geq 2$) are completely and irreversibly converted by the first reaction, while in the next two reactions, the strongly endothermic methane-reforming reaction (2) and the exothermic shift reaction (3) are close to equilibrium in the outlet of the steam reformer. The reactions take place over a nickel catalyst placed inside metal tubes. The tubes are arranged in a furnace where burners firing on the outside of the tubes supply the heat.

Metal dusting is a catastrophic corrosion phenomenon that leads to the disintegration of structural metals and alloys into dust composed of fine particles of the metal/alloy and carbon. This phenomenon has been observed in the chemical and petrochemical industries, in reformer and direct-reduction plants, in processes that generate syngas, and in other processes where hydrocarbons or other strongly carburizing atmospheres are present. Failures have been reported in ammonia plants since reduced energy requirements result in a lower steam/H_2 ratio, whereas CO/CO_2 ratios have tended to increase.

Metal dusting is a process of highly accelerated material wastage that is preceded by the saturation of a material with carbon. The phenomenon is typified by the disintegration of a material (iron- or nickel-base) to a mixture of carbon dust, metal particles, and possibly oxides and carbides. This is usually a localized form of attack, resulting in pits and grooves. Metal dusting occurs at intermediate temperatures of 400-800°C, but this type of corrosion is possible at any temperature at which the carbon activity (a_C) in the gas phase is >1. Such high carbon activities are prevalent in certain locations in several chemical processes, such as methanol production, hydrocarbon and ammonia synthesis, hydrogen production, and syngas generation. Several of these chemical systems have reported metal/component failures by metal dusting. For

CO-H_2-H_2O mixtures, carbon activity, which is the thermodynamic driving force for metal dusting, increases with decreasing temperature. Carbon activity values >1000 can be obtained at 500°C in several of the process streams.

Materials can be protected against metal dusting by adding sulfur-containing compounds, such as H_2S, to the process gas. Sulfur in the gas "poisons" the metal surfaces and prevents both carbon ingress and graphite nucleation. However, in many catalytic processes, sulfur-bearing substances cannot be injected since they deactivate the catalysts. To prevent material wastage under such conditions, an appropriate material with high resistance to metal dusting is needed.

Important reactions, which can occur in the typical metal dusting environment, are:

$$2CO = CO_2 + C \quad (4)$$

$$H_2 + CO = H_2O + C \quad (5)$$

$$H_2O + CO = CO_2 + H_2 \quad (6)$$

$$H_2O + CH_4 = CO + 3H_2 \quad (7)$$

Reactions (4) and (5) can produce carbon; Reaction (6) deals with water-gas shift, and Reaction (7) with methane-steam reforming. The dominant reaction in a chemical process can be any one of the above reactions or a combination of them, and the carbon activity will be influenced by the dominant reaction, process temperature, and pressure. Most of the structural materials based on Fe, Ni, and Co are susceptible to this type of degradation even though the conditions of temperature, environmental chemistry, and incubation and kinetic factors for this occurrence may be different.

In a hydrogen plant, the major process components are the fuel gas reformer, process gas boiler, and high- and low-temperature shift reactors. The syngas from the reformer contains various amounts (in vol%) of gases, such as H_2 (60), CO (15), CO_2 (5), CH_4 (10), steam (10), and trace amounts of other compounds. It is produced primarily by steam reforming and partial oxidation of hydrocarbons at temperatures of 800-1400°C. The hot gases are contained in refractory-lined equipment and quenched to about 300°C in a waste-heat boiler or cooled by direct injection of water to the process stream. Most processes deliberately avoid transferring heat through the 800-400°C range because metal dusting occurs at these temperatures, and at present, no alloy can resist this type of corrosion over the long term. Consequently, the energy in high-temperature syngas is not recovered in an efficient manner.

Another example relevant to metal dusting is the formation of filamental coke in several petrochemical processes, which eventually leads to failure of heater alloys by metal dusting. The coke formation involves several sequential steps, such as dissociative chemisorption of hydrocarbon, stepwise dehydrogenation, surface and volume diffusion of carbon, carbide precipitation and transport under a temperature gradient, and regeneration of catalyst or decoking under oxidizing conditions. Further, the process entails cyclic deposition and decoking. Some

models have been proposed in the literature for coke formation, which involves dissociative chemisorption and stepwise dehydrogenation leading to adsorption of C and H on the surface sites on the catalyst, diffusion of carbon through the metal and precipitation on the grain boundaries or at the metal/support interfaces, lifting of metal crystallites from the surface of the catalyst, and transport of crystallites to the top of the growing filaments.

Alternatively, C species may react on the surface to develop an encapsulating film, leading to the deactivation of the catalyst. Competition between C accumulation on the surface and C diffusion away from the active sites determines whether the catalyst becomes deactivated or not. This is determined by the gas composition, hydrogen pressure, and temperature.

1. GAS CHEMISTRY AND CARBON ACTIVITY

Before initiation of experiments, gaseous environments that are prevalent in chemical process industries were characterized by computer modeling of gas-phase reactions under both equilibrium and nonequilibrium conditions. To evaluate the role of gas composition on metal dusting rate of alloys, specimens were exposed to several gas mixtures (see Table 1.1) of varying composition. Gas mixtures 1, 2, and 3 show the composition of the effluent from hydrogen and ammonia reformers. Figure 1.1 shows the compositions of gas mixtures in terms of CO/CO_2 and H_2O/H_2 ratios.

Calculations were made to evaluate carbon activities for different gas mixtures as a function of temperature at atmospheric pressure (14.7 psia) and at plant system pressures. Carbon deposition process can be influenced by two possible reactions, as follows:

$$CO\ (g) + H_2\ (g) = C + H_2O\ (g) \qquad \text{Reaction 1}$$

$$2CO\ (g) = C + CO_2\ (g) \qquad \text{Reaction 2}$$

Since the gas composition is maintained fairly constant during the passage through the waste-heat boiler, either Reaction 1 or Reaction 2 may dictate the carbon activity in the stream at different temperatures. If it is determined by Reaction 1, the carbon activity will be directly proportional to H_2 and CO partial pressures and inversely proportional to H_2O partial pressure. On the other hand, if carbon activity is determined by Reaction 2, then it will be directly proportional to the square of the CO partial pressure and inversely proportional to CO_2 partial pressure. In addition, if gas phase equilibrium does prevail, albeit at high temperatures and/or for long residence times, then the calculated carbon activity value will be the same (irrespective of Reaction 1 or 2) since thermodynamically the gas composition will adjust to give the most stable (lowest free energy) composition. Therefore, carbon activity was calculated as a function of temperature from 496°C (or 925°F) to the maximum test temperature and for 1 atm to the maximum test pressure for various gas mixtures (Table 1.1), assuming that Reaction 1 or 2 is dominant and the gas phase is in thermodynamic equilibrium.

Carbon activities were calculated for several of the gas mixtures, and their impact on metal dusting was reported earlier (Natesan 2002). Figures 1.2-1.8 show the carbon activity of several gas mixtures as a function of temperature. Carbon activity calculated using Reaction 1 and 2 decreases with increasing temperature, but increases with an increase in system pressure. Figure 1.1 shows that the carbon activity, calculated using Reaction 1, varies from 2 to 149 for the gas mixtures used in our study at 593°C. The carbon activity of Gas 10 at 14.2 atm (210 psi) is similar to the carbon activity of Gas 11 at 1 atm at 593°C, and these two gas mixtures were used to evaluate the effect of system pressure on metal dusting at similar carbon activity.

Table 1.1 Chemical composition (in mole %) of gas mixtures used in the metal dusting study.

Gas	H_2	CO	CO_2	H_2O	CH_4	N_2
1	43.8	7.2	5.7	39.2	4.1	-
2	52	18	5.6	23	1.1	-
2b	66.2	23	7.1	2.3	1.4	-
3	36.3	8.4	5.6	35	0.2	15
4	74.2	17.5	8.3	0	-	-
5	72.2	17.6	8.3	1.96	-	-
6	77.2	12.7	10.1	0	-	-
7	25.25	70	4	0.007	-	-
8	71.4	11.3	17.4	0	-	-
9	71	11.7	17.3	0	-	-
10	53.4	18.4	5.7	22.5	-	-
11	79.5	18.2	-	2.3	-	-
12	75.4	6.2	18.4	-	-	-
13	71.0	2.6	26.4	-	-	-
14	40	45	5	10	-	-
15	20	65	5	10	-	-
16	40	25	25	10	-	-
17	20	74.5	5	0.5	-	-

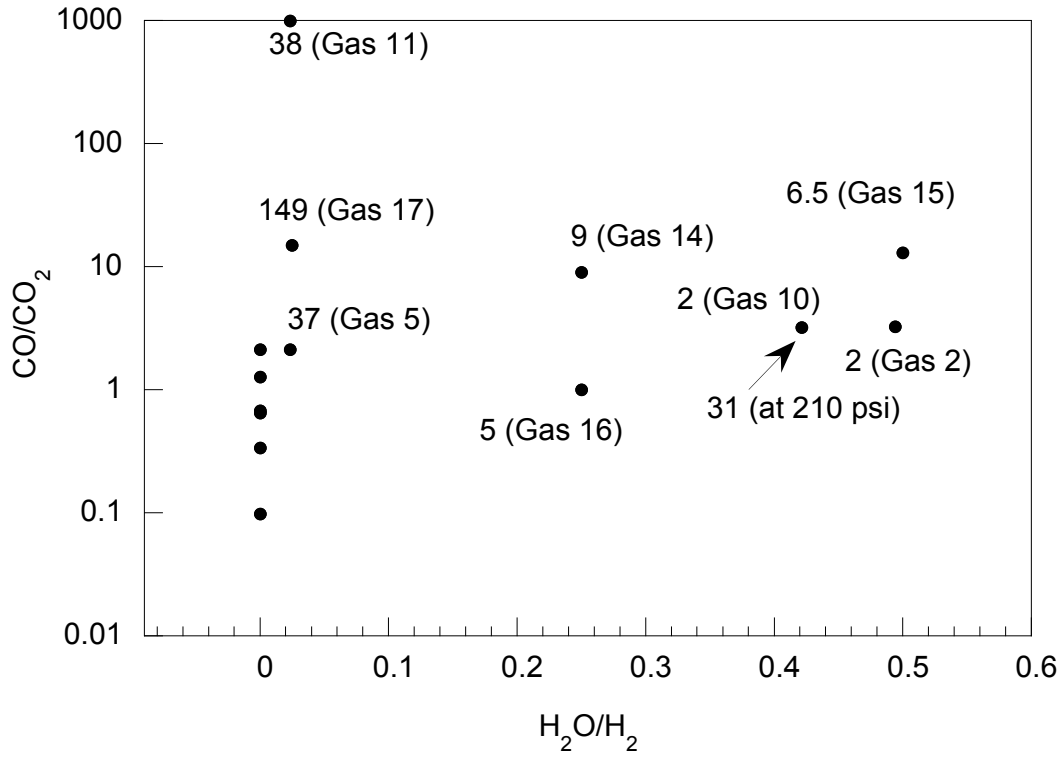

Figure 1.1. Chemical composition and carbon activity for gas mixtures that were used in metal dusting study. Carbon activity was calculated from reaction CO (g) + H_2 (g) = C + H_2O (g) at 593°C.

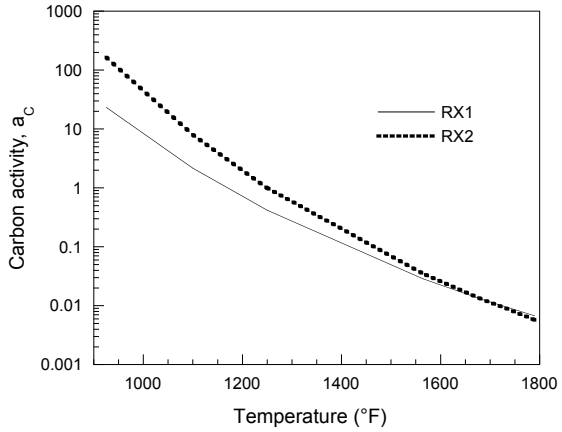

Figure 1.2. Carbon activity of Gas 10 as a function of temperature at 1 atm.

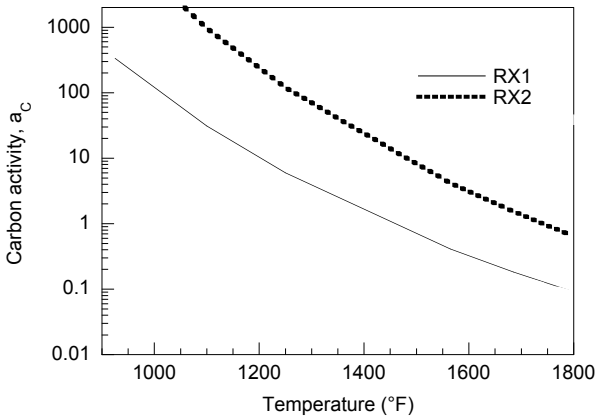

Figure 1.3 Carbon activity of Gas 10 as a function of temperature at 14.2 atm.

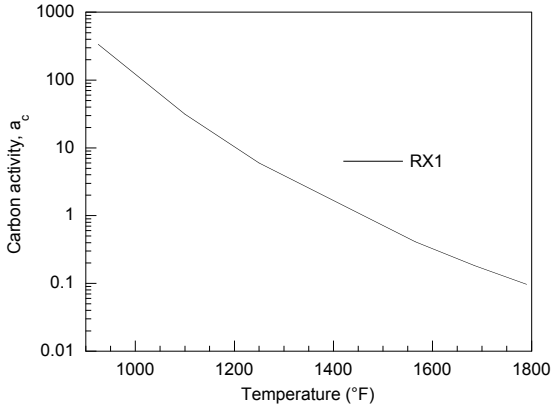

Figure 1.4. Carbon activity of Gas 11 as a function of temperature at 1 atm.

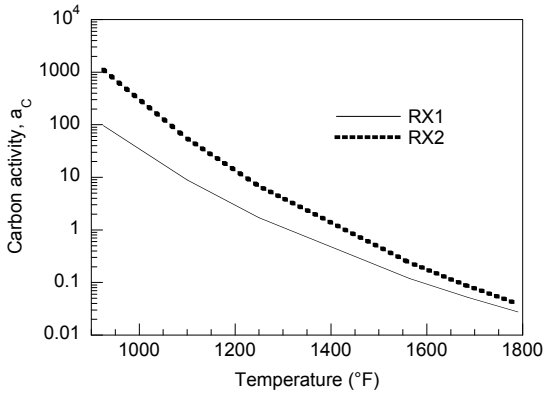

Figure 1.5. Carbon activity of Gas 14 as a function of temperature at 1 atm.

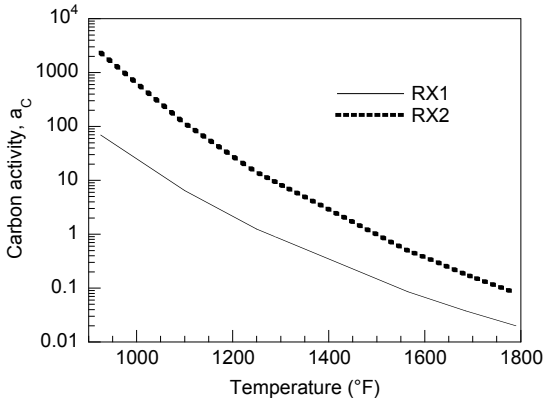

Figure 1.6. Carbon activity of Gas 15 as a function of temperature at 1 atm.

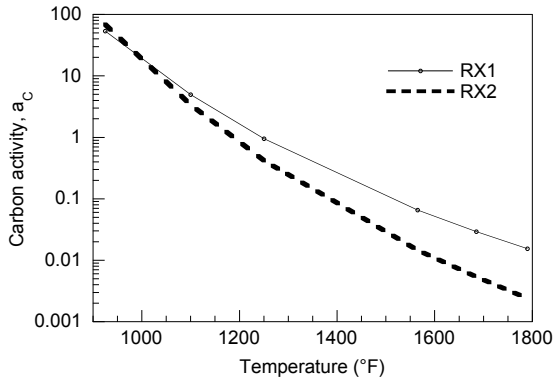

Figure 1.7. Carbon activity of Gas 16 as a function of temperature at 1 atm.

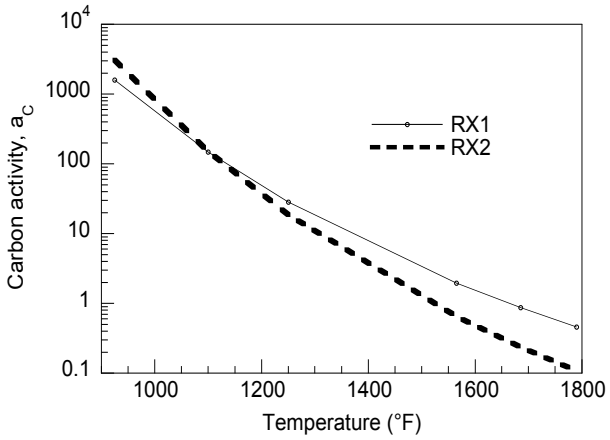

Figure 1.8. Carbon activity of Gas 17 as a function of temperature at 1 atm.

2. EXPERIMENTAL PROGRAM

2.1 Equipment Description

In all, five experimental systems were used in the metal dusting experiments. Two existing systems at ANL were modified to accommodate the requirements of the program. Each of the modified systems consisted of a horizontal, tubular, high-temperature furnace capable of operation up to 900°C. The reaction chamber, with gas inlet/outlet fittings, was fabricated from quartz and positioned within the furnace chamber. The ends of the reaction chamber had specially designed flanges with O-ring seals. A chromel-alumel thermocouple, inserted from one end of the reaction chamber, was used to monitor the specimen temperature. Specimens were suspended from quartz rods held on the top of a high-purity alumina boat. The specimens and the boat were positioned in the constant-temperature section of the reaction chamber. High-purity gases such as CO, CO_2, CH_4, and H_2 were procured and piped into the reaction chamber through flow meters to obtain the desired composition. In some experiments, H_2 gas was bubbled through a water bath to saturate the H_2 with water prior to entering the reaction chamber. Upon completion of the experiments, the specimens and the carbon accumulated on the specimens and in the boat were removed for detailed microstructural, X-ray, and Raman analysis.

While the two systems described above enabled study of the key variables in metal dusting research, additional facilities were needed for long-term testing of metallic alloys, surface-engineered materials, and coatings. For this purpose, three new systems were designed and assembled in a metal dusting research laboratory. Figure 2.1 shows a schematic diagram for the three test facilities set up for metal dusting experiments. The three environmental exposure test fixtures were positioned horizontally on a laboratory bench top in a staggered linear arrangement with a common gas supply. Each test fixture consisted of a quartz retort chamber (74-cm length, 5-cm OD, 0.32-cm thick), which was centered in a 30-cm-diameter resistive heating furnace. A Barber-Coleman Model 560 three-mode controller was used to control the furnace temperature. Type 316 stainless steel (SS) flange caps with an O-ring seal were used to close the ends of the quartz retort tube. The flange caps provided port fittings for the gas flow, steam/vapor preheater, and ceramic thermowells used for measurements of specimen temperature. Figure 2.2 shows a schematic diagram for the furnace assembly and gas flow arrangement used for the metal experiments.

The gas that flowed through the retort chamber had various ratios of H_2, CH_4, CO, CO_2, and steam/water vapor. Laboratory-grade compressed gases were supplied from AGA Gas Co. in industry standard 1A size (136 atm and 4.3 m^3 internal volume) cylinders. Each gas was piped to the reaction chamber through a low-pressure manifold line that was fed from a two-stage gas pressure-reducing regulator with a flash arrestor and a solenoid shut-off valve. The solenoid valves were controlled by a gas-leak detection system manufactured by International Sensor Technology Co. Overhead sensors that are selective to H_2, CH_4, CO gases were used to

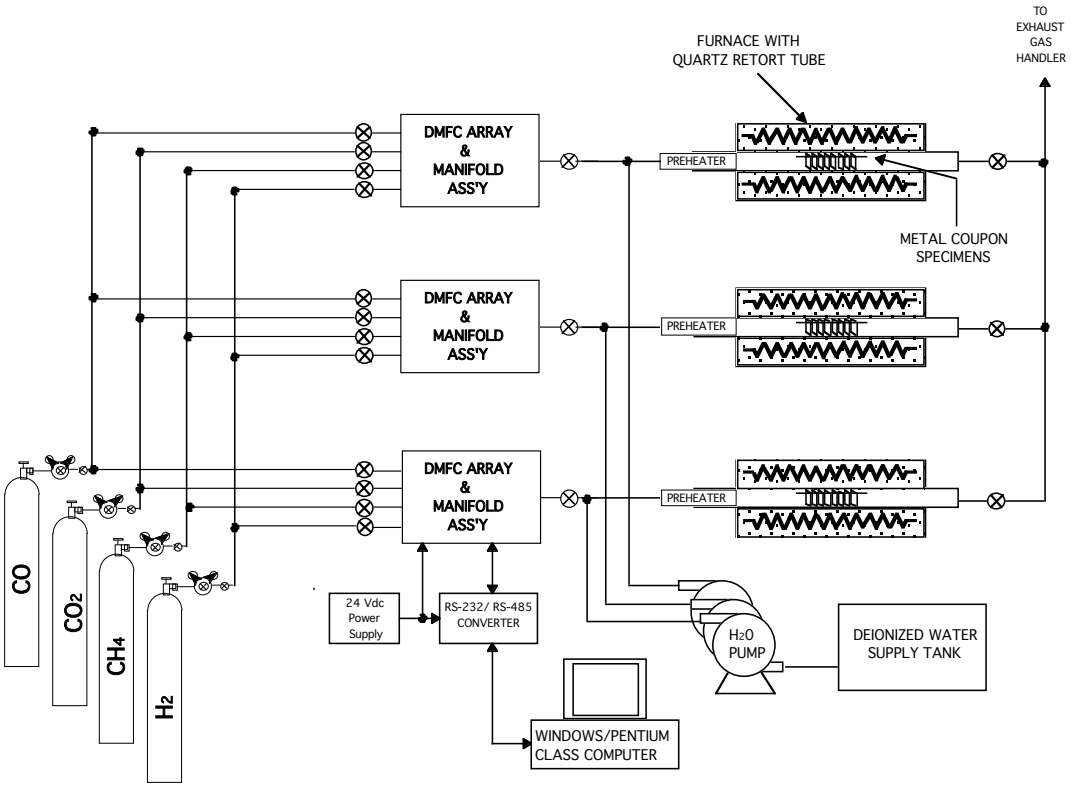

Figure 2.1. Schematic of three atmospheric test facilities used for metal dusting experiments.

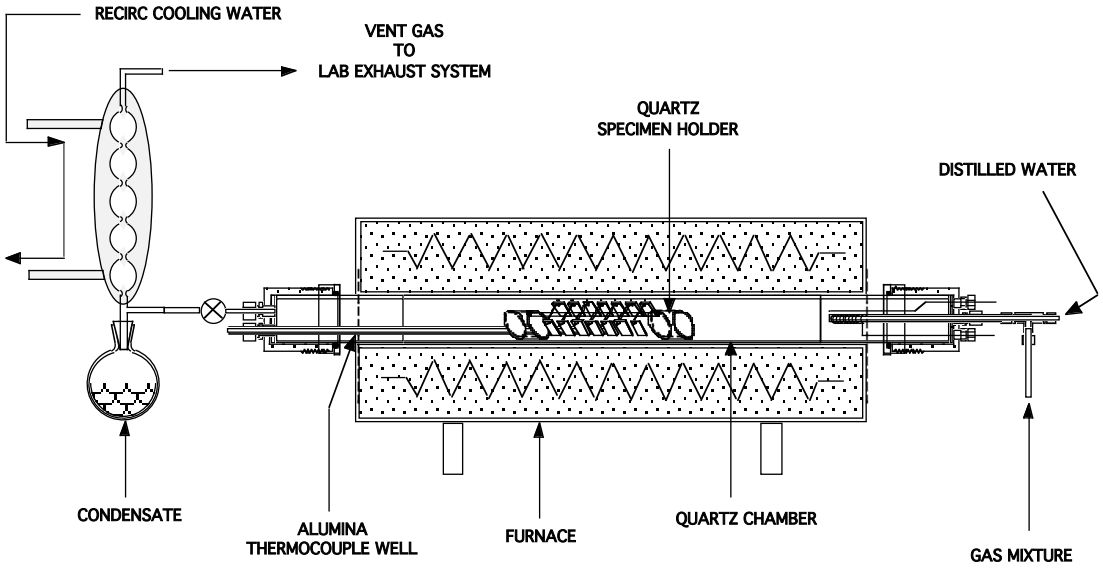

Figure 2.2. Schematic of furnace assembly and gas flow arrangement used for metal dusting experiments.

Detect gas leaks. In the event of a leak detected above a user-selected threshold by any of the sensed gases, the detection system closed the solenoid valves for all gases.

Gases from the low-pressure manifold lines were supplied to respective individual Brooks model 5850S digital computer-controlled mass flow control (DMFC) valves. Figure 2.3 shows a schematic diagram of the steam and gas flow scheme used for the metal dusting experiments. The output from each mass flow controller combined into a central manifold tube that connects to the steam/vapor preheater assembly at the input cover flange for the retort tube. The steam/vapor preheater had a coaxial-design mixing chamber enabling the water vapor to be entrained by the flowing gas mixture prior to passing the preheat element. The gas mixture flow rate was typically 200-400 cm^3/min (STP), and the water flow rate was 1-5 cm^3/h. The preheat temperature was maintained with a Love Controls Model 16A three-mode process controller. Distilled water was supplied to the preheat mixing chamber by a Watson-Marlow Model MPL micro-metering pump that was fed from a 20 L polycarbonate carboy. The micro-metering pump was based on peristaltic action, and the flow rate was adjusted by varying the rotational speed of the roller cam and/or the diameter of the flexible tubing. The gas-steam mixture flowed past the alloy test specimens to the exit port at the rear flange cap. After the gas-steam mixture exited the retort, it was passed through a chilled water pyrex condenser to collect water vapor for future measurement, while the remaining gas mixture was vented to a room exhaust vent handler

Alloy test specimens were mounted on a quartz specimen tree (see Fig. 2.4) that was centered in the heat zone of the retort chamber. Metal-dusting experiments were conducted under isothermal conditions at temperatures between 800 and 1300°F (427 and 704°C). A chromel-alumel thermocouple controlled the furnace temperature. The test temperature and the precision of its control are important to the reproducibility and usefulness of the results. An indicating controller calibrated for the control thermocouple maintained the furnace temperature. Specimen temperature was monitored with a second, sheathed chromel-alumel thermocouple inserted into the reaction chamber in the vicinity of the specimens. The outputs of the monitoring and control thermocouples were calibrated over the temperature range of interest, so that if the monitoring thermocouple became inoperative due to corrosion, the control thermocouple was used during continuation of the test. The multicomponent gas environment for the metal dusting program consisted of CO, CO_2, H_2, CH_4, and H_2O. The actual composition of the gas mixture had a wide enough range to establish carbon activity of ≈0.5 to ≈100 at the temperatures and pressures of interest. The exposure time periods in different experiments ranged between 5 and 1000 h, depending on the objective of the test.

Figure 2.5 shows a system that was built to conduct experiments at system pressures up to 600 psi (41 atm). The system consisted of a horizontal, tubular, high temperature furnace capable of operation up to 900°C. The reaction chamber, with gas inlet/outlet fittings, fabricated from alumina and/or quartz was positioned within a pressure vessel made of a high-temperature heat-resistant alloy (16-mm ID, 50-mm OD, 500-mm long). A chromel-alumel thermocouple was inserted into the pressure vessel to monitor the specimen temperature. Specimens were suspended from an alumina rod and were positioned in the constant-temperature section of the

tubular furnace. High-purity gases such as CO, CO_2, CH_4, and H_2 were piped into the reaction chamber through flow meters to obtain the desired composition. To include steam in the exposure environment, water was pumped from a water pump, converted to steam, pressurized, and inserted along with the gas mixture. The effluent from the reactor chamber was condensed to remove the water prior to exhaust. Figure 2.6 shows a magnified view of the high-pressure parts of the system described in Fig. 2.5.

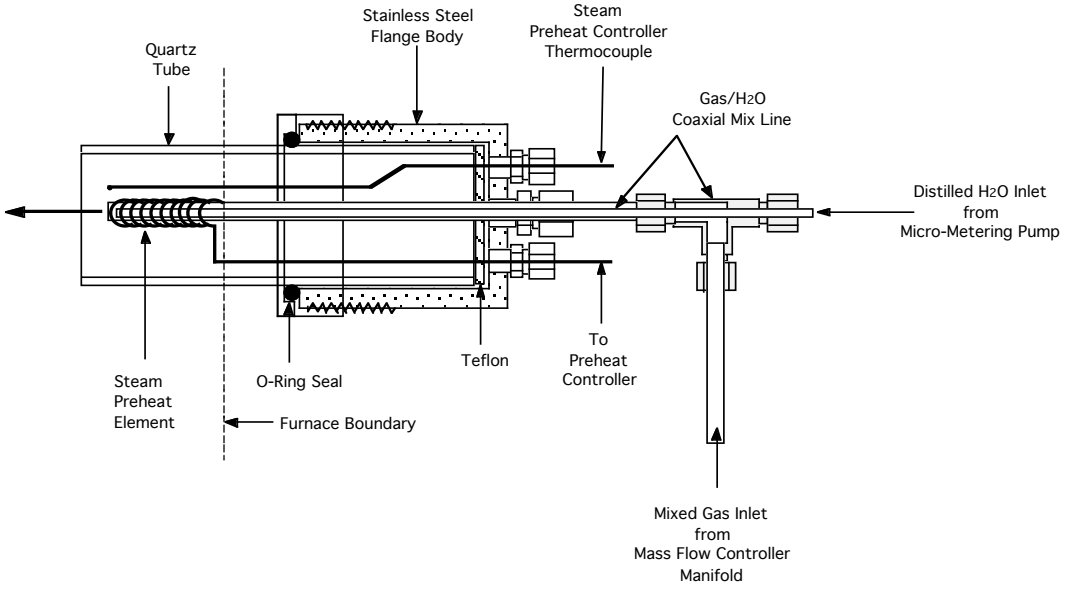

Figure 2.3. Schematic of steam and gas flow scheme used for metal dusting experiments.

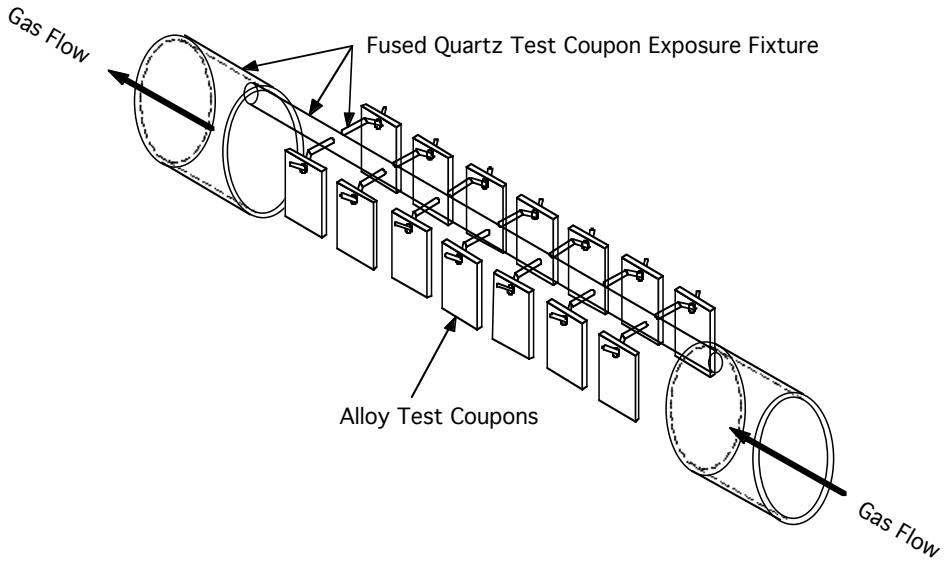

Figure 2.4. Schematic of quartz specimen holder and test coupon arrangement used for metal dusting experiments.

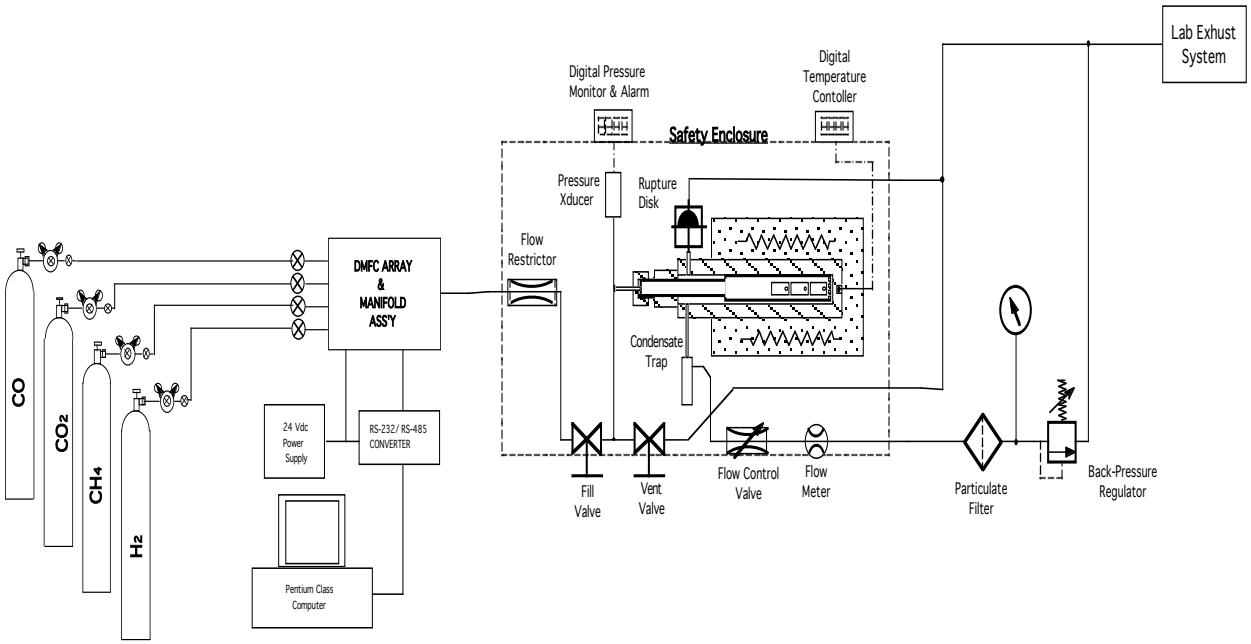

Figure 2.5. Schematic of high-pressure, high-temperature system for metal dusting experiments.

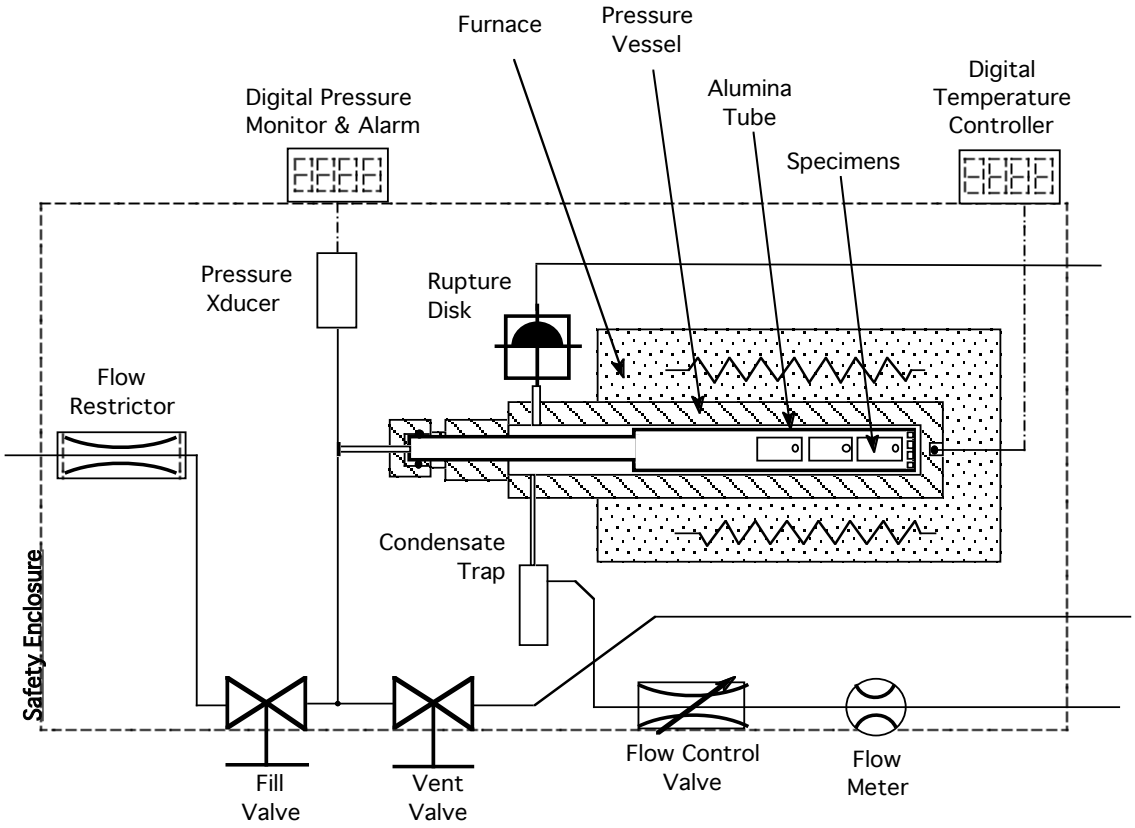

Figure 2.6. A magnified view of the high-pressure region of the system shown in Fig. 2.5.

2.2 Materials

The test program included a number of Fe- and Ni-base alloys, predominantly those commercially available, selected on the basis of Steering Committee discussions. Heat analysis of all the alloys, supplied by the alloy supplier, was maintained at Argonne National Laboratory. In addition, several surface-engineered alloy specimens (including surface coatings) were evaluated in the program. Only wrought alloys were evaluated in the test program. Table 2.1 lists the nominal chemical compositions of the alloys selected for evaluation in the program.

The Fe-base alloys included a low-Cr ferritic steel (T22), an intermediate-Cr ferritic steel (T91), and several high-Cr ferritic and austenitic steels and other alloys. The Cr content of the latter alloys ranged between 17.3 and 26.7 wt.%. The Ni content of the high-Cr alloys ranged between 9.3 and 36.6 wt.%, except for alloys MA 956 and APMT, which contained no nickel. Several of the Fe-base alloys contained a third element such as Al or Si, which has a high affinity for O. For example, MA956 and APMT contained 4.5 and 4.9 wt.% Al, respectively. Alloys 153MA, 253MA, and 353MA contained Si in a range of 1.3-1.6 wt.%, whereas Alloy 38815 contained 5.8 wt.% Si.

Generally, the Ni-base alloys had a much more complex chemical composition since they contained Cr (in a range of 15.4-28 wt.%) and several other elements, such as Mo (alloys 617 and 625), Al (601, 617, 602CA, and 214), and Si (45TM and HR 160). Further, several alloys contained Nb, W, and Co, which can also influence the oxidation behavior of the alloys and their resistance to metal dusting attack.

Surface engineering of select alloys was conducted to examine the influence of that treatment on their resistance to metal dusting. The pretreatment involved oxidation of the alloys in an air or in a low-pO_2 environment at elevated temperatures. In addition, the pack diffusion process was used to develop metallic coatings (primarily Al or Cr enrichment in the surface regions of the alloys) on several Fe- and Ni-base alloys. In general, the deposited regions were in a range of 100-200 μm thick. Prior to evaluation under metal dusting conditions, the coatings were oxidized in air at elevated temperatures to develop adherent alumina or chromia/silica scales.

2.3 Specimen Preparation

The samples were flat coupons with approximate dimensions of 12 x 20 x 1 to 2 mm. They were sheared slightly oversize, and their edges were milled to remove cut edges and reduce the coupons to final size. A standard surface finish was used for all alloy specimens. The finish involved a final wet grinding with 400-grit SiC paper. The surface-engineered specimens were used in the as-fabricated condition. In the tests to evaluate the effect of surface preparation on metal dusting, specimen surfaces were prepared by electropolishing, mill annealing, shot peening, etc. Stenciling or electric engraving at the corner of the coupons identified all of the specimens.

Table 2.1 Nominal chemical composition (in wt.%) of alloys selected for the study program.

Material	C	Cr	Ni	Mn	Si	Mo	Al	Fe	Other
Fe-base alloys									
T22	0.20	2.3	–	0.6	0.5	1.0	-	Bal	–
T91	0.08	8.6	0.1	0.5	0.4	1.0	-	Bal	N 0.05, Nb 0.07, V 0.2
153MA	0.05	18.4	9.5	0.6	1.4	0.2	-	Bal	N 0.15, Ce 0.04
253MA	0.09	20.9	10.9	0.6	1.6	0.3	-	Bal	N 0.19, Ce 0.04
353MA	0.05	24.4	34.7	1.4	1.3	0.1	-	Bal	N 0.18, V 0.06
321L	0.02	17.4	9.3	1.8	0.5	-	-	Bal	N 0.02, Ti 0.3
310	0.03	25.5	19.5	1.7	0.7	-	-	Bal	-
800	0.08	20.1	31.7	1.0	0.2	0.3	0.4	Bal	Ti 0.31
803	0.08	25.6	36.6	0.9	0.7	0.2	0.5	34.6	Ti 0.6
38815	0.01	13.9	15.3	0.6	5.8	1.0	0.13	Bal	-
MA956	-	20.0	-	-	-	-	4.5	Bal	Ti 0.5, Y_2O_3 0.6
321	0.04	17.3	10.3	1.2	0.4	-	-	Bal	Ti 0.4, N 0.01
APMT	0.04	21.7	-	0.1	0.6	2.8	4.9	Bal	-
4C54	0.17	26.7	0.3	0.7	0.5	-	-	Bal	N 0.19
Ni-base alloys									
600	0.04	15.4	Bal	0.2	0.1	-	-	9.7	-
601	0.03	21.9	61.8	0.2	0.2	0.1	1.4	14.5	Ti 0.3, Nb 0.1
690	0.01	27.2	61.4	0.2	0.1	0.1	0.2	10.2	Ti 0.3
617	0.08	21.6	53.6	0.1	0.1	9.5	1.2	0.9	Co 12.5, Ti 0.3
625	0.05	21.5	Bal	0.3	0.3	9.0	0.2	2.5	Nb 3.7, Ti 0.2
602CA	0.19	25.1	62.6	0.1	0.1	-	2.3	9.3	Ti 0.13, Zr 0.19, Y 0.09
214	0.04	15.9	Bal	0.2	0.1	0.5	3.7	2.5	Zr 0.01, Y 0.006
230	0.11	21.7	60.4	0.5	0.4	1.4	0.3	1.2	W 14, La 0.015
45TM	0.08	27.4	46.4	0.4	2.7	-	-	26.7	RE 0.07
HR 160	0.05	28.0	Bal	0.5	2.8	0.1	0.2	4.0	Co 30.0
693	0.02	28.8	Bal	0.2	-	0.1	3.3	5.8	Nb 0.7, Ti 0.4, Zr 0.03

Prior to testing, specimens were thoroughly degreased in clean acetone, rinsed in water, and dried. The specimen dimensions were measured to ±0.02 mm, and the total exposed surface area, including edges, was calculated. The specimens were weighed to an accuracy of 0.1 mg.

2.4 Post-exposure Analysis of Specimens

Several analytical approaches and techniques were used to evaluate the tested specimens. These included metal weight gain/loss in as-exposed and cleaned conditions, pitting size and density (pits per unit area of surface), pit depth (average depth over significant number of pits), and substrate penetration as determined by metallographic examination. After the specimens were weighed in the as-exposed condition, deposits on the specimens were mechanically removed with a soft brush, and the deposit material was analyzed for metal content, if warranted.

The brushed specimens were cleaned ultrasonically to remove residual deposits and then washed in water and dried. Subsequently, the specimens were weighed, and the weight gain/loss was noted. The cleaned specimens were examined for surface pits by optical microscopy. This allowed determination of the number of pits present in different regions of the specimen and the pit density. In addition, the sizes of several pits were measured and averaged to establish an average pit size.

At the end of a given run, several of the cleaned specimens (after weighing and pit measurement) were cut and mounted on the cut faces for metallographic polishing and examination in the as-polished condition (with chemical etching, if needed) by optical and/or scanning electron microscopy. Pit depth and substrate penetration thickness were measured in several exposed specimens. The remaining good metal was calculated as the difference between the original thickness and the thickness unaffected by substrate penetration after exposure.

Raman spectra were excited with 60 mW of 476-nm radiation from a Kr-ion laser. The scattered light was analyzed with a triple Jobin-Yvon grating spectrometer. All of our spectra were acquired in 300 sec at room temperature.

2.5 Metal Dusting Experiments

Table 2.2 lists the experimental conditions used for the various metal dusting runs. The list includes the test temperature, system pressure, gas chemistry, exposure time, alloys tested, and the purpose for conducting these experiments. Ten short-term runs were conducted to evaluate the role of several variables in the carbon deposition process and in the initiation of metal dusting reactions. The first nine runs were conducted to evaluate the effect of key variables such as exposure time, temperature, water content in the exposure gas, and presence/absence of catatytic material during exposure on the metal dusting initiation. The range of parameters in the scoping tests included exposure times of 5-100 h, temperatures of 593°C and 704°C, gas mixtures with and without H_2O, and presence/absence of catalyzing agent. The specimens included pure Fe, pure Ni, Type 304 stainless steel, Alloys 800 and 601, and Fe aluminide intermetallic. Runs 2 and 3 were conducted for 100 h at 593°C in Gas 4 and 5, respectively. Gases 4 and 5 had similar composition, except that Gas 5 had 2 vol.% H_2O in addition to other gases. Since Gas 4 contained no H_2O, the carbon activities of this gas mixture at 593°C (1100°F) are infinity and 4.98, based on Reactions 1 and 2, respectively. The carbon activity values for Gas 5 at 593°C are 32.3 and 5.04, based on Reactions 1 and 2, respectively.

Runs 11 through 14 were conducted to isolate the Fe and Ni specimens during exposure and also to evaluate the influence of H_2O in the exposure environment on the carbon deposition and dusting processes. Runs 15 and 16 were of 1000-h duration and were conducted with Fe- and Ni-base alloys in Gas 2, which simulated the reformer effluent. This gas contained 23 vol.% H_2O, which was achieved by pumping water into the reaction chamber through a specially designed heater. Runs 17 and 18 were conducted to evaluate the carbon deposition/dusting behavior at 482°C. Detailed analysis of the specimens from Runs 15 and 16 showed little, if any, deposit of carbon on the specimen surfaces. Carbon was noted primarily on the T22 specimen,

and virtually no carbon was detected in Run 16 conducted with Ni-base alloys. The major difference between these runs and the others (Runs 1 through 9) was the amount of H_2O in the exposure environment. Note that the carbon activity established by Gas 2 at 593°C (1100°F) is ≥2 (see Table 2), yet no deposit of carbon was noted after 1000 h exposure. Run 19 was conducted to examine the competing effects of oxidation and carbon deposition/metal dusting on alloy behavior. In this run, Fe-base alloys were exposed in Gas 2, but in contrast to Run 15, with only 2 vol.% H_2O. The calculated values for carbon activity in Runs 15 and 19 were 2 and 30, respectively, at 593°C. In Run 19, a copious amount of carbon was observed on specimen surfaces.

The specimens from Runs 1-19 (see Table 2.2 for details) were extensively analyzed, and the results were discussed in the last annual report and in several publications (Natesan et al. 2000, 2001; Zeng et al. 2001, 2002). Several conclusions were drawn from the study:

- The results were used to propose a mechanism based on catalytic crystallization of carbon for the metal dusting degradation of iron.

- The 1000-h data from these runs were also used to examine the metal dusting degradation of Fe-base alloys.

- The study indicated two major issues of importance in metal dusting. First is formation of carbon and subsequent deposition of carbon on metallic materials. Second is the initiation of metal dusting degradation in the alloy. The first is influenced by a_C in the gas mixture and availability of the catalytic surface for carbon-producing reactions to proceed. There may be a threshold in a_C (>>1) for carbon deposition. Metal dusting of the alloy in the reformer environments is determined by a competition between the oxide scale development and access of the virgin metal surface to the carbon deposit. The presence of an oxide scale may not prevent metal dusting but can delay its initiation, thereby slowing the overall attack.

- The local nature of dusting (initiated by pits on the alloy surface) on Fe-base alloys shows that defects in the oxide scales play a large role in initiation. Oxide scaling may not occur if a_C >>1 and/or if the H_2O content in the environment is very low. Laboratory experiments indicated a pronounced effect of gas chemistry (in particular, H_2O content) in the scaling, carbon deposition, and dusting initiation in the alloy. The results showed that the environment in reformers is high enough in pO_2 that a Cr-rich alloy can develop a chromia scale (given enough exposure time) before carbon deposition.

- Preliminary results showed that oxide coatings have the advantage in that they can minimize carbon-producing reactions (by reducing the availability of catalytic surface) and can also act as a barrier to minimize carbon ingress and pitting of the substrate alloy. Short-term experiments showed virtually no carbon in pre-oxidized layers of Al-, Cr-, and Si-enriched layers that were subjected to metal dusting environments.

Since the last report, we have developed a substantial body of information on both Fe- and Ni-base alloys in gas mixtures that encompass a wide range of compositions and carbon activity. In addition, we have examined the role of system pressure on the metal dusting degradation of both Fe- and Ni-base alloys. We have also gathered metal dusting performance data on alloys that were pretreated to develop oxide layers in air and/or low-pO2 environments. Data were also obtained on long-term performance of the alloys in environments that simulate the reformer effluent at atmospheric and high pressures. Information developed from these tests will be presented in subsequent sections of this report.

Table 2.2 Experimental conditions for laboratory runs.

Run Number	Experimental conditions	Gas mixture #	Objective
1	593°C, 1 atm, 48 h	6	Program start
2	593°C, 1 atm, 100 h	4	No water
3	593°C, 1 atm, 100 h	5	2 vol.% H_2O
4	704°C, 1 atm, 100 h	4	Effect of temperature, H_2O
5	704°C, 1 atm, 100 h	5	"
6	593°C, 1 atm, 5 h	5	Effect of time, H_2O
7	593°C, 1 atm, 5 h	4	"
8	593°C, 1 atm, 72 h	4	Ceramics only (no catalysis)
9	593°C, 1 atm, 72 h	5	"
10	593°C, 1 atm, 90 h	4	New system validation
11	593°C, 1 atm, 115 h	4	Fe specimen only
12	593°C, 1 atm, 115 h	Gas 4+H_2O	Fe specimen only
13	593°C, 1 atm, 100 h	Gas 4+H_2O	Ni specimen only
14	593°C, 1 atm, 100 h	4	Ni specimen only
15	593°C, 1 atm, 1000 h	2	Fe-base alloys
16	593°C, 1 atm, 1000 h	2	Ni-base alloys
17	482°C, 1 atm, 100 h	2	Fe specimen only
18	482°C, 1 atm, 100 h	2	Ni specimen only
19	593°C, 1 atm, 1000 h	Gas 2, low H_2O	Fe-base alloys
20	482°C, 1 atm, 1000 h	2	Fe-base alloys
21	482°C, 1 atm, 1000 h	2	Ni-base alloys
22	704°C, 1 atm, 98 h	High CO Gas	Fe, T91, 304
23	704°C, 1 atm, 98 h	"	Ni, Ni-base alloys
24	704°C, 1 atm, 102 h	No water	Ni, Ni-base alloys
25	593°C, 1 atm, 1000 h	2	Fe-base alloys, preoxidized at 750°C in air
26	593°C, 1 atm, 1000 h	2	Ni-base alloys, preoxidized at 750°C in air
27	593°C, 1 atm, 142 h	2	Pack diffusion coatings/Fe-base alloys
28	593°C, 1 atm, 300 h	2b	Fe-base, preoxidized in 75-CO-5CO_2 at 900°C

			for 200 h
29	593°C, 1 atm, 300 h	2b	Ni-base, preoxidized in 75-CO-5CO_2 at 900°C for 200 h
30	593°C, 1 atm, 1040 h	2	Aluminized coating
31	593°C, 1 atm, 300 h	2b	Fe-base, preoxidized in 98H_2-2H_2O at 900°C for 200 h
32	593°C, 1 atm, 300 h	2b	Ni-base, preoxidized in 98H_2-2H_2O at 900°C for 200 h
38HP	593°C, 41 atm, 90 h	8	Fe base
39HP	593°C, 41 atm, 100 h	8	Fe base
40	593°C, 1 atm, 119 h	9	Fe base
41HP	593°C, 27 atm, 100 h	8	Fe base
41R	593°C, 27 atm, 140 h	8	Fe base
42HP	593°C, 14 atm, 100 h	8	Fe base
43HP	593°C, 41 atm, 100 h	13	Fe base
44	593°C, 1 atm, 122 h	4	Fe- and Ni-base
45	593°C, 1 atm, 300 h	4	Fe- and Ni-base
46	593°C, 1 atm, 300 h	4	Fe- and Ni-base
47	593°C, 1 atm, 300 h	4	Fe- and Ni-base
48	593°C, 1 atm, 122 h	13	Fe- and Ni-base
49HP	593°C, 14 atm, 1131 h	10	Fe base
50HP	593°C, 14atm, 100 h	10	Ni base
51HP	593°C, 41 atm, 113 h	10	Ni base
52HP	593°C, 41 atm, 680 h	10	Fe base
53	593°C, 1 atm, 2284 h	11	Fe base
54	593°C, 1 atm, 1950 h	11	Ni base
55	593°C, 1 atm, 4038 h	17	Ni base
56	593°C, 1 atm, 5303 h	14	Ni base
57	593°C, 1 atm, 3447 h	15	Ni base
58	593°C, 1atm	16	Ni base
59HP	593°C, 14 atm, 5300 h	10	Ni base
60	593°C, 1 atm, 246 h	10	Ni base

3. METAL DUSTING MECHANISM IN NICKEL-BASE ALLOY

3.1 Introduction

Metal dusting corrosion of Ni and Ni-base alloys occurs in several steps (Grabke et al. 1998, Grabke 2000). In the first step carbon deposits on the surface of nickel by any of the two possible reactions,

$H_2 + CO = C + H_2O$ Reaction 1

$2CO = C + CO_2$ Reaction 2

As discussed earlier, under nonequilibrium conditions, carbon activity calculated from any one of the above reactions can dictate the carbon deposition. Generally, Reaction 1 dominates in the process, especially at temperatures of 400-700°C. High carbon activity (>1) is the driving force for the first step. In second step, carbon atoms dissolve and diffuse into the alloy. The second step is driven by the concentration gradient of carbon. Graphite particles have been observed to precipitate and grow in nickel metal (Wei et al. 2000). This process causes the nickel metal to separate into nano-size particles that move away from the bulk alloy in the third step. The objective of this study was to find the driving force that leads carbon to precipitate and to grow in nickel metal.

Investigations into the mechanism of metal dusting have focused predominantly on defects in the metals. Defects in carbon deposits have hardly been studied, even though carbon is an integral part of the metal dusting process. The structure of graphite is layered, with the space group $P6_3/mmc$ (see Fig. 3.1). Carbon atoms within the layers bond strongly through sp^2 hybridization and arrange in a two-dimensional honeycomb network. The layers are stacked in a hexagonal crystalline structure and are bound together by van der Waals forces. Because the van der Waals force is weak, the C-C distance between layers is a large value of 3.354 Å (Franklin 1951). For this reason, graphite crystals readily become disordered along the c-axis (Krebs 1968).

Several researchers have studied the structural disorder of graphite by Raman scattering (Dillon and Woollam 1984, Tuinstra and Koenig 1970, Nakamizo et al. 1977, 1978). Lattice defects in graphite break down the hexagonal symmetry of the graphite lattice and modify the optical selection rules for the lattice vibrational modes that are observable in Raman scattering. A single Raman line, the E_{2g} vibration mode, is theoretically expected for the hexagonal lattice of graphite and has been observed at 1575 cm^{-1} in natural graphite. In glassy carbon, the mutual orientation between the layers is random (due to the weak link between the layers). A band at 1355 cm^{-1}, observed for glassy carbon, has been assigned to a defect-activated vibrational mode that originates at the distorted hexagonal lattice of graphite near the crystal boundary. The two bands at 1355 and 1575 cm^{-1} are designated as the D (distorted) band and the G (graphite) band, respectively. It has been reported that the relative intensity ratio I_D/I_G and the relative

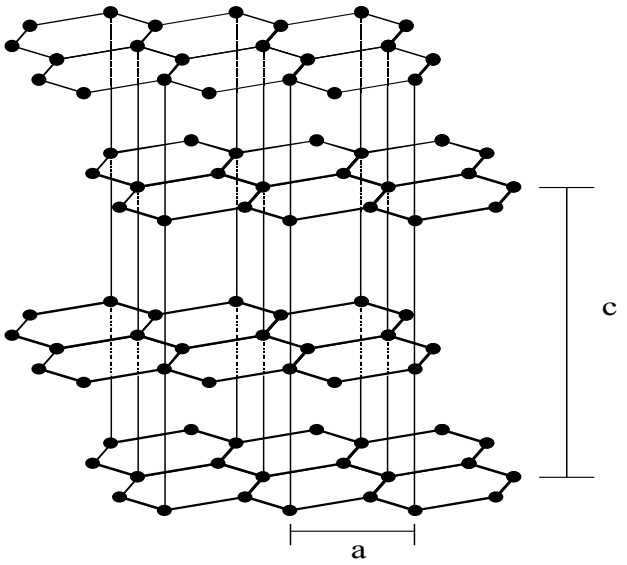

Figure 3.1. Structure of graphite. Carbon atoms within layers are arranged in two-dimensional honeycomb network; layers are stacked in hexagonal crystal structure.

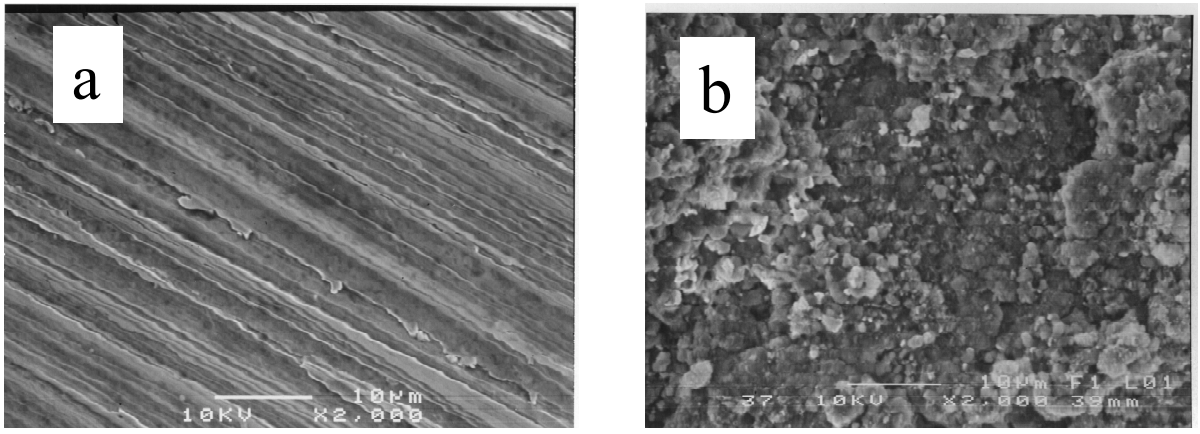

Figure 3.2. Surface SEM image of nickel (a) before and (b) after exposure in a carburizing atmosphere at 593°C for 100 h.

bandwidths increase in progression from single-crystal graphite through polycrystalline graphite up to glassy carbon; hence, their values can be used as a measure of imperfection of the planes of the graphite layer. These parameters are more defect-sensitive than are the X-ray diffraction (XRD) parameters that define crystalline size. Therefore, Raman spectroscopy represents a useful tool for investigating the defects in carbon structures and their relationship to metal dusting. In this report, we present results of Raman spectroscopy measurements that are pertinent to the metal dusting of nickel and nickel-base alloys.

3.2 Scanning Electron Microscopy (SEM) Observations

The surface of the nickel specimen was smooth before exposure in the carburizing atmosphere (Fig. 3.2a); the lines in the photomicrograph of the surface are polishing marks made by the SiC paper. However, the nickel surface became rough (Fig. 3.2b) after exposure in the metal dusting environment. Even ultrasonic cleaning and acetone washing could not remove a tightly adhering carbon layer on the surface of the nickel. The thickness of the carbon layer was ≈40 μm, but was not uniform. Metallographic cross sections showed separation of nickel grains

and their subsequent incorporation in the carbon layer (Fig. 3.3). The surface of Alloy 601 was smooth after exposure in the carburizing atmosphere for 100 h at 593°C, and no metal dusting corrosion was observed in 100 h (see Fig. 3.4).

3.3 Oxide Scale on the Surface of Alloy 601

The effect of Cr on metal dusting was investigated, the results of which showed that a Cr_2O_3 layer protected the alloys from metal dusting (Grabke 1998, Strauss and Grabke 1998). Cr_2O_3 was observed by Raman spectroscopy on the surface of Alloy 601 tested in our study (see Fig. 3.5). The 303, 355, and 559 cm^{-1} peaks correspond to Cr_2O_3 (Farrow et al. 1980, Thierry et al. 1988, Maroni et al. 1990, and Thibeau et al. 1978). A broad band at ≈680 cm^{-1} was observed as shown in the Raman spectrum of Alloy 601. This band also corresponds to an oxide phase and will be discussed in detail later in this report.

3.4 Crystallization of Carbon in Metal Dusting Process

The major phases observed in the metal dusting product were graphite and nickel metal (see Fig. 3.6). As mentioned above, a tightly adhering carbon layer was present on the surface of the nickel. The XRD [002] peak width of this carbon layer was broader than that of well-crystallized graphite (see Fig. 3.7), a finding we interpret as due to inferior crystallinity of the carbon when compared to that of graphite. The width of the XRD [002] of coke was even broader than that of the carbon in the adhering carbon layer; however, it was much narrower than that of carbon black, which was made by thermal decomposition of gasoline vapor at 704°C (see Fig. 3.8). Table 3.1 shows that the crystallite size of coke is much larger than that of carbon black. The crystallite size of coke is also considerably larger than those reported for other carbonaceous materials made at a similar temperature (Blayden et al. 1940, Schaeffer et al. 1953).

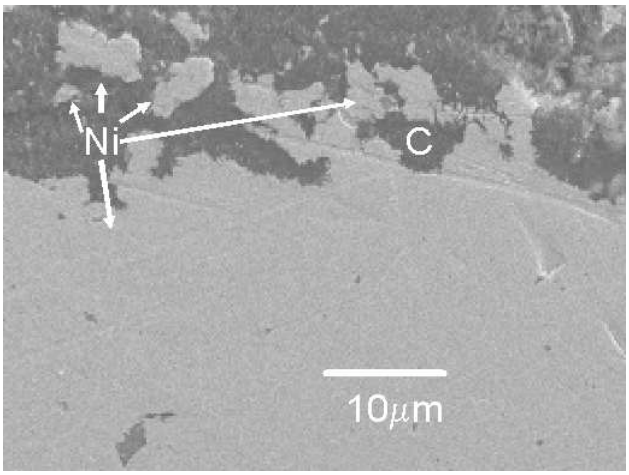

Figure 3.3. SEM image of metallographic cross section of nickel surface after ultrasonic cleaning. Tightly bound carbon layer is visible.

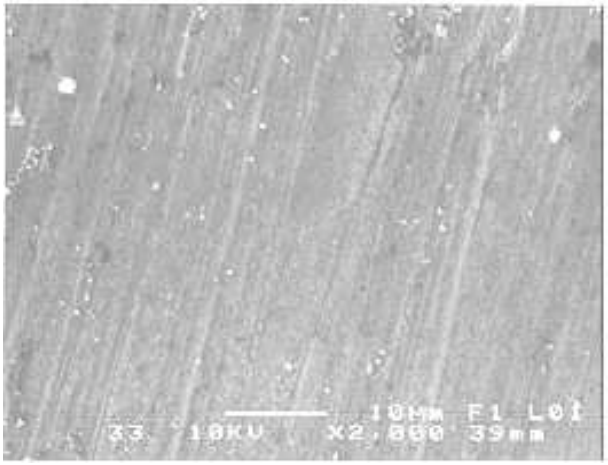

Figure 3.4. SEM image of surface of Alloy 601 after exposure in a carburizing gas atmosphere at 593°C for 100 h.

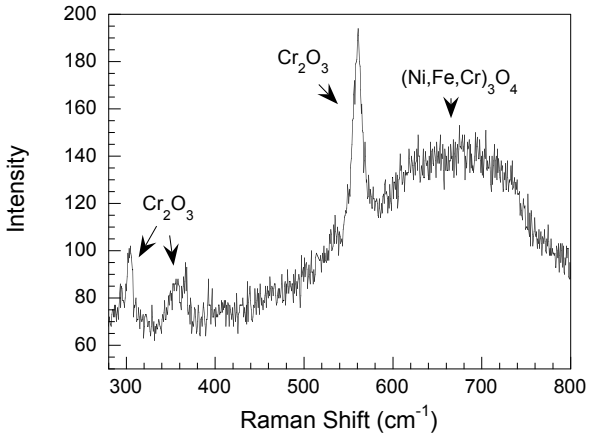

Figure 3.5. Raman spectrum of surface of Alloy 601 after exposure in a carburizing gas atmosphere at 593°C for 100 h.

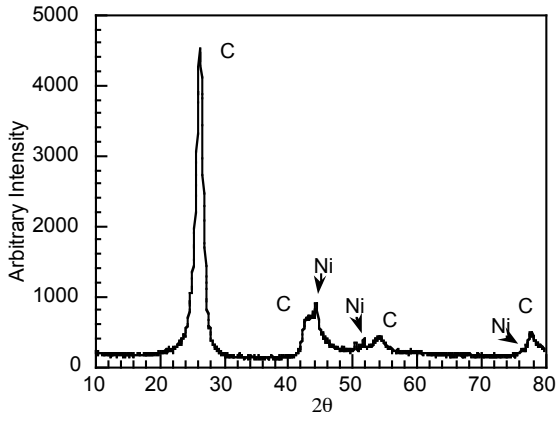

Figure 3.6. X-ray diffraction pattern of coke.

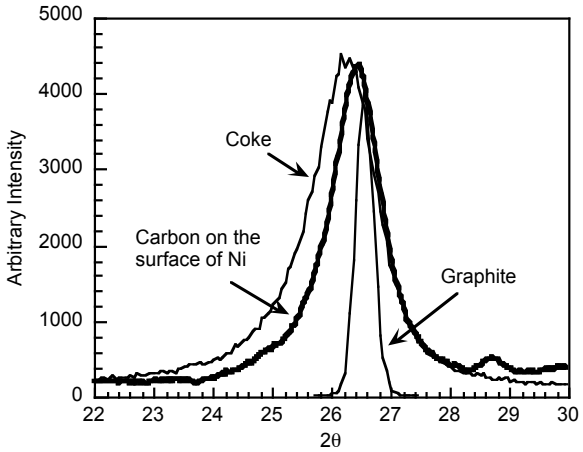

Figure 3.7. Peak widths of XRD [002] diffraction of graphite, coke, and carbon in the adhering carbon layer on nickel.

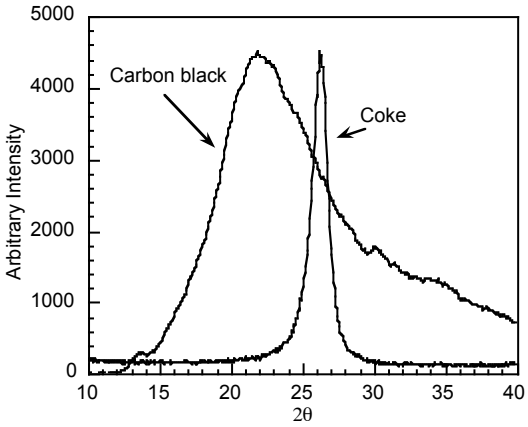

Figure 3.8. XRD [002] diffraction of carbon black and coke.

Table 3.1. Crystallite dimension and interlayer plane distance of graphite, coke (made at 593 and 704°C), and carbon black. Δ is difference of interlayer plane distance of carbon from single-crystal graphite (with interlayer plane distance 3.354 Å).

Carbon material	Interlayer plane distance (Å)	Δ (Å)	Crystallite size (Å)	Mean number of layers per particle
Graphite	3.356	0.002	220	65.7
Coke developed at 704°C	3.368	0.014	106	31.5
Coke developed at 593°C	3.396	0.042	62.8	18.5
Carbon black	4.026	0.672	9.9	2.5

In Fig. 3.8, the peak position of carbon black moves to a smaller diffraction angle, which indicates that the interlayer distance between the carbon planes is also related to the degree of disorder (Blayden et al. 1940, Schaeffer et al. 1953, Kinney 1956). The layers are not parallel in the disoriented graphite structure. Average interlayer plane distance increases when layers are disoriented, as shown in Fig. 3.9. The interlayer plane distance is 3.354 Å for single-crystal graphite (Franklin 1951). The interlayer plane distance for coke is very close to that of the well-crystallized graphite. Franklin proposed the following relationship for the proportion of disoriented layers (p) as a function of interlayer plane distance (d):

$$d = 3.44 - 0.086(1 - p^2)$$

According to this relationship, the interlayer plane distance for coke made at 593°C (3.396 Å), seen in Table 3.1, is indicative of carbon with ≈60% three-dimensional ordering. For the carbon produced by conventional treatment of carbon-containing raw materials, a heat treatment temperature >2000°C is necessary for thermal recrystallization before this high degree of three-dimensional ordering is achieved (Franklin 1951, Blayden et al. 1940, Schaeffer et al. 1953, Kinney 1956, Austin and Hedden 1956). Therefore, nickel may work as a catalyst to help the crystallization of carbon to achieve higher ordering at lower temperatures.

Raman spectra of coke, carbon black, and graphite are presented in Fig. 3.10. The well-crystallized graphite shows a sharp band at 1580 cm^{-1} (G band) that can be assigned to E_{2g} C-C stretching mode (Tunistra and Koenig 1970, Nemanich and Solin 1979, Vidano and Fischback 1978). The first-order phonon band at 1360 cm^{-1} (D band) is not observed for well-crystallized graphite because of the k = 0 selection rule (Tunistra and Koenig 1970). However, disorder in the lattice can cause a breakdown of this selection rule, and thereby exhibit a band at 1360 cm^{-1} in the Raman spectra of carbon black. The highly disordered carbon exhibits very broad Raman bands, and the intensity of the 1360 cm^{-1} band increases when carbon becomes more disordered. The intensities of the D band are considered dependent on the in-plane displacements, which lead to a loss of hexagonal symmetry of the two-dimensional graphite lattice within the planes (Nakamizo et al. 1978). A shoulder at 1620 cm^{-1} in the cokes is also dependent on structural disorder and is, therefore, designated as the D' band; its behavior is qualitatively similar to that of the D band (Vidano and Fischback 1978, Knight and White 1989).

The widths of Raman bands for the coke from the dusting process are between those of well-crystallized graphite and carbon black, which indicates that the crystallinity of coke is better than that of carbon black, but worse than that of well-crystallized graphite. The Raman spectra in Fig. 3.11 show that the band for the carbon in the adhering carbon layer on the specimen is narrower than that for coke at some distance from the surface. The relative intensity ratio I_D/I_G of coke is also larger (1.22) than that of the carbon (1.07) in the adhering carbon layer. These results may indicate that the crystallinity of carbon in this layer is better than that of coke, and this is consistent with the XRD results.

Raman spectra (Fig. 3.12) indicate that a small amount of carbon is present on the surface of Alloy 601. The amount of carbon is too small for detection by XRD; however, Raman spectra are sensitive enough to detect the carbon deposited on the oxide layer of Alloy 601. The width of the Raman band for this carbon is close to that of carbon black, which is deposited without

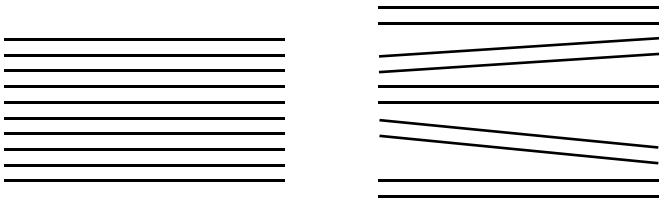

Figure 3.9. Schematic of interlayer planes in single-crystal and disoriented graphite.

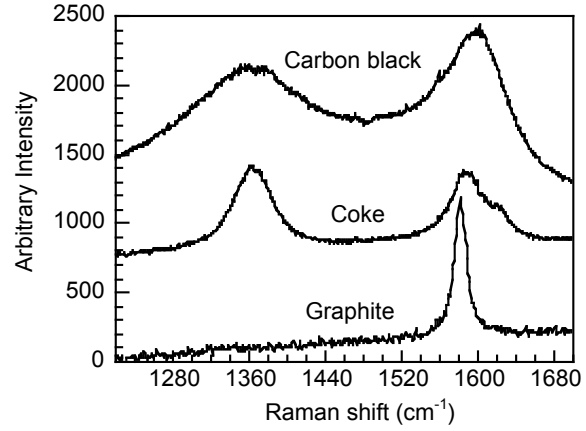

Figure 3.10. Raman spectra of coke, carbon black, and graphite.

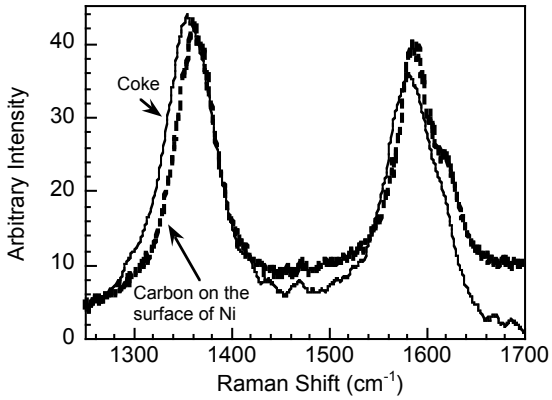

Figure 3.11. Raman spectra of bulk coke and carbon in the adhering carbon layer of the nickel specimen. The relative intensity ratio I_D/I_G of coke (1.22) is larger than that of carbon on surface of nickel (1.07), which indicates that crystallinity of carbon on nickel surface is better than that of bulk coke.

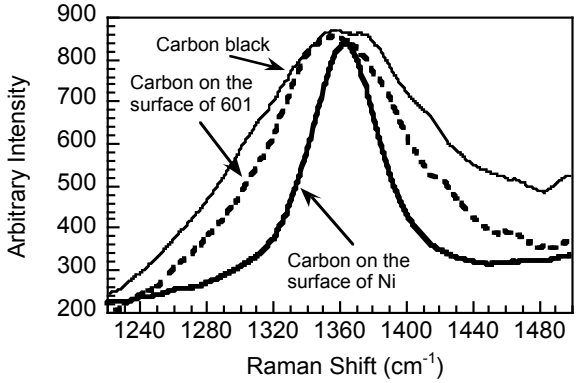

Figure 3.12. Raman spectra of carbon black and carbon on surface of Alloy 601 and pure nickel.

a catalyst. However, the width of the Raman band of the carbon in the adhering carbon layer of the nickel specimen is much narrower than that of both carbon black and the carbon on the surface of Alloy 601. This finding indicates that the crystallinity of the carbon in the adhering carbon layer of the nickel specimen is much better than that of the carbon on the surface of Alloy 601. The SEM image in Fig. 3.4 shows that metal dusting corrosion has not initiated on the surface of Alloy 601 after 100 h exposure in a carburizing atmosphere. Carbon has not penetrated through the oxide layer on the surface of Alloy 601 in 100 h, and the oxide layer has not acted as a catalyst to aid in the catalytic crystallization of carbon. Therefore, the crystallinity of carbon on the surface of Alloy 601 is similar to that of carbon black. These results indicate a possible relationship between metal dusting and the catalytic crystallization of the carbon, because the crystallinity is good if the carbon experienced metal dusting and the crystallinity is poor if the carbon has not experienced metal dusting.

Another example is that carbon at the metal-dusting pit area on Alloy 45TM also has a sharper Raman band than that of carbon in the area without pit (see Fig 3.13). This result also indicates that metal dusting is related to the improvement in crystallinity of carbon.

3.5 Proposed Mechanism

Figure 3.14 shows our interpretation of the crystallizing process for carbon during dusting of nickel (essentially same process for iron). In the initial stage, single carbon atoms are deposited on the surface of the nickel; they then either dissolve in the nickel or accumulate to form small carbon particles. There are dangling bonds on the surface and many defects, such as vacancies and distorted bonds in the small particles. The surface and internal defects cause an increase in the free energy of these particles compared to that of well-crystallized graphite. At higher temperature, where the carbon atoms have enough energy to migrate, the carbon crystallizes from small distorted particles to large well-crystallized graphite. However, because the C-C bond is very strong (the melting temperature of carbon is 4492°C), the crystallization process requires a higher temperature. The rate of carbon crystallization could be dramatically increased if nickel acts as a catalyst. When carbon dissolves in nickel, the Ni-C bond is much weaker than the C-C bond, and transport of carbon atoms is greatly facilitated. Therefore, the poorly crystallized coke can transfer through nickel and eventually achieve improved crystallinity. Reducing the number of dangling bonds on the surface and the number of internal defects in the carbon particles then decreases the free energy.

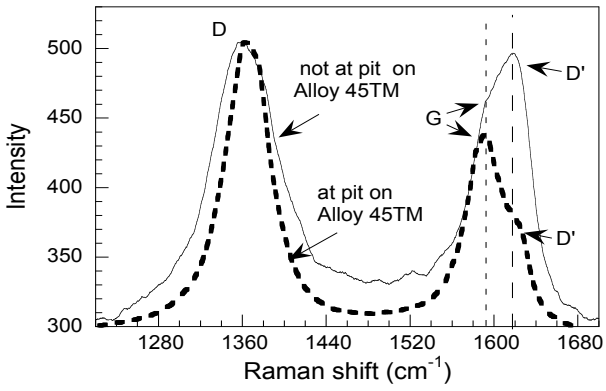

Figure 3.13. Raman spectra of carbon at pit and non-pit areas on surface of Alloy 45TM.

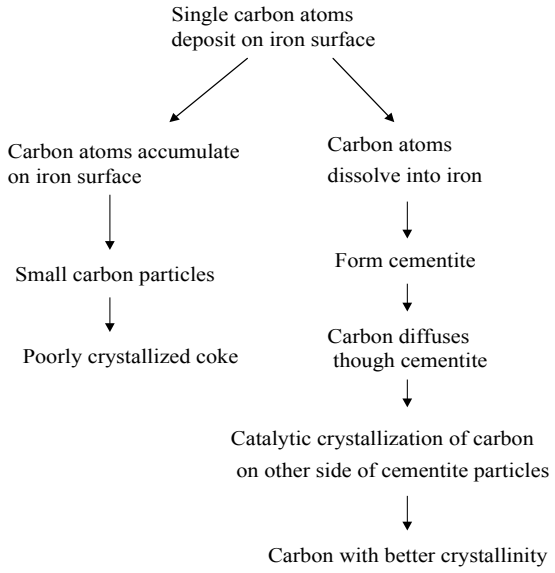

Figure 3.14. Proposed process for carbon crystallization after deposition from carburizing gas. Carbon atoms accumulate on surface and form poorly crystalline carbon particles in the left branch when Ni lattice does not help the crystallization process of carbon. However, highly crystalline carbon is formed in right branch, if carbon diffuses through nickel, and the nickel lattice helps the crystallization of carbon.

Figure 3.15 shows the catalytic crystallization process. As mentioned above, the carbon layers in the graphite structure are easily disoriented because the van der Waals forces between the layers are weak. At the upper surface of the nickel particle, there is a mismatch between the lattice planes of the nickel and graphite. This lattice mismatch retards the formation of well-crystallized graphite. If carbon grows from this nickel lattice plane, poorly crystallized carbon will form. However, carbon atoms can dissolve into and diffuse though the nickel lattice; they precipitate from a lattice plane that provides an excellent orientation for the epitaxial growth of graphite. Graphite was reported to grow with its layer plane parallel to the (111) plane and (110) of the nickel (Wei et al. 2000). The catalytic crystallization process leads to a coke (produced during metal dusting) with a crystallite size that is much larger and an interlayer plane distance that is smaller than those of carbon made by other methods at a similar temperature (Franklin 1951, Blayden et al. 1940, Schaeffer et al. 1953, Kinney 1956).

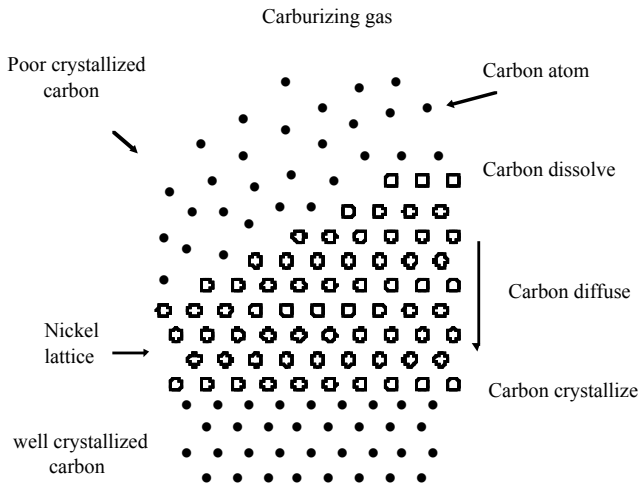

Figure 3.15. Illustration of carbon crystallization process in nickel leading to metal dusting.

In our proposed catalytic crystallization process, carbon dissolves on the surface of the nickel and crystallizes at the defects of the bulk nickel. Because the free energy of poorly crystallized carbon is probably higher than that of well-crystallized graphite, the saturating concentrations for poorly crystallized carbon and graphite will differ. Poorly crystallized carbon should exhibit a slightly higher saturating concentration than that of graphite; hence, the saturating concentration of poorly crystallized carbon will be oversaturating for graphite; therefore, poorly crystallized carbon could dissolve in nickel and form well-crystallized graphite. The free energy difference between poorly crystallized carbon and the well-crystallized graphite drives carbon to transfer through the nickel particles and precipitate inward via the defects or grain boundary of nickel. The accumulation of carbon in an alloy causes the metal to separate, as seen in Fig. 3.3. The metal particles finally become nano-size powder in this process until they are too small to help carbon grow to large crystals (see Fig. 3.16). The nano-size nickel particles in coke continue to interact with carburizing gas. These particles also work as catalyst to help the deposition of carbon. However, the average size of a nickel particle in coke is only 48 nm. These nickel particles are too small to help carbon grow to large crystals. The surface areas of nano-particles are large. Therefore, carbon has more chance to accumulate on the surface of nano-size nickel particles according to the left branch in Fig. 3.14, and formed poorly crystallized particles. Since coke contains these poorly crystalline carbon particles, its crystallinity is worse than that of the carbon in the adhering carbon layer of the nickel specimen.

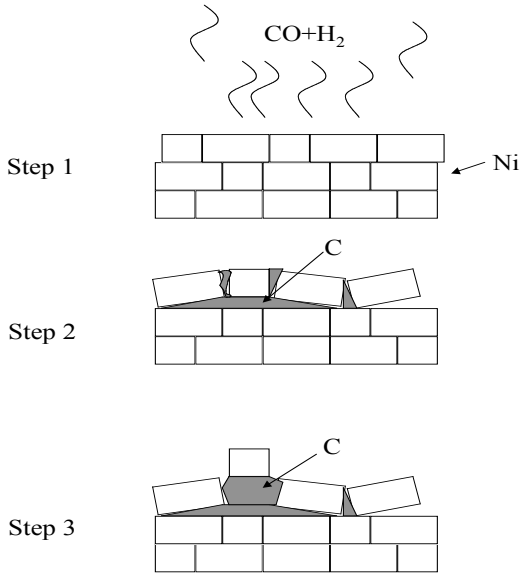

Figure 3.16. Schematic of steps involved in metal dusting of nickel.

3.6 Conclusions

Raman and XRD results shed some light on the metal dusting mechanism. Carbon on an oxide layer, which did not participate in the metal dusting process, exhibits poor crystallinity, whereas carbon on the metal surface and in pits, which experienced the metal dusting process, shows good crystallinity. These results indicate that metal dusting process involves catalytic crystallization of carbon. Nickel acts as a catalyst in this process, and the catalytic crystallization causes inward transport of carbon into the nickel. The accumulation of carbon in nickel leads to

separation of nickel into a fine powder and eventual degradation of the alloy by metal dusting. The difference in the free energy between poorly crystallized coke and well-crystallized graphite is the driving force for crystallization of coke and for the metal dusting corrosion. Although the driving force is very small, it can lead to severe corrosion in the long term.

4. RELATIONSHIP BETWEEN GROWTH OF CARBON FIBERS AND METAL DUSTING CORROSION

4.1 Carbon Fibers/Tubes in Metal Dusting Process

Metal dusting corrosion always follows coke formation. There are two types of coke. One type forms homogeneously from gas phase reaction when carbon activity is >1. The other type forms on the surface of metals or alloys. The formation of the second type of coke involves catalytic action of metal particles. The coke in the latter case usually consists of carbon nanotubes and/or nanofibers instead of powders. Figures 4.1 and 4.2 show carbon filaments in coke. There usually is a nanosize metal particle at the tip of these carbon nanotubes or nanofibers.

Recently, the growth of carbon nanotubes has attracted much attention since they have many potential applications in electronic devices and as a hydrogen storage medium (Iijima 1991, Deheer et al. 2001, Liu et al. 1999). Meanwhile metal dusting is anther old problem in the petrochemical, syngas, and other industries (Lefrancois and Hoyt 1963, Hochman 1977). Both research fields involve growth of carbon nanotubes. However, the two phenomena are usually

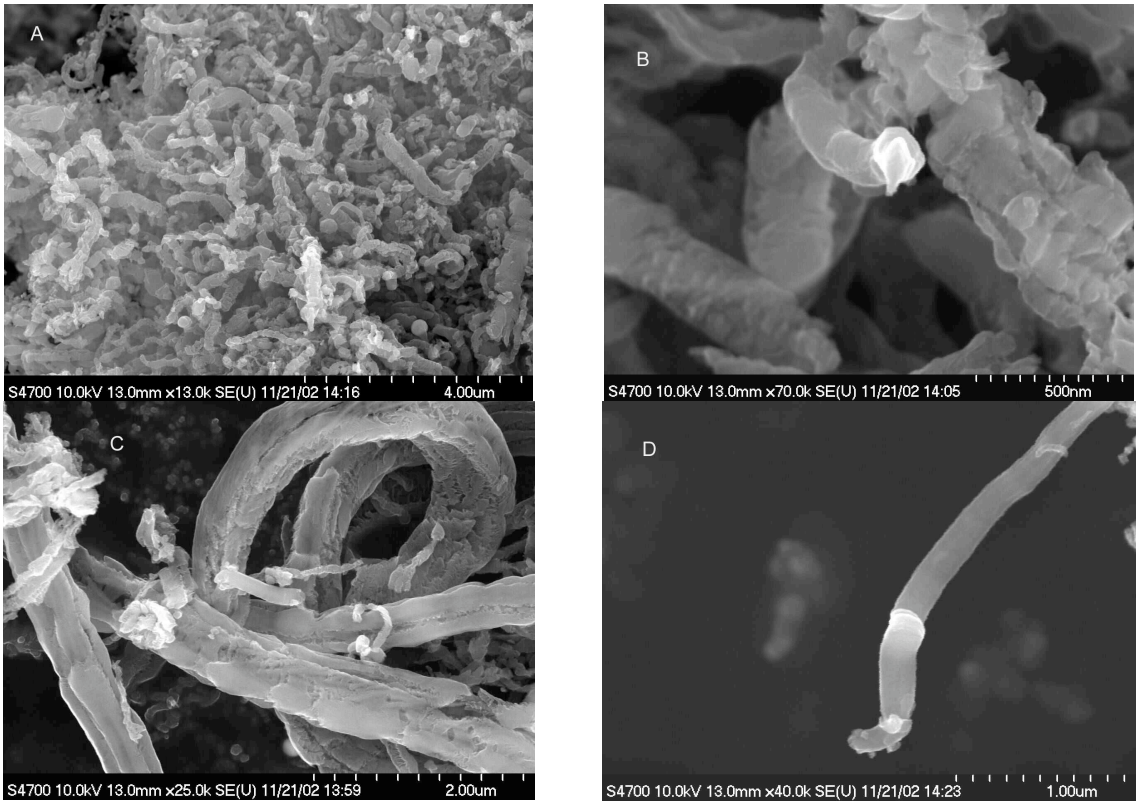

Figure 4.1. SEM photographs of several coke forms developed after exposure in Gas 5 at 593°C for 100 h.

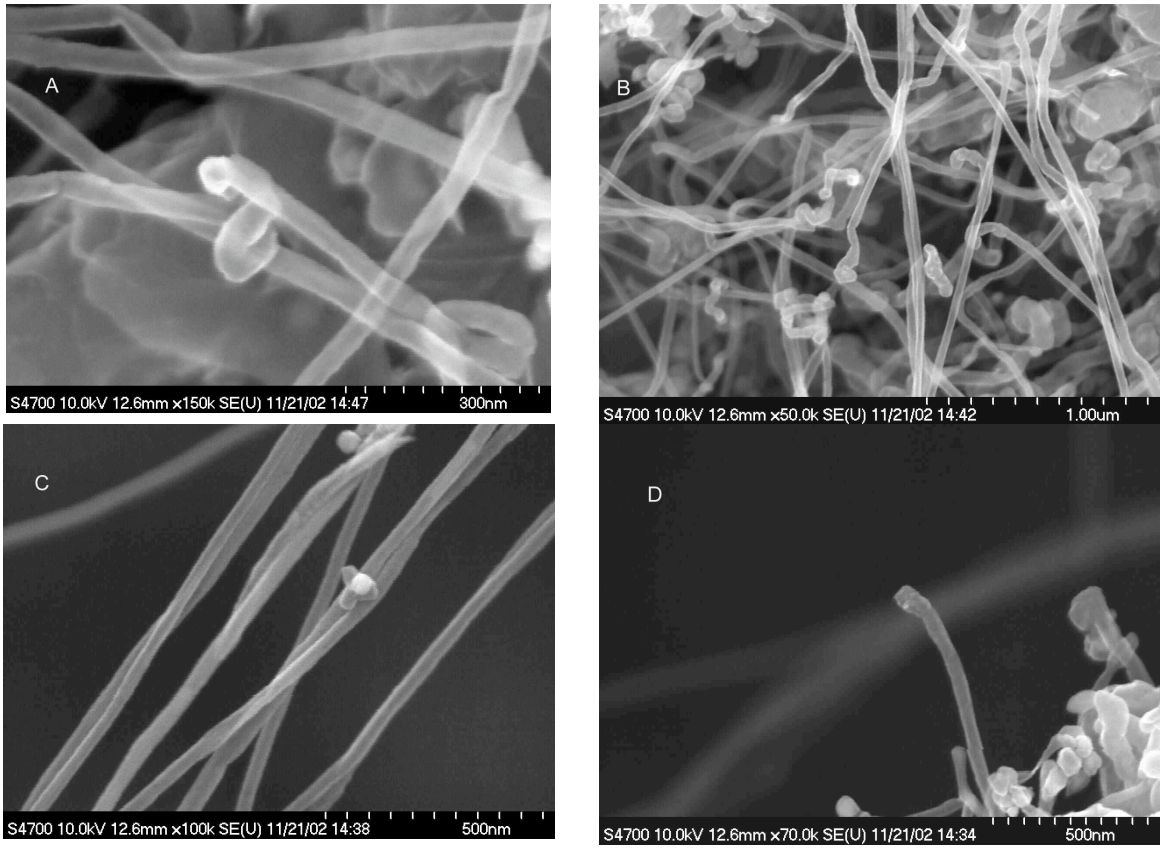

Figure 4.2. SEM photographs of additional forms of coke developed after exposure in Gas 5 at 593°C for 100 h.

studied separately. Neither the mechanism of catalytic growth of carbon filaments, nor the mechanism for metal dusting has been clear so far. Generally, metal dusting pits are filled with carbon nano-filaments, as evidenced by the photomicrograph shown in Fig. 4.3. There may be a relationship between the growth of carbon nano-filaments and metal dusting corrosion. In this study, we try to achieve a complete picture by examining the two phenomena.

To grow carbon filaments, nanoparticles of Ni and Fe are used as catalysts. In 1972, Baker proposed a mechanism for the growth of carbon filaments assisted by metal particles (Baker et al. 1972). This mechanism involves diffusion of carbon through the metal particle from the hotter leading face, on which exothermic decomposition of the hydrocarbon occurs, to the cooler trailing faces, at which carbon is deposited from solution, as shown in the schematic in Fig. 4.4. The temperature gradient is the driving force for the diffusion of carbon through the metal particle and the growth of carbon filaments. But this mechanism fails to explain the carbon fiber growth by pyrolysis of methane (Rostrup-Nielson 1975), an endothermic decomposition. Other mechanisms also cannot totally explain the catalytic growth of carbon filaments (Yang and Chen 1989).

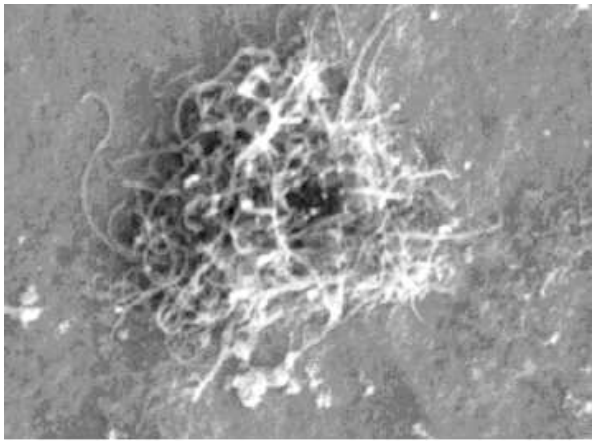

Figure 4.3. Carbon nano-filaments formed at a metal dusting pit on surface of Alloy T91.

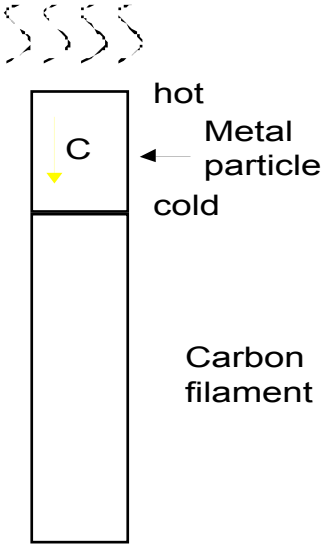

Figure 4.4. Schematic for the growth of carbon filaments.

4.2 Metal Dusting Corrosion

Hochman proposed a mechanism for the metal dusting of iron (Hochman 1977). The steps involve the following: (a) carbon deposits on the metal surface and dissolves in the metal; (b) Fe_3C forms as carbon diffuses into the iron, and the metal becomes oversaturated; and (c) metastable Fe_3C decomposes to Fe and graphite by the reaction: $Fe_3C = 3Fe + C$. According to this mechanism, the final product is graphite and iron. However, Fe_3C instead of iron is usually observed in the final product of metal dusting. It is not clear what drives the formation and decomposition of Fe_3C under the same conditions of temperature, pressure, and composition. To explain the experimental observations, we proposed a new mechanism for the metal dusting of Fe-base alloys as follows (Natesan 2002, Zeng and Natesan 2003):

1. Carbon deposits on iron surface and supersaturates the iron.

2. Cementite forms at the surface of the iron, and the volume expansion creates defects.

3. Carbon diffuses through the cementite and precipitates at defects.

4. Accumulation of carbon at defects causes the cementite to separate into small particles and move away from the metal.

5. Gas penetrates into cracks in the metal and continues further deposition of carbon and metal dusting.

More evidence to support this mechanism is that carbon at the metal dusting pit area has a sharper Raman band than that of carbon in the non-pit area (see Fig 4.5). This finding means that the crystallinity of carbon at the metal dusting pit is better than that in the non-pit area. The shoulder at 1613 cm^{-1} in the coke is also dependent on structural disorder and is, therefore, designated as the D' band. The G band (at 1590 cm^{-1}) was not observed in carbon for the non-pit area since the D' band is as strong as the G band and the two bands overlap. However, the G band is obviously stronger than the D' band for the carbon in the pit region. This finding also means that the crystallinity of carbon at the metal dusting pit is better than that in the non-pit area. Therefore, the metal dusting process is related to the improvement in crystallinity of carbon.

4.3 Carbon Catalytic Crystallization by Metal and Carbide

Figure 4.6 shows a schematic of the catalytic crystallization process. Carbon atoms are deposited on the surface of Fe_3C. The carbon layers in the graphite structure are easily disoriented because the van der Waals forces between the layers are weak. Carbon cannot grow with good crystallinity if the lattice planes of Fe_3C do not match the graphite lattice planes to help the crystallization of carbon (up position in Fig. 4.6). However, when carbon atoms diffuse through the Fe_3C and precipitate from a favorable face, the lattice of Fe_3C provides an excellent orientation for the epitaxial growth of graphite. Graphite was reported to grow perpendicular to the lattice plane of Fe_3C with its layer plane (Chun et al. 1999). Fe_3C has an orthorhombic lattice with cell parameters a = 5.091, b = 6.743, c = 4.526 Å; its b axis is almost the same as the c axis of graphite (6.724 Å). This is helpful for the crystallization of graphite.

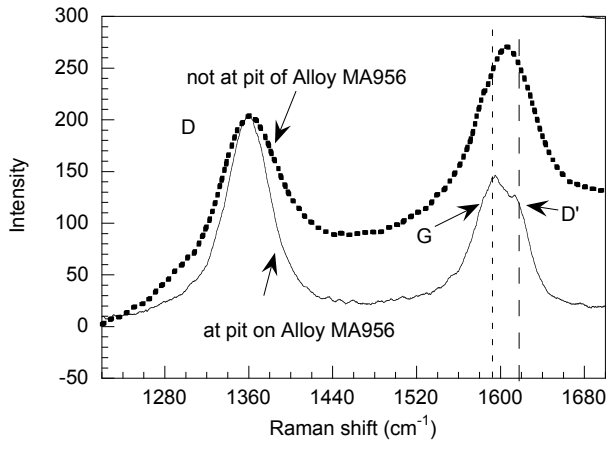

Figure 4.5. Raman spectra of carbon at pit and non-pit areas on surface of Alloy MA956.

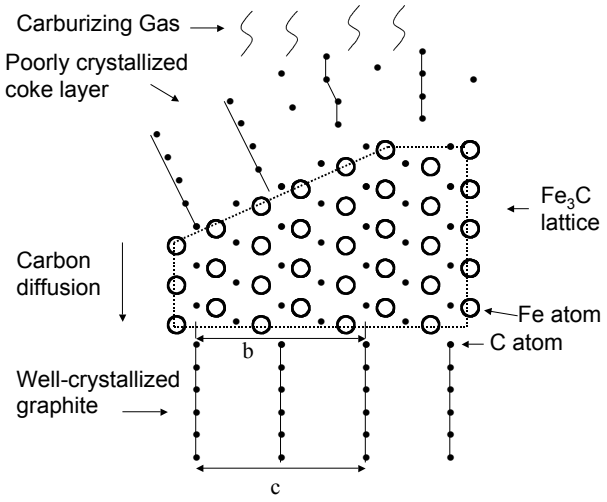

Figure 4.6. Schematic of catalytic crystallization process in Fe and Fe-base alloys. Poorly crystallized carbon dissolves in and diffuses through Fe_3C, whose lattice provides excellent orientation for crystallization of graphite; b dimension of Fe_3C (6.743 Å) is very close to c dimension of graphite (6.724 Å).

The crystallization process for carbon through nickel particles may be slightly different from that through Fe_3C, since graphite was reported to grow parallel instead of perpendicular to the (111) face of Ni with its layer plane (Wei et al. 2000). However, the carbon behavior in the processes through both Fe_3C and Ni is similar. Carbon was catalytically deposited on the face of metal or carbide, and then found another favorite face to precipitate out. Such a catalytic crystallization process causes the coke produced from metal dusting to have a much larger crystallite size and a smaller interlayer plane distance than those of carbons made by other methods at a similar temperature. Single-crystal graphite has a total interlayer binding energy ≈3 kcal/mol (Peacock 1960). The binding energy decreases with increasing interlay plane distance (Lewis et al. 1965). It is estimated that the enthalpy increment is 900 ± 200 J mol^{-1} for an increase in interlayer plain distance of 2.1% among the pyrolytic graphite (Abrahamson 1973). The initial state of carbon that is deposited on the surface of metal is very disordered. The free energy difference between this carbon to the well-crystalline graphite should be much larger than the difference between polycrystalline graphite to single-crystal graphite. The catalytic crystallization leads to improved crystallization of carbon and to decreased in free energy from poor crystalline carbon to good crystalline carbon. This energy difference drives carbon to transfer from one face to another face of metal or carbide.

4.4 Proposed Mechanism

When the above carbon crystallization process occurs in metals and alloys, carbon transfers from the Fe_3C surface and grows inward via the defects or grain boundary of Fe_3C. The accumulation of carbon in the alloy causes the metal particles to disintegrate, as seen in Fig. 4.7. When carbon continues to precipitate under the Fe_3C particle, a carbon filament is formed as shown in Fig. 4.8. Both carbon filament growth and metal dusting involve catalytic deposition of carbon and catalytic growth of graphite on the metal surface. The deposition and precipitation process may favor different faces. Therefore, carbon deposits on one face of metal or carbide and precipitates on another face. The carbon transport through carbide or metal particles causes the movement of metal particles and the growth of carbon filaments. Both processes have the same driving force, which is the free energy difference between poor and good crystalline carbon. For large-size carbon fiber, the decrease in interlayer plane distance decreases the free energy of the carbon fiber. The metal dusting process ultimately results in separation of very

small particles when carbon is continuously inserted into defects in metals. When the metal particles at the tip of carbon filament are very small, the carbon sheet follows the contour of the metal particles to fold into tubes, so that the system energy decreases after the dangling bonds on the two edges of the sheet merge together. This driving force always exists, no matter whether the carbon deposition is an exothermic or endothermic reaction. If we assume that the driving force for carbon filament growth is the temperature difference, it is difficult to understand why carbon filaments grow under both exothermic and endothermic environments. However, the observed behavior can be explained if we assume the driving force is the free energy difference between the poor and good crystalline carbon. The proposed mechanism explains the metal dusting process without involving the decomposition of Fe_3C.

Nickel carbide does not form in the metal dusting process since it is unstable. Therefore, the mechanism for nickel has been previously considered to be different from that for iron (Grabke et al. 1996). However, if the carbon catalytic crystallization process through iron carbide and nickel is similar, their metal dusting mechanism should be similar, although the process details may be slightly different. Metal dusting of both iron and nickel is caused by the catalytic crystallization of carbon and has a similar driving force. Carbon is easy to deposit on (100) and (110) faces of nickel and to precipitate from (111) and (311) faces (Yang and Chen 1989). The deposited carbon into and out of different faces causes the nickel particles to move and separate into dust. When carbon continues to transfer from one face of Ni to another face, the accumulation of carbon leads to the formation of carbon fibers or tubes. This process is similar to the formation of carbon fibers or tubes through Fe_3C. Figure 4.9 shows the proposed process for metal dusting in nickel. A comparison of the proposed mechanism with Hochman's mechanism for metal dusting of iron is shown in Fig. 4.10.

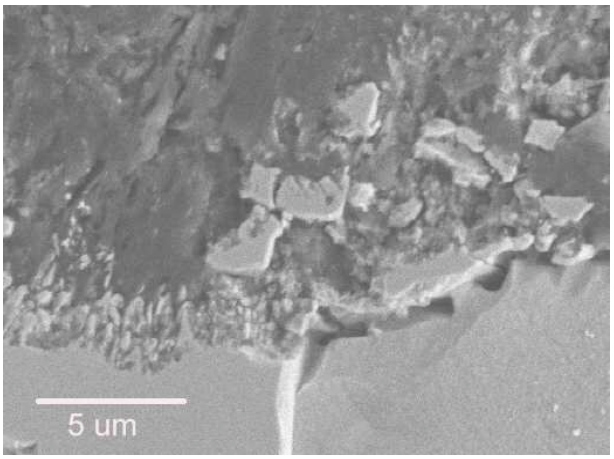

Figure 4.7. SEM micrograph of metallographic cross section of iron. Iron particles are separated into small particles and move away from metal surface.

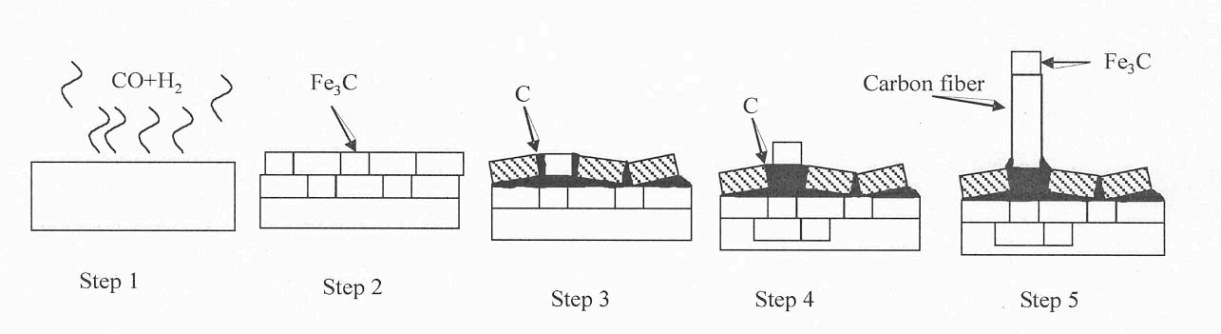

Figure 4.8. Process of metal dusting and carbon filament growth through Fe_3C.

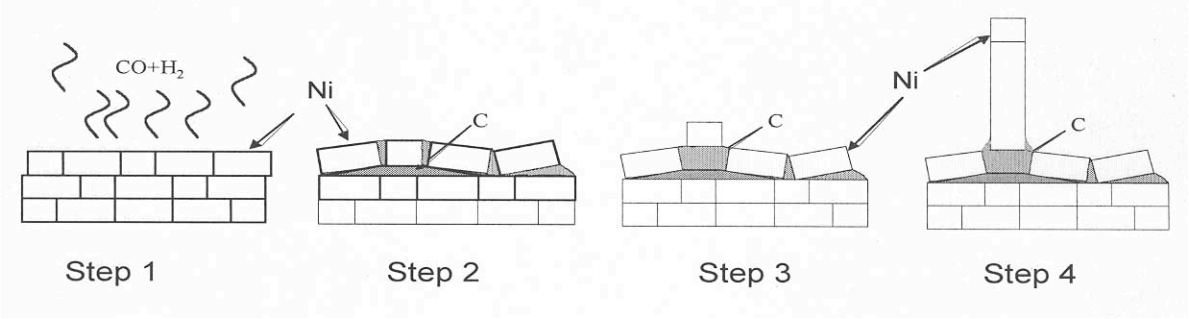

Figure 4.9. Process of metal dusting and carbon filament growth through Ni.

4.5 Questions and Answers Regarding Proposed Mechanism

Question 1: Carbon diffusion through Fe_3C is extremely slow, a factor 10^{-6} slower than through α-Fe. Is the transformation of disordered carbon to well-crystallized graphite possible by C diffusion through cementite?

Answer: There are two factors that determine the precipitation rate of carbon from cementite and Fe. First is the energy barrier on the surface of cementite and iron, which is related to fitness of the lattice between graphite and iron and cementite. The other is the diffusion rate of carbon in iron and cementite.

We know that the diffusion rate of carbon in cementite is 10^{-6} smaller than that of α-Fe. However, it was reported that 1-μm-thick cementite can be grown in 6 min (Pippel et al. 1995), which indicates that carbon can diffuse through at least 1 μm in 6 min. The average particle size in coke is only 27 nm, which means that carbon can precipitate out of cementite after only diffusing through 27 nm (only ≈40 lattice cells of cementite). Carbon can diffuse through this distance in a relatively short time if it can diffuse 1000 nm in 6 min. Since metal dusting is a slow process (loss of only 0.55 mg/cm^2 in 1 h), diffusion of carbon may not be the controlling factor in metal dusting corrosion, but the energy barrier on the surface for the carbon precipitation may be the controlling factor.

Question 2: Is the free energy difference from poor to well crystallized carbon too small to lead to metal dusting corrosion?

Answer: Metal dusting is a slow process, which may take one or more years to form a small pit on many of the alloys. Therefore, it is reasonable to assume that the driving force is small. Otherwise, metal dusting corrosion will proceed very fast.

Two parts contribute to the free energy difference from poor to well crystallized carbon. The first part arises from the disorientation between graphite planes. Single-crystal graphite has a total interlayer binding energy of ≈3 kcal•mol^{-1} (Peacock 1960). Therefore, the maximum energy contribution from interlayer disorientation is ≈3 kcal•mol^{-1}. The other part comes from intra-layer disorder. This part could be much larger than that of interlayer disorientation. At the utmost case, each atom separates to form the most disordered gaseous state. The crystallization energy from carbon gas to well crystallized graphite is 139 kcal•mol^{-1}. The initial state of carbon deposited on the metal surface is very disordered. The free energy difference between this carbon and the well crystallized graphite should be much larger than the difference between polycrystalline graphite and single-crystal graphite. However, this energy should not be as high as 139 kcal•mol^{-1}. The maximum disordering energy should be determined by carbon activity. The chemical potential of carbon in gas $\mu_C = \mu^o + RT\ln a_C$. The larger the carbon activity, the higher the potential for carbon to deposit into solid phase, and the more disordered the carbon that forms. Therefore, the possible free energy difference from this carbon to the well crystallized graphite increases with increasing carbon activity.

We deposited carbon at 704°C from a carburizing gas onto a quartz tube, which is a non-catalytic surface. The carbon was very disordered with an interlayer distance 4.026 Å, which is 20% larger than that in single-crystal graphite. The disordering energy for carbon deposited at 704°C onto a non-catalytic surface is at least 2 kcal•mol^{-1}. We could not collect enough carbon for X-ray diffraction when we deposited carbon at 593°C, since the deposition rate was too low. However, the carbon deposited at 593°C on a non-catalytic surface must be more disordered than that deposited at 704°C. Therefore, the disordering energy of carbon that deposited on a non-catalytic surface at 593°C should be larger than 2 kcal•mol^{-1}, as calculated from interlayer disorientation. If we include the part of disorder energy from intra-layer disordering, the overall free energy difference from disordered carbon to well crystallized carbon would be more than 3 kcal•mol^{-1}. The decomposition free energy of Fe_3C at 593°C is only 1 kcal•mol^{-1}. According to Hochman's mechanism, this energy of 1 kcal•mol^{-1} is enough to lead to the decomposition of Fe_3C and to metal dusting. The disordering energy of the 3 kcal•mol^{-1} is more than sufficient to initiate metal dusting, as discussed in the proposed mechanism.

Question 3: Is Fe_3C stable? If Fe_3C decomposes, does this mechanism still work?

Answer: Since carbon can diffuse through iron, we assume that the catalytic carbon crystallization through iron is similar to that through Ni metal. Therefore, the mechanism still works even though Fe_3C decomposes in some cases. However, if Fe_3C does not decompose, the Hochman mechanism should not work.

The ΔG of the reaction $Fe_3C = 3Fe + C$ is –1.02 kcal•mol^{-1}, which means Fe_3C is not thermodynamically stable. However, the ΔG only tells us that the reaction could go by this direction, but it does not mean that the reaction must happen. Neutron diffraction experimental results showed that Fe_3C is thermodynamically stable at 593°C. Above 640°C, the energy of the cementite lattice is high enough to pass the energy barrier to decompose. At high carbon

activity, cementite could be stable. It has been reported that when cementite decomposes, the resistance of the material will change (Lee and Simkovich 1988). However, when the carbon activity is >5.9, the resistance of cementite did not change for 200 h, which indicates a lack of decomposition in 200 h.

Question 4: When particle size is too small, the nano-particles will not be detected by XRD and magnetic measurements. This is why XRD and magnetic measurement do not indicate iron in the final products of metal dusting, although iron carbide has already decomposed to iron and carbon. Is Hochman's mechanism right, although no iron was detected by XRD and magnetic measurement in the final products of metal dusting?

Answer: Recently, nanotechnology has become an active field of research. It is not difficult to find X-ray patterns for nanoparticles of iron. When the particle size is extremely small, X-rays may not show clear diffraction peaks. However, the average metal particle size in coke is 20-30 nm. Transmission electron microscopy (TEM) observation also showed that the metal particle size is in the range of 20-80 nm (Pippel et al. 1995). X-ray diffraction should be able to detect these particles. In Fig. 4.11, X-ray diffraction patterns of iron nanoparticles with 6-18-nm size and Fe_2O_3 with 3-5-nm size are clearly shown (Bermejo et al. 1997). When the particle size is less than a critical size of 8 nm, ferromagnetic particles become superparamagnetic (Bermejo et al. 1997). Its properties would be different. However, the particle size is larger than the critical size in the current study and in the past studies referenced above.

It is possible that TEM can find small Fe particles. However, Pippel et al. (1995) reported that a 1-μm Fe_3C layer can be grown on an iron surface within 6 min and the iron surface was totally covered by Fe_3C layer in 20 min. If an iron particle of 1000 nm becomes Fe_3C in 6 min, what is the lifetime of 20-80 nm iron particles when exposed in such a carburizing atmosphere? They should become Fe_3C quickly. Pippel et al. (1995) reported metal particles with size 20-80 nm. However, no SAD (selected area diffraction) pattern was shown to prove the particles are iron phase instead of Fe_3C phase. High-resolution electron microscopy (HREM) image is not enough to distinguish the phases.

Question 5: Does graphite grow into Fe_3C?

Answer: It has been observed directly by TEM that graphite grows into Fe_3C (Pippel et al. 1995). The carbon atoms attach to the graphite planes growing more or less perpendicular into the carbide; the iron diffuses outward and aggregates to nanoparticles. We trust this observation that graphite grows into Fe_3C. To answer this question and link this observation to the metal dusting mechanism, we need to revisit the fundamental solid-state reaction principle, since the decomposition $Fe_3C=3Fe+C$ is a pure solid-state reaction.

The structure of Fe_3C is actually related to the structure of Fe. The structure of Fe_3C is described as a framework of almost close-packed iron atoms held together by metallic bonding with small carbon atoms in the largest interstices (Chun et al. 1999). The decomposition of Fe_3C is a solid-state reaction, which is different with gas or solution reaction. In gas or solution reaction, if a molecule decomposes the products generally move away immediately. However, in solid-state reaction, such as the decomposition of Fe_3C, the Fe and C atoms need time to slowly

diffuse away. We do not deny the possibility that Fe atom can diffuse though graphite. However, the small carbon atom should be easier to diffuse out after Fe_3C decomposes, and the larger Fe atoms should move little since they diffuse slowly. Since the lattice of Fe_3C is held together by metallic bonding in a framework of almost close-packed iron atoms with the small carbon atoms in the largest interstices, it is reasonable that the small carbon atoms in the interstice diffuse out and the Fe framework stays there in the process of Fe_3C decomposition.

Figure 4.12 shows the image that was interpreted as graphite growing into cementite. The dark area is cementite, and the bright area is graphite. The iron element content in the graphite is only 0.5% by energy dispersive X-ray spectroscopy, and iron particles are never found in the graphite layer (Pippel et al. 1995). The authors surmised that iron diffused out though graphite by the mechanism shown in the insertion of the left-bottom part of Fig. 4.12.

We strongly disagree with the above interpretation. When Fe_3C decomposes, the products will contain three parts of iron and one part of carbon. The above interpretation requires that the three parts of iron, which constitute the framework of Fe_3C, transport faster than the one part of carbon, which is in the interstice and more mobile. This violates the principle of solid-state reaction. If the carbon in Fig. 4.12 comes from the decomposition of Fe_3C, the microstructure of cementite/Fe/C should be observed. However, the authors observed only cementite/C microstructure (Pippel et al. 1995), which indicates that the carbon in Fig. 4.12 comes from the deposited carbon instead of the decomposition of Fe_3C.

The right schematic diagram in Fig. 4.12 shows our explanation to this image. Carbon diffuses through Fe_3C and precipitates at the defects. The accumulation of carbon separates the particle into two pieces, as shown in Fig. 4.13. Because carbon in the defect came from the diffusion of carbon through Fe_3C instead of the decomposition of Fe_3C, no Fe was observed in this image. The experimental results presented in this report validate this interpretation.

Question 6: How to explain the effect of sulfur on metal dusting corrosion?

Answer: The activation energy for the reaction $CO+H_2=H_2O+C$ is high, and the reaction cannot go forward without a catalyst. For example, when gas with a composition of $72.4H_2$-$8.1CO_2$-$17.2CO$-$2.3H_2O$ was passed through a quartz tube without any catalyst (or metal specimens) at 593°C for 100 h, there was no carbon deposition in the quartz chamber. Metals such as Fe and Ni work as catalyst for the reaction $CO+H_2=H_2O+C$ to proceed. It is well known that sulfur is an element that can poison the catalyst surface. If the surface of metallic materials is covered by sulfur, iron cannot work as a catalyst to enable the carbon deposition reaction. A Fe_3C layer may be able to form by the following reaction: $CO+3Fe+H_2=Fe_3C+H_2O$. However, metals would not be oversaturated with carbon since there is not enough carbon deposition.

The effect of sulfur on metal dusting can be explained at the atomistic level by the mechanism that we have proposed. The crystallization of carbon is assisted by Fe_3C or by iron, since the b axis of Fe_3C (6.744 Å) is very close to the c axis of graphite (6.708 Å). Fe_3C provides an excellent orientation for the growth of graphite, as shown by Fig. 4.14. However, the structure and properties of the surface are altered when sulfur is adsorbed and stays on the surface or interface of Fe_3C. The energy barrier for carbon atoms to move out of the Fe_3C lattice

can increase, and sulfur blocks not only carbon deposition but also retards carbon precipitation out of Fe_3C (Fig. 4.14). This will decrease the availability of carbon and the driving force for metal dusting.

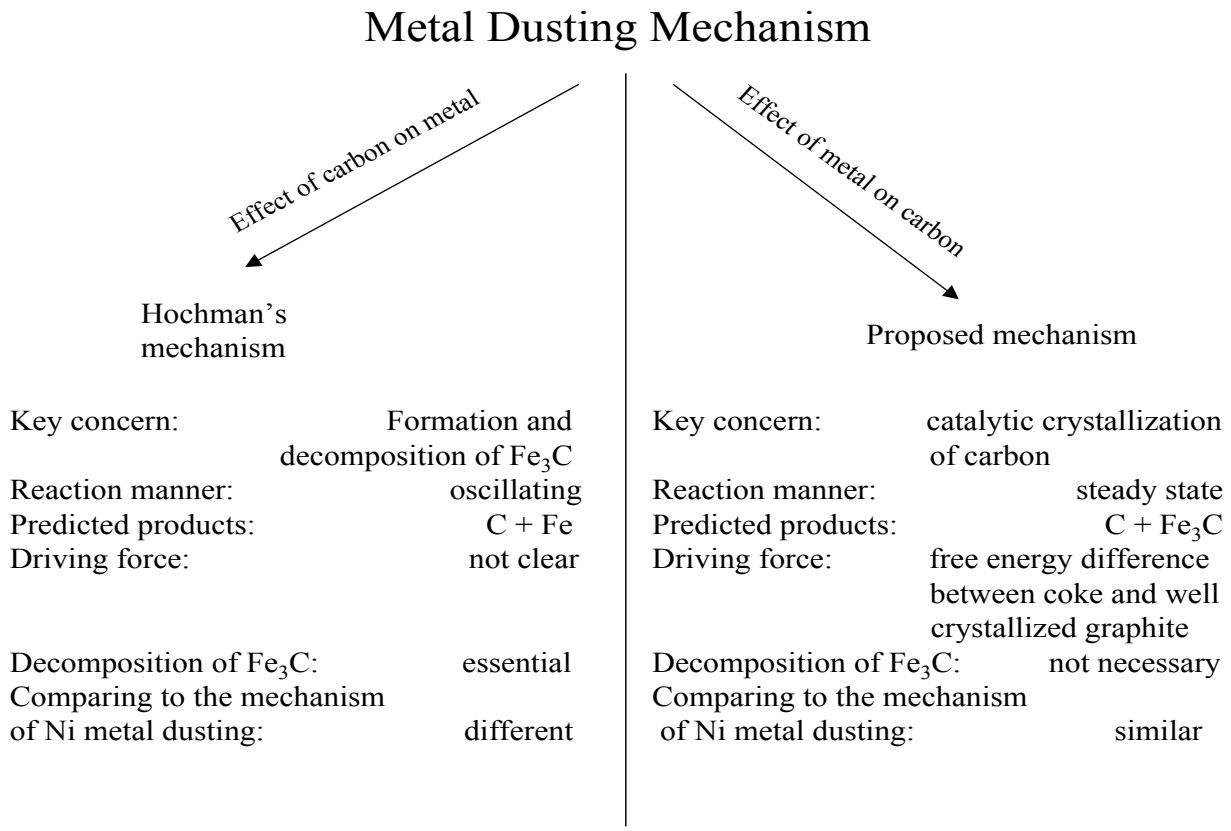

Figure 4.10. Comparison of the proposed mechanism with Hochman's mechanism for metal dusting of iron.

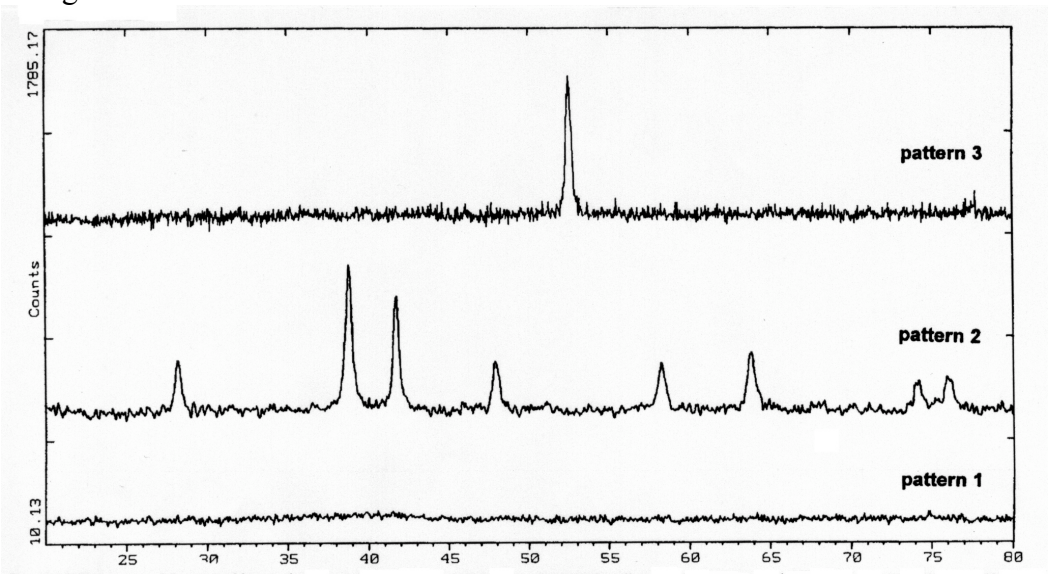

Figure 4.11. XRD patterns for (1) amorphous precursor, (2) Fe_2O_3 with 3-5-nm particles of iron, and (3) Fe_2O_3 with 6-8-nm particles of iron made by reduction of nanoparticles (Bermejo et al. 1997).

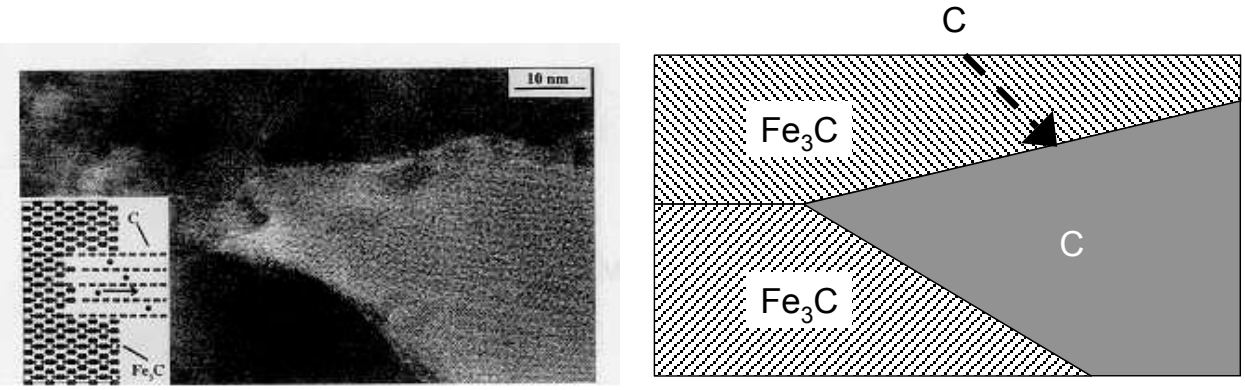

Figure 4.12. Illustration of decomposition of Fe_3C TEM image from Pippel et al. 1997 (left). Schematic to explain the TEM image by the proposed mechanism (right).

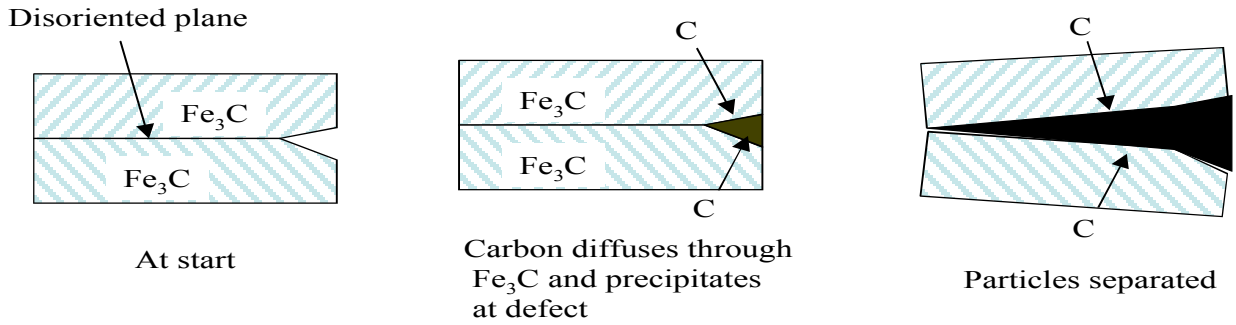

Figure 4.13. Mechanism of graphite growth into cementite. Carbon dissolved, diffused through Fe_3C, and precipitated at the disoriented defect. Accumulation of carbon at the defect tore the particle into two pieces.

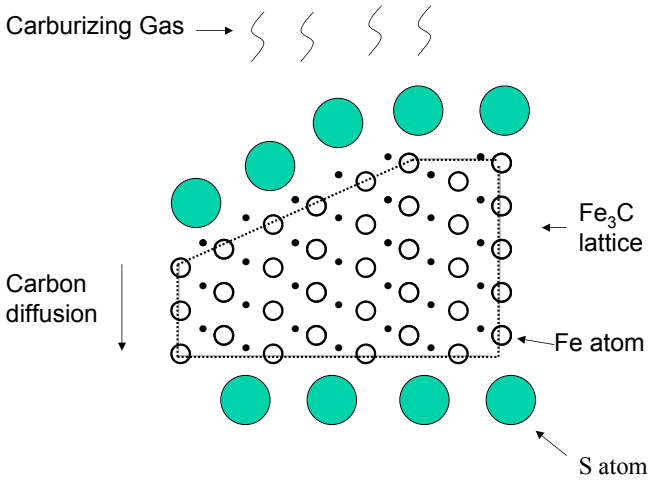

Figure 4.14. Effect of sulfur on metal dusting. Big sulfur atoms distort the surface structure and retard the carbon deposition and crystallization.

5. EFFECT OF COMPOSITION OF OXIDE SCALE ON METAL DUSTING CORROSION OF IRON-BASE ALLOYS

5.1 Introduction

Oxide scales are reported to play an important role in preventing alloys from metal dusting corrosion since carbon does not diffuse through the oxide layers (Grabke et al. 1998, 1993). Because oxide scales are important in metal dusting corrosion, it is necessary to study the effect of their composition and defects on metal dusting. However, the phase composition of oxide scales has been rarely investigated since the oxide layer is too thin to be detected by conventional X-ray diffraction (XRD). Raman spectroscopy is an excellent tool to study the phases in thin oxide layers. The presence of possible phases such as Cr_2O_3, $FeCr_2O_4$, and Fe_3O_4 in the oxide scales has been studied by Raman scattering (Farrow et al. 1980, Thierry et al. 1988, Renusch et al. 1996). The most intense Raman bands for Cr_2O_3 and Fe_3O_4 are at 550 and 670 cm^{-1}, respectively. In this study, we used Raman spectroscopy combined with other techniques to study the phase composition of oxide scales and the relationship between phase composition and metal dusting.

5.2 Experimental

Three gas compositions were used for this study (see Table 1.1). Gas 2 is a simulation of a reformer outlet gas consisting of $52H_2$-$5.6CO_2$-$18CO$-$1.1CH_4$-$23H_2O$. Gas 2b consisted of $66.2H_2$-$7.1CO_2$-$23CO$-$1.4CH_4$-$2.3H_2O$. Its steam content is only 1/10 of the water concentration of Gas 2, but the other constituent gases have similar relative compositions as in Gas 2. By comparing the test results of the two gases, we obtained information regarding the effect of steam on metal dusting corrosion. Gas 11 consisted of $79.5H_2$-$18.2CO$-$2.3H_2O$.

5.3 Metal Dusting Corrosion of Fe-base Alloys in Gas 2b

Table 5.1 shows the weight loss of virgin alloys after exposure at 593°C for 1000 h in Gas 2b. Little mass loss occurred for the alloys except T22, a low alloy steel with 95 wt% Fe and only 2.3 wt% Cr. This alloy lost weight heavily since there was no Cr_2O_3 protective scale on the surface. Its surface was covered by carbon. No pit was observed on the T22 surface, indicating that metal dusting corrosion proceeds uniformly in the absence of a protective oxide scale. Pits were observed on alloys T91, 800, 803, 321, and 321L (Fig. 5.1). T91 has the largest pit (~2 mm in diameter). Figure 5.2a shows the cross section of a metal dusting pit in T91. A dark layer is observed near the surface of the pit area. No such dark layer appears in the region without the pit, where an oxide layer with thickness ~1 μm is observed (Fig. 5.2b). A dark layer is also observed in the pit area in 321L (Fig. 5.3). Energy dispersive X-ray spectroscopy (EDX) showed the dark layer to contain a significant amount of carbon. According to the new mechanism, carbon should diffuse through metal or carbide and insert itself into the defects of metal and carbide. This insertion may be the cause for the cracks shown in Fig. 5.3b.

It was suggested that an oxide scale protects alloys, and metal dusting corrosion starts at defects in the oxide scale (Grabke 1998, Grabke et al. 1993, 1998). Carbon penetrates through the defects and undermines the oxide scale. Pits finally grow to round shapes at the defects. The

defect density is high at the edges of the specimens. Therefore, most of the pits in T91 appear at the edges. An oxide layer with thickness ~2 μm was observed on the surface of Alloy 800 (Fig. 5.4). X-ray diffraction (XRD) of the layer showed the major phases to be spinel and Cr_2O_3 (Fig. 5.5). The oxide layer was destroyed at the pit area. Alloy 800 had pits everywhere on its surface. This finding indicates that the oxide scale on Alloy 800 is not good enough to protect it from metal dusting corrosion. For 321L and T91, dark high-carbon layers appear only around the pit area, where no oxide layer was present to retard the diffusion of carbon. However, a uniform dark layer appeared under the oxide layer and in the pit area of Alloy 800. Carbon seemed to diffuse uniformly through the oxide layer in Alloy 800 and led to severer metal dusting corrosion than in Alloy 321L.

Table 5.1. Weight loss data for alloys after 1000-h exposure at 593°C in gas mixture $66.2H_2$-$7.1CO_2$-$23CO$-$1.4CH_4$-$2.3H_2O$

Alloys	Mass loss (mg/cm^2h)	Visual examination
T22	0.5	Heavy carbon deposition
T91	0.066	Pits
153MA	0	Clean surface
253MA	0	Clean surface
321L	$2.2x10^{-4}$	Pits
310	0	Clean surface
800	0.045	Pits
803	0	Pits
38815	0	Clean surface
MA956	0	Clean surface
321	$3.8x10^{-3}$	Pits
APMT	0	Clean surface
4C54	0	Clean surface

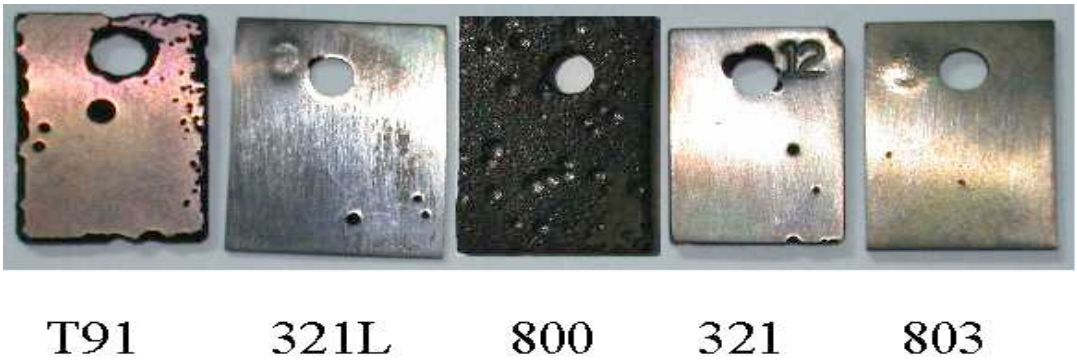

Figure 5.1. Metal dusting pits in Alloys T91, 321L, 800, 321, and 803 after 1000-h exposure in Gas 2b at 593°C.

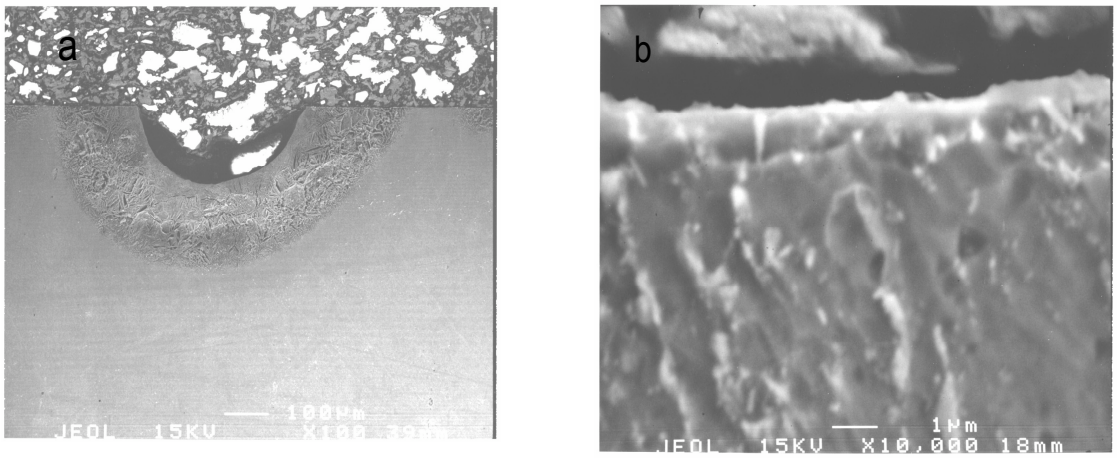

Figure 5.2. SEM micrographs of metallographic cross section of Alloy T91 after exposure in Gas 2b (66.2H_2-7.1CO_2-23CO-1.4CH_4-2.3H_2O) at 593°C for 1000 h. a: pit area; b: non-pit area.

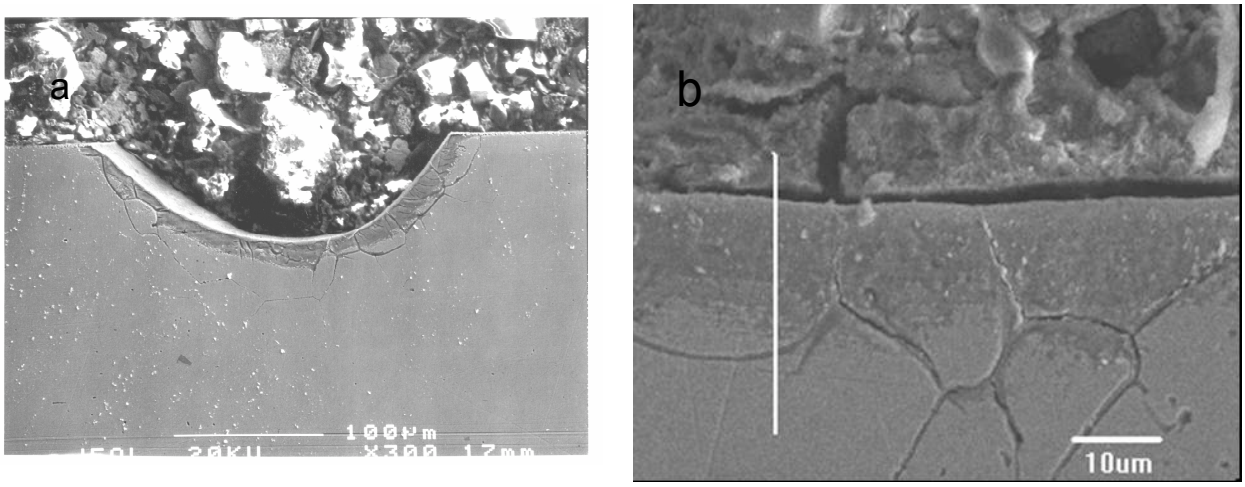

Figure 5.3. SEM micrographs of metallographic cross section of Alloy 321 after exposure in Gas 2b (66.2H_2-7.1CO_2-23CO-1.4CH_4-2.3H_2O) at 593°C for 1000 h. a: metal dusting pit; b: crack observed at the surface of pit area.

5.4 Metal Dusting Corrosion in Gas 2

When the metal dusting tests were run in a high-steam atmosphere, T22 was the only alloy that was attacked by metal dusting (Table 5.2). However, its corrosion rate was much lower than that observed in the low-H_2O atmosphere (Table 5.1). To understand the dramatic difference, Raman spectroscopy and XRD were used to study the surface oxide scales.

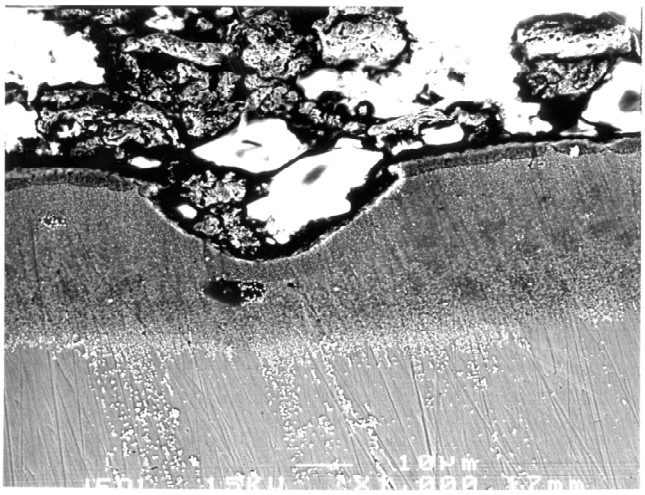

Figure 5.4. SEM micrograph of cross section of Alloy 800 after 1000-h exposure in Gas 2b ($66.2H_2$-$7.1CO_2$-$23CO$-$1.4CH_4$-$2.3H_2O$) at 593°C.

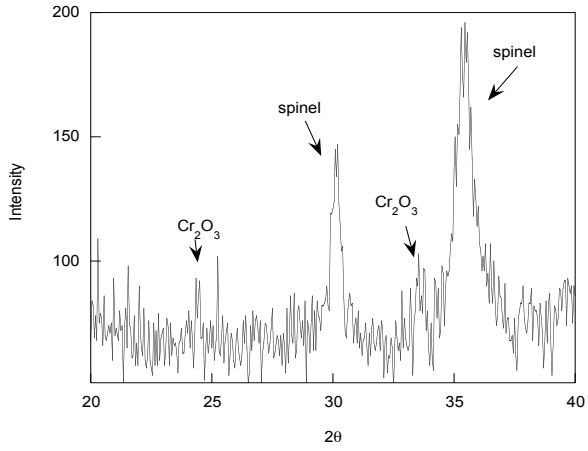

Figure 5.5. X-ray diffraction of oxide scale on the surface of Alloy 800 after 1000-h exposure in Gas 2b ($66.2H_2$-$7.1CO_2$-$23CO$-$1.4CH_4$-$2.3H_2O$) at 593°C.

5.5 Stability of Fe_3O_4 in Carburizing Atmosphere

Figure 5.6 shows two Raman bands at 540 and 670 cm^{-1} for specimen T22 tested in the high-H_2O atmosphere. The two Raman bands correspond to Fe_3O_4 phase (Thierry et al. 1988). In contrast, no Raman band of oxides was observed for the specimen tested in the low H_2O atmosphere. X-ray diffraction of the oxide scales on T22 also showed that Fe_3O_4 is the major phase in the high-H_2O atmosphere (Fig. 5.7), but Fe_3C is the major phase of the oxide scale in the low-H_2O atmosphere (Fig. 5.8). These results indicate that H_2O can stabilize the Fe_3O_4 phase, which can function as a protective scale to retard carbon from diffusing into the alloy when the H_2O concentration is high. Figure 5.9 shows the oxygen/carbon thermochemical

Table 5.2. Weight loss data for alloys after exposure at 593°C for 1000 h in gas mixture $52H_2$-$5.6CO_2$-18CO-$1.1CH_4$-$23H_2O$

Alloys	Mass loss (mg/cm^2h)	Visual examination
T22	$7.6x10^{-3}$	Carbon deposition
T91	0	Clean surface
153MA	0	Clean surface
253MA	0	Clean surface
321L	0	Clean surface
310	0	Clean surface
800	0	Clean surface
803	0	Clean surface
38815	0	Clean surface
MA956	0	Clean surface
321	0	Clean surface
APMT	0	Clean surface
4C54	0	Clean surface

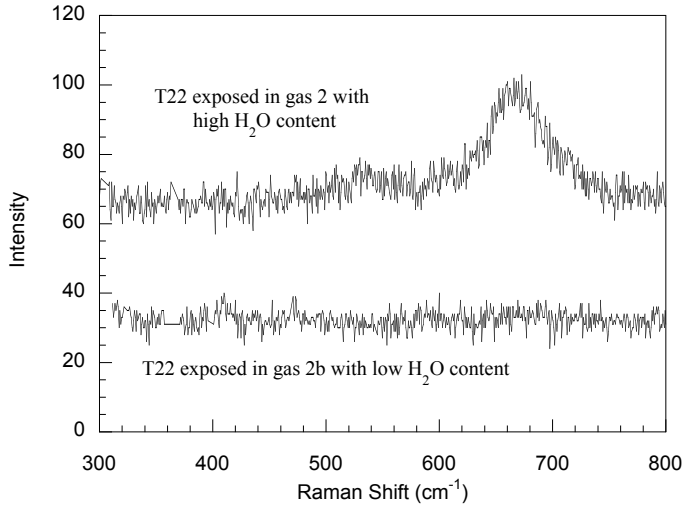

Figure 5.6. Raman spectra of Alloy T22 exposed in different gas atmospheres.

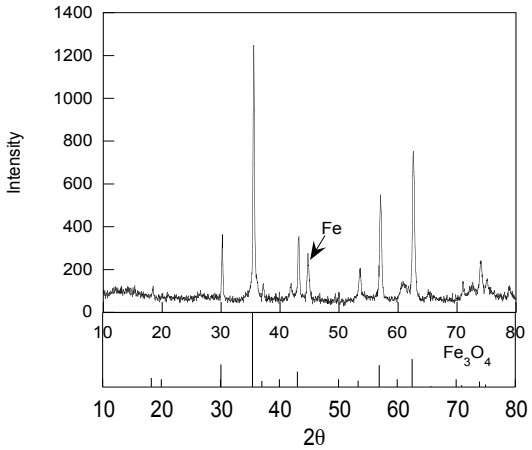

Figure 5.7. XRD on the surface of Alloy T22 after 1000-h exposure in Gas 2 ($52H_2$-$5.6CO_2$-$18CO$-$1.1CH_4$-$23H_2O$) at 593°C.

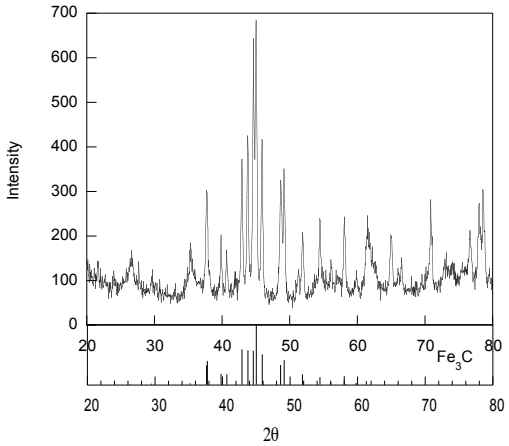

Figure 5.8. XRD on the surface of Alloy T22 after 1000-h exposure in Gas 2b ($66.2H_2$-$7.1CO_2$-$23CO$-$1.4CH_4$-$2.3H_2O$) at 593°C.

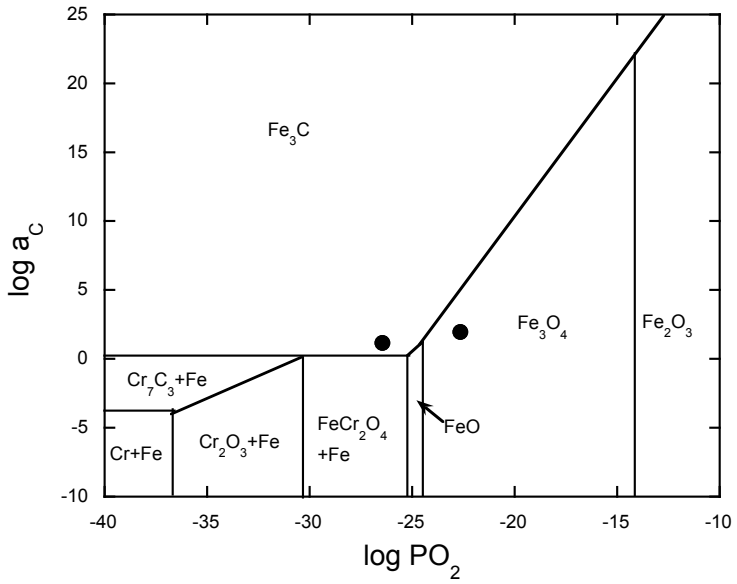

Figure 5.9. Thermochemical diagram showing the stability region of Fe_3C and Fe oxides at 593°C. The two dark circles correspond to the high- and low-pO_2 environments used.

diagram for iron oxide at 593°C. Fe_3O_4 is stable in high H_2O gas, but not in low-H_2O gas. This explains why the metal dusting rate of T22 is much lower in gas containing high than low H_2O. Carbon activity of Gas 2b (a_C=33) was higher than that of Gas 2 (a_C=1.8). Higher carbon activity may also lead to faster metal dusting corrosion. However, the 16-times-higher carbon activity of Gas 2b may not able to account for the metal loss rate of Alloy T22 in Gas 2b being 56 times higher than that in Gas 2. The oxide layer on T22 separated carburizing gas with metal.

Carbon had to diffuse through oxide to attack metal. The oxide layer formed on T22 in Gas 2 made a primary contribution to slow down metal dusting corrosion, although lower carbon activity in Gas 2 may also make a secondary contribution. Fe_3O_4 cannot totally stop the diffusion of carbon into metal. Therefore, metal dusting corrosion was still observed on T22, although the corrosion is much slower than that without a Fe_3O_4 protective layer.

5.6 Relationship Between Phase Composition of Oxide Scale and Alloy Composition

The most intense Raman band from Cr_2O_3 is the peak at 551 cm^{-1} (Thierry et al. 1988). For alloys exposed in Gas 2 (high H_2O concentration), the intensity of the strongest band of Cr_2O_3 increased with increasing Cr content in the alloys (Fig. 5.10). Two phases, Cr_2O_3 and $(Fe,Cr)_3O_4$, were usually observed for Cr-containing Fe-base alloys. There is also a broad band from 400 to 800 cm^{-1} with a peak position at ≈660 cm^{-1}. The sharp Cr_2O_3 and spinel bands pile up on the broad band. Figure 5.11 shows a fit to the broad Raman band for Alloy 153MA. The intensity of the broad band also increases with increasing Cr content. The broad band is an indication of a third phase in the oxide scale. At present, the composition of the third phase is not established. Renusch et al. (1996) reported that this broad band could be observed on pure Cr metal when the metal is oxidized at low temperature. Spinel-like Cr_3O_4 may be responsible for the band. Cr_3O_4 is not stable in normal condition. However, it may be possible to form thin Cr_3O_4 film on the surface of Cr metal since Cr continues to diffuse into the oxide layer and lead to a dynamic equilibration. Although a powder sample of Cr_3O_4 is not available for measurement, reflection high-energy electron diffraction (RHEED) and secondary ion mass

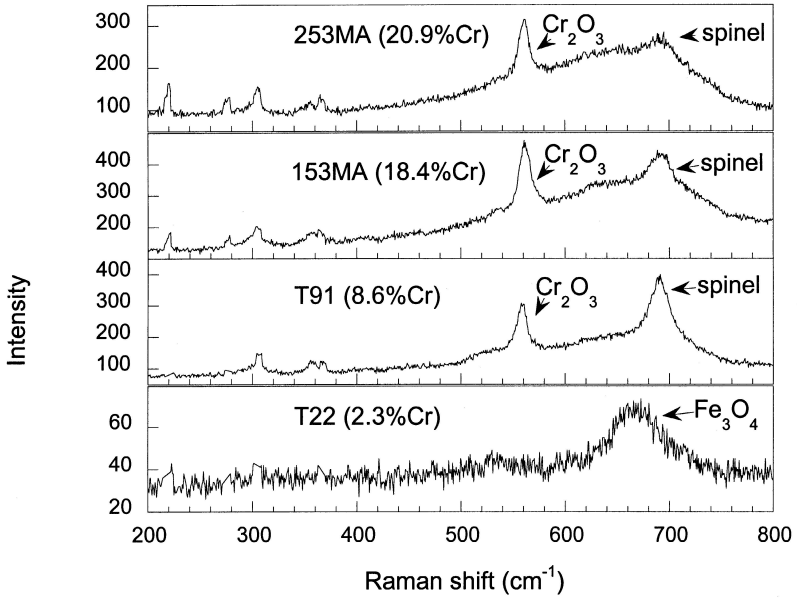

Figure 5.10. Raman spectra of Alloys T22, T91, 153MA, and 253MA after 1000-h exposure in Gas 2 ($52H_2$-$5.6CO_2$-$18CO$-$1.1CH_4$-$23H_2O$) at 593°C.

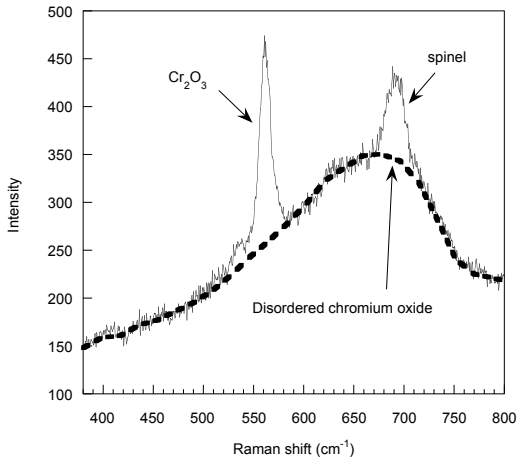

Figure 5.11. Simulated fit of broad band in Fig. 5.10 for Alloy 153MA. Cr_2O_3 and spinel Raman bands pile up on broad band (dash line), which may be caused by disordered chromium oxide.

spectrometry (SIMS)/Auger experiments showed that Cr_3O_4 with a spinel structure might exist on the surface of Cr when the metal is oxidized at low temperature. A second possible source of the broad band could be disordering of Cr_2O_3. It is known that iron doping of Cr_2O_3 leads to a disorder-induced Raman band in the neighborhood of 670 cm^{-1} (Renusch et al. 1996, McCarty and Boehme 1989). The chromium oxide that forms on Cr metal may contain oxygen vacancies. Its composition may vary from Cr_3O_4 to Cr_2O_3. The disordered chromium oxide with oxygen vacancies may also lead to the broad Raman band.

Figures 5.12 and 5.13 show the Raman spectra for the rest of the alloys exposed to Gases 2 and 2b, respectively. On the MA956 and APMT alloys that contain 4-5 wt% Al, strong fluorescence from Al_2O_3 was observed. The γ-phase Al_2O_3 (which will be stable alumina at low temperature) is almost featureless with a broad fluorescence background. The fluorescence masks the Raman lines of Cr_2O_3 and spinel (Fig. 5.13). Amorphous SiO_2 is also almost featureless and was not observed on Alloy 38815. However, since alloys that contain Al and Si show the best resistance to metal dusting corrosion among the 13 alloys studied, it is likely that Al_2O_3 and SiO_2 scales play an important role in preventing alloys from metal dusting attack. Of the thirteen alloys, 4C54 has the highest Cr content and also shows no metal dusting corrosion after 1000-h exposure in both gas environments.

5.7 Stability of Oxides in Carburizing Atmosphere

Raman spectroscopy of the scales on Fe-Cr alloys shows that they may contain three phases: Cr_2O_3, disordered chromium oxide, and $(Fe,Cr)_3O_4$ spinel. To study the reaction of these oxides with carburizing gas, Cr_2O_3, $(Fe,Cr)_3O_4$ spinel, and Cr metal were tested in Gas 2 at 593°C in a thermogravimetric test apparatus. Disordered chromium oxide and Cr_2O_3 formed on the surface of Cr metal. Weight gains of $FeCr_2O_4$, Cr_2O_3, and Cr metal were almost zero. Although the carbon activity of Gas 2 was >1 at 593°C, the deposition of carbon on Cr_2O_3, disordered chromium oxide, and $FeCr_2O_4$ is very difficult since the activation barrier is high for the following reactions:

$CO + H_2 = C + H_2O$

$2CO = C + CO_2$

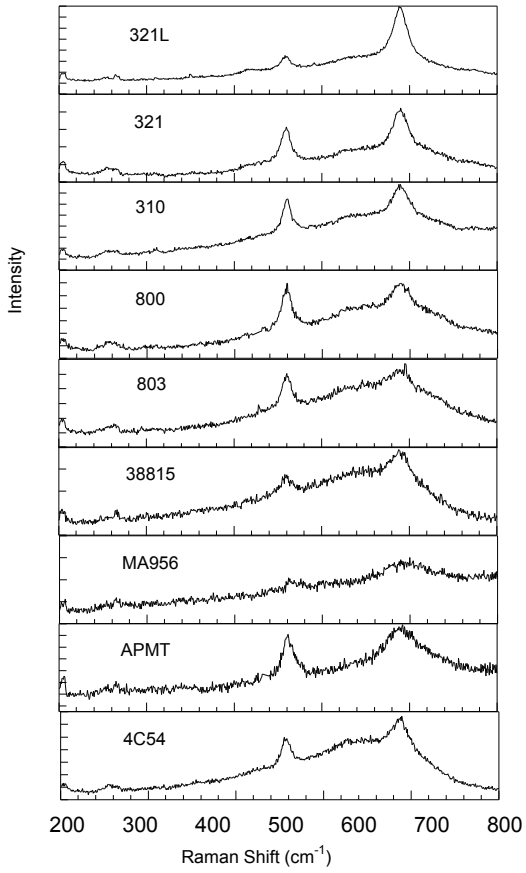

Figure 5.12. Raman spectra of Alloys 321L, 321, 310, 800, 803, 38815, MA956, APMT, and 4C54 after 1000-h exposure in Gas 2 ($52H_2$-$5.6CO_2$-$18CO$-$1.1CH_4$-$23H_2O$) at 593°C.

If the alloy surface is totally covered by Cr_2O_3, disordered chromium oxide, and $FeCr_2O_4$, carbon deposition may not occur, and in turn, metal dusting will not occur if carbon deposition is retarded by Cr_2O_3, disordered chromium oxide, and $FeCr_2O_4$ scales. However, weight gain was observed for $Fe_{1.8}Cr_{1.2}O_4$, and the carbon deposition rate in $Fe_{2.4}Cr_{0.6}O_4$ was much larger than that of $Fe_{1.8}Cr_{1.2}O_4$ (Figure 5.14). Therefore, a spinel with high iron content seems to catalyze the reaction and lead to deposition of carbon.

Cr_2O_3 is stable in carbon and hydrogen atmospheres down to very low P_{O2}. This oxide works as an excellent protective layer in preventing alloys from metal dusting corrosion. $Fe(Cr_{1-x}Fe_x)_2O_4$ spinel, on the other hand, is not as stable as Cr_2O_3. The composition of the spinel can change from $FeCr_2O_4$ [x=0 in $Fe(Cr_{1-x}Fe_x)_2O_4$] to Fe_3O_4 (x=1). As mentioned above, Fe_3O_4 is not stable when the H_2O concentration is low. The stability of $FeCr_2O_4$ is higher than that of Fe_3O_4, but lower than that of Cr_2O_3. If there are no defects, $FeCr_2O_4$ should be stable in

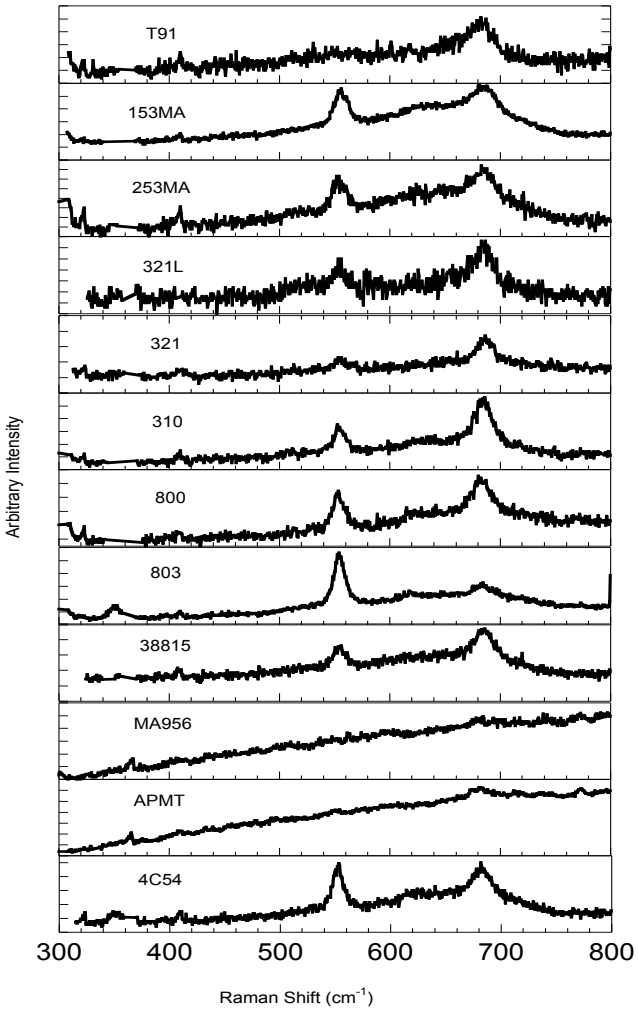

Figure 5.13. Raman spectra of Alloys T91, 153MA, 253MA, 321L, 321, 310, 800, 803, 38815, MA956, APMT, and 4C54 after 1000-h exposure in Gas 2b ($66.2H_2$-$7.1CO_2$-$23CO$-$1.4CH_4$-$2.3H_2O$) at 593°C.

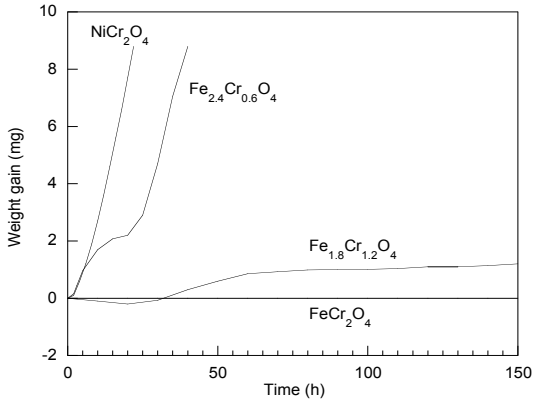

Figure 5.14. Weight change for spinels during exposure in Gas 2b ($66.2H_2$-$7.1CO_2$-$23CO$-$1.4CH_4$-$2.3H_2O$) at 593°C.

Gas 2b. However, Vuuren et al. (1992) reported that $FeCr_2O_4$ starts to be partially reduced by carbon at 600°C. Figure 5.15 shows that the X-ray peak position of spinel on the surface of Alloy 800 is between Fe_3O_4 and $FeCr_2O_4$, and the peak is also much broader than that of polycrystalline Fe_3O_4 and $FeCr_2O_4$. We conclude that the spinel on the surface of alloys is not stoichiometric $FeCr_2O_4$, but has a higher iron content and may also contain defects.

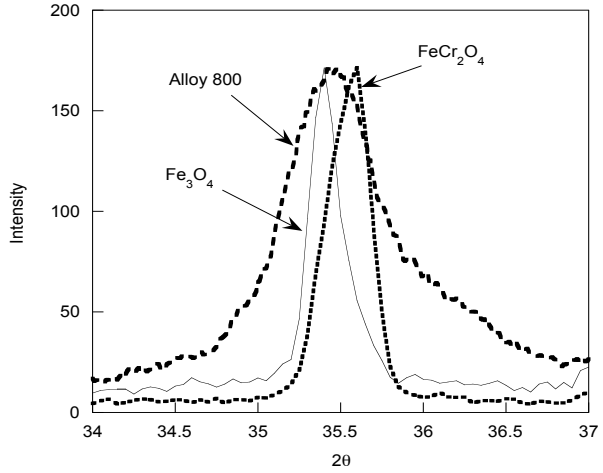

Figure 5.15. XRD for Fe_3O_4, $FeCr_2O_4$, and oxides on Alloy 800 after 1000-h exposure in Gas 2b ($66.2H_2$-$7.1CO_2$-$23CO$-$1.4CH_4$-$2.3H_2O$) at 593°C.

The higher the concentration of iron in $Fe(Cr_{1-x}Fe_x)_2O_4$, the easier for the spinel reduction. The rate of Fe/Cr in spinel may vary with oxygen partial pressure in gas. Spinel with high iron content cannot form when P_{O2} is low. The chance to form a spinel with high iron content increases with increasing P_{O2} in gas. When the P_{O2} in gas such as Gas 2 is higher than 7×10^{-26} atm, the most undesirable spinel Fe_3O_4 could form. There is a critical oxygen partial pressure in gases. When P_{O2} in gas is higher than the critical value (7×10^{-26} atm at 593°C), all types of spinels are stable: increasing steam content in gas will increase the stability of desirable spinel and lead to a low metal dusting rate. However, when P_{O2} in gas is below the critical value, increasing P_{O2} may result in the formation of spinel with high Fe/Cr ratio that is easy to be attacked by carbon and leads to metal dusting corrosion.

It is difficult to measure the iron content in the oxide layer because it is too thin. However, it may be assumed that the iron content in the oxide scale increases with increasing iron content in the alloy. Furthermore, the iron concentration may not be uniform in the oxide scale. Some spots with high iron content may react with carbon first. Metal dusting will start from those regions. Figure 5.10 shows that 153MA has less spinel phase in the oxide scale than does T91; therefore, 153MA has fewer defects susceptible to attack by metal dusting corrosion than does T91. This observation has been further substantiated since the mass loss rate of 153MA is much less than that of T91.

Alloy 800 has a similar chromium content as Alloy 253MA but more nickel. Usually, Ni-base alloys perform better than Fe-base alloys in metal dusting environments. However, the ability of Alloy 800 to resist metal dusting corrosion is much worse than that of Alloy 253MA. This trend is hard to understand on the basis of conventional wisdom. Raman spectra show that

the intensity ratio of the 550 cm^{-1} band (Cr_2O_3) to the 684 cm^{-1} band (spinel) for Alloy 800 (I_{Cr2O3}/I_{spinel} =1.2) is less than that of Alloy 253MA (I_{Cr2O3}/I_{spinel} =1.7) (Fig. 5.16). The intensity of the broad band, which is due to disordered chromium oxide, is also stronger in 253MA than in Alloy 800. The higher content of spinel phase in the scale on Alloy 800 is a possible reason that this alloy is more easily attacked by metal dusting corrosion.

Since a laser beam can focus to ≈1 μm, we have been able to analyze the phase composition of the oxide scale at a metal dusting pit in various alloys. Figure 5.17 shows that the phase composition of the oxide scale at a metal dusting pit is different from that at the non-pit area on Alloy 800. Both Cr_2O_3 and spinel phases were observed on the area without pits. However, only spinel was observed at the pit area. This observation also indicates that spinel was easy to be attacked by carbon, and metal dusting occurred at the area where spinel was the major phase. Similar results were observed on Alloy 153MA. Intensity of the Cr_2O_3 band from the pit area was much lower than that from the non-pit area (Fig. 5.18).

5.8 Change of Phase Composition of Oxide Scales with Exposure Time

Figure 5.19 shows that the phase composition of the oxide scale on Alloy 800 changed with exposure time. The intensity of the Cr_2O_3 band decreased with exposure time, and the intensity of spinel band increased with exposure time.

The increasing content of spinel in oxide scales may be due to the outward diffusion of iron. Chromium is easier to oxidize than iron. At the initial state, chromium oxide first formed on the surface of alloys. Therefore, a strong spinel band was observed in Raman spectra. The diffusion of iron in the oxide scales is faster than that of chromium. Therefore, iron gradually diffused out after long exposure times. The accumulation of iron in the oxide scale leads to changes in phase composition. When spinel (especially with higher Fe content) becomes the major phase, metal dusting corrosion would initiate since the spinel can be easily attacked by carbon.

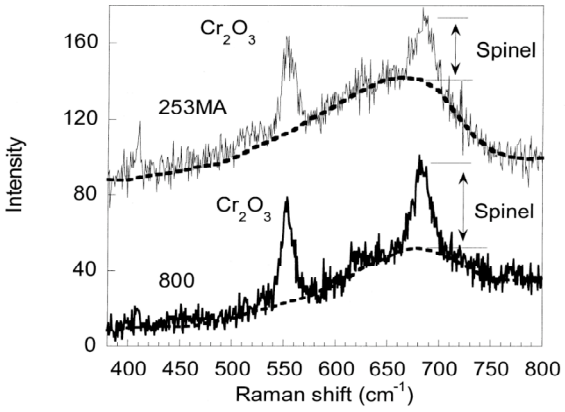

Figure 5.16. Raman spectra of oxide layer on Alloys 253MA and 800.

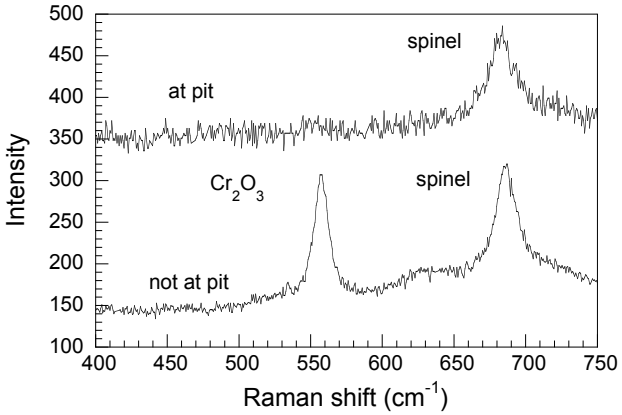

Figure 5.17. Raman spectra of Alloy 800 exposed to Gas 11 at 593°C for 1280 h.

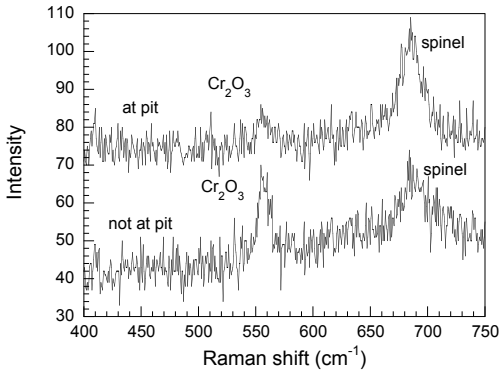

Figure 5.18. Raman spectra of Alloy 153MA exposed to Gas 11 at 593°C for 1280 h.

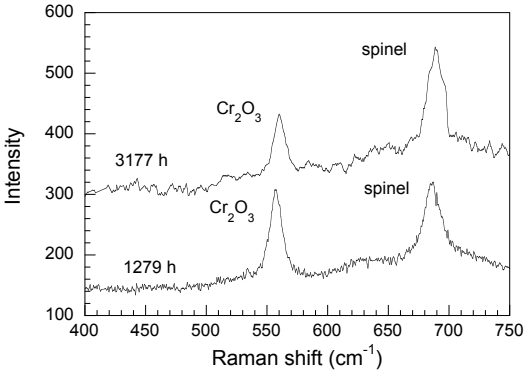

Figure 5.19. Raman spectra of Alloy 800 exposed in Gas 11 at 593°C.

5.9 Conclusion

Two aspects in the scaling process play a role in the initiation and propagation of metal dusting attack. These involve the phases that are present in the oxide scale and the Fe content in the oxide phases. Raman spectra showed the presence of $Fe_{1+x}Cr_{2-x}O_4$ ($0 \le x \le 1$) spinel, Cr_2O_3, and disordered chromium oxide in the scale grown on Fe-Cr alloys that contained 9 wt.% or more Cr. All three phases act, at different degrees, as protective layers to resist metal dusting corrosion. Among these phases, Cr_2O_3 is the most protective, followed by the spinel with a high Cr content. However, if the spinel phase contains more Fe, then it can be reduced by carbon, leading to metal dusting. Alloy composition, oxygen partial pressure in the gas mixture, and alloy pretreatment can affect the composition of the phases that form in the surface oxide scales.

Increasing the steam content in the exposure environment can lead to spinel formation in addition to chromia. The amount of steam in the environment dictates the Fe content of the $Fe_{1+x}Cr_{2-x}O_4$ ($0 \le x \le 1$) spinel. With an increase in steam content, the Fe content of the spinel increases, which is detrimental from the standpoint of its resistance to reduction by carbon.

Steam has two effects on metal dusting. First, high steam content in the atmosphere provides a high Po_2 and stabilizes the spinel phase. This effect is good for reducing the metal dusting rate when compared with the rate observed in the absence of any surface oxide. Second, high Po_2 may lead to an increase in the Fe content of the spinel, which is not good for resistance to metal dusting. However, metal dusting will be retarded, if steam content is much higher than a critical value, at which high Po_2 stabilizes even the most undesirable spinel. Therefore, the metal dusting rate in high steam gas is much lower than that in low steam gas.

6. EFFECT OF PRE-OXIDATION ON METAL DUSTING OF IRON-BASE ALLOYS

6.1 Objectives

If an alloy directly contacts a carburizing gas without a protecting oxide scale on the surface, metal dusting corrosion will start immediately. Therefore, we tried to build an oxide scale on the alloy surface before the alloy contacted a carburizing gas.

6.2 Pre-oxidation Condition

Several alloys were pre-oxidized in a $2.3H_2O$-$97.7H_2$ or $75CO$-$25CO_2$ gas mixture at 900°C for 200 h to develop a protective scale. The pre-oxidized alloys were tested under the same conditions as the specimens without pre-oxidation by exposing them to Gas 2b (Sec. 5.2).

6.3 Metal Dusting Corrosion of Pre-oxidized Fe-base Alloys

We found that the resistance of the alloys to metal dusting was not improved by pre-oxidation. For the $2.3H_2O$-$97.7H_2$ pre-oxidation, weight loss and pits were observed for 153MA and 253MA (Table 6.1), while the two alloys without pre-oxidation were not attacked. Raman spectra show that the ratios of the intensity of the 550 cm^{-1} band (Cr_2O_3) over the 684 cm^{-1} band (spinel) for pre-oxidized specimens are less than those without pre-oxidization (Fig. 6.1). High spinel content in oxide scales correlated with low resistance to metal dusting corrosion. The oxygen pressure in our pre-oxidation gas may be too high, considering that iron was oxidized to form a spinel phase. If an environment that oxidizes only chromium is used, alloys may perform better.

Table 6.1. Weight loss data for alloys after exposure at 593°C for 300 h in gas mixture $66.2H_2$-$7.1CO_2$-$23CO$-$1.4CH_4$-$2.3H_2O$. Specimens were pre-oxidized in a H_2O/H_2 atmosphere at 900°C for 200 h.

Alloys	Mass loss (mg/cm^2h)	Visual examination
T22	0.7	Heavy carbon deposition
T91	0.032	Pits, carbon deposition
153MA	$5.3x10^{-3}$	Pits
253MA	$4.3x10^{-3}$	Dark spots
321L	~0	Pits
310	~0	Light carbon deposition
800	~0	Pits
803	~0	Light carbon deposition
38815	~0	Clean surface
MA956	~0	Dark surface
321	$9.3x10^{-4}$	Pits
APMT	~0	Dark surface
4C54	~0	Dark surface

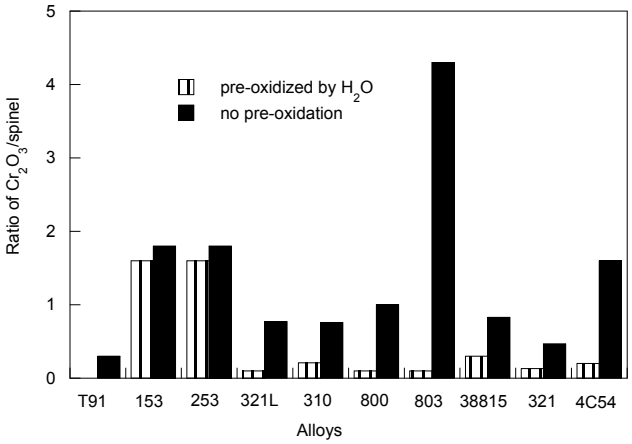

Figure 6.1 Intensity ratio of 550 cm^{-1} band (Cr_2O_3) over 684 cm^{-1} band (spinel) for specimens with and without pre-oxidation in $2.3H_2O$-$97.7H_2$ gas mixture at 900°C for 200 h.

The performance of specimens pre-oxidized by a gas mixture of $75CO$-$25CO_2$ was worse than that of specimens pre-oxidized by a gas mixture of $2.3H_2O$-$97.7H_2$. No weight loss was recorded for Alloys 310, 800, and 803 for specimens pre-oxidized by H_2O/H_2 gas. However, these alloys lost weight after they were pre-oxidized by CO/CO_2 gas and tested in the same metal dusting environments (Table 6.2). The alloys may have carburized in the pretreatment, which can lead to preferential pathways for diffusion of carbon through oxide scales. Figure 6.2 shows the ratios of the intensity of the 550 cm^{-1} band (Cr_2O_3) over the 684 cm^{-1} band (spinel) for pre-oxidized specimens by CO/CO_2. Some alloys have more spinel phase and some have less than in the specimens pre-oxidized by H_2O/H_2 gas.

Table 6.2. Weight loss data for alloys after exposure at 593°C for 300 h in gas mixture $66.2H_2$-$7.1CO_2$-$23CO$-$1.4CH_4$-$2.3H_2O$. Specimens were pre-oxidized in a CO/CO_2 atmosphere at 900°C for 200 h.

Alloys	Mass loss (mg/cm^2h)	Visual examination
T22	0.46	Heavy carbon deposition
T91	0.0099	Pits, carbon deposition
153MA	0.019	Pits
253MA	0.02	Dark surface
321L	0	Dark surface
310	0.053	Dark surface
800	0.083	Pits
803	0.067	Dark surface
38815	0.0001	Clean surface, no pit
MA956	0	Dark surface
321	0.0022	Pits
APMT	0	Dark surface
4C54	0	Dark surface

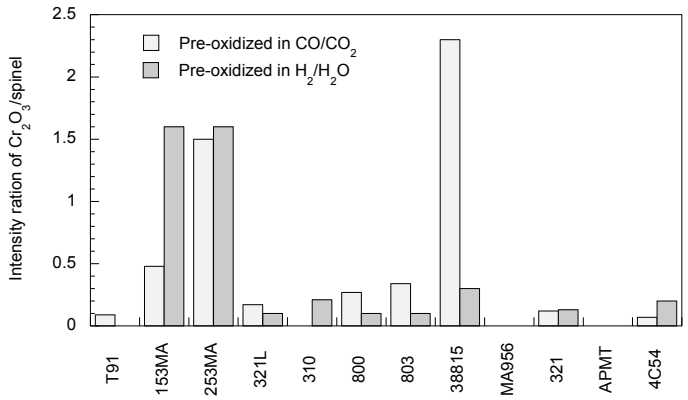

Figure 6.2 Intensity ratio of 550 cm^{-1} band (Cr_2O_3) over 684 cm^{-1} band (spinel) for specimens with and without pre-oxidation in 75CO-25CO_2 gas mixture at 900°C for 200 h.

6.4 Conclusion

Pre-oxidation in a gas of 2.3H_2O-97.7H_2 and a gas of 75CO-25CO_2 at 900°C did not improve the ability of the alloys to resist metal dusting. The performance of pre-oxidized samples was worse than that of the samples without pre-oxidation. There was more spinel phase on the surface of alloys that were pre-oxidized. The spinel phase, especially if it contained a high Fe content, was detrimental and led to an increase in metal dusting corrosion.

7. EFFECT OF SYSTEM PRESSURE AND GAS CHEMISTRY ON METAL DUSTING OF IRON-BASE ALLOYS

7.1 Objectives

It is believed that process variables, such as carbon activity, pressure, temperature, and velocity influence metal dusting. It has been reported that increasing pressure increases metal dusting attack (Maier and Levi 1998, Levi et al. 2002). However, the reason for the pressure effect is not clear, and no long-term results in high-pressure test environments have been reported. For Reactions 1 and 2 (Sec. 1), carbon activities increase with gas pressure. To study the effect of gas pressure on metal dusting, the other variables need to keep constant. Therefore, we exposed alloys in two gas mixtures with similar carbon activity but at different pressures. By comparing the metal dusting behavior of the alloys in the two gases, we developed information on the effect of system pressure on metal dusting.

7.2 Experimental

Alloys 253MA, 310, 800, 38815, MA956, 321, and Ni_3Al were used for this metal dusting test. Specimens were ground on 400 grit SiC paper before exposure to carburizing gases. Two gas mixtures were used for this study. Gas 10 is a simulation of a reformer outlet gas consisting of $53.4H_2$-$5.7CO_2$-18.4CO-$22.5H_2O$. The carbon activity of the gas is ≈31.3 for reaction 1 at 210 psi (14.3 atm) and 593°C. Gas 11 consists of $79.5H_2$-$18.2CO$-$2.3H_2O$, with carbon activity of 31.5 for reaction 1 at 1atm and 593°C. One set of alloys was exposed in Gas 11 at 1 atm and 593°C. Another set was exposed in Gas 10 at 593°C and 210, 400, and 600 psi (14.3, 27.2, and 40.8 atm). After each exposure, specimen weight change was determined after removal of adhering coke in an ultrasonic bath with acetone. Phases present in the coke and metal samples were analyzed by X-ray powder diffraction. The microstructure of each sample was examined with a JSM-6400 scanning electron microscope. To study the metallographic cross section, the samples were electrolytically etched with 10% acetic acid at 10 V for 30 sec.

Raman spectra were excited with 60 mW of 476-nm radiation from a Kr-ion laser. The incident beam impinged on the sample at an angle close to 45° from the normal. Scattered light was collected along the surface normal with an f/1.4 lens. The scattered light was analyzed with a triple Jobin-Yvon grating spectrometer and detected with a CCD detector from Princeton Instruments. All of our spectra were acquired in 300 sec at room temperature.

7.3 Effect of System Pressure on Weight Loss Data for Fe-base alloys

Tables 7.1 to 7.5 show the weight loss of alloys at different pressures. Experiments listed in Tables 7.1 and 7.2 were done at the same conditions, except the gas flow direction was reversed. The metal loss rate of Alloy 800 was the highest of the six alloys. In 100 hours at 210 psi (14 atm), no metal dusting corrosion was observed for all six alloys (Table 7.4). However, when experiments were run at 400 and 600 psi (27 and 41 atm), Alloys 310 and 800 lost weight, and pits were observed (Tables 7.3 and 7.5). Their metal loss rates also increased with increasing pressure. We concluded that increasing pressure could lead to increased corrosion by metal dusting in 100 h. Carbon activity of Gas 11 was lower than that of Gas 10. Therefore,

metal loss rate in Table 7.5 is lower than that in Tables 7.1 and 7.2, although the specimens were run at the same temperature and pressure.

Table 7.1. Weight loss data for alloys (Run 39HP) after 100-h exposure at 593°C and 600 psi (41 atm) in Gas 10.

Alloys	Mass loss (mg/cm^2h)	Visual examination
253MA	0	Clean surface
310	4.04	Pits
800	15.76	Pits
38815	0	Clean surface
MA956	0	Clean surface
321	0	Clean surface

Table 7.2. Weight loss data for alloys (Run 42HP) after 100-h exposure at 593°C and 600 psi (41 atm) in Gas 10. Gas flow direction was reversed from that in Run 39HP.

Alloys	Mass loss (mg/cm^2h)	Visual examination
253MA	0	Clean surface
310	2.49	Pits
800	13.04	Pits
38815	0	Clean surface
MA956	0	Clean surface
321	0.20	Pits

Table 7.3. Weight loss data for alloys (Run 41HP) after 100-h exposure at 593°C and 400 psi (27 atm) in Gas 10.

Alloys	Mass loss (mg/cm^2h)	Visual examination
253MA	0	Clean surface
310	0.19	Pits
800	11.11	Pits
38815	0.24	Clean surface
MA956	0	Clean surface
321	1.03	Pits

Table 7.4. Weight loss data for alloys (Run 49HP) after 100-h exposure at 593°C and 210 psi (14 atm) in Gas 10.

Alloys	Mass loss (mg/cm^2h)	Visual examination
253MA	0	Clean surface
310	0	Clean surface
800	0	Clean surface
38815	0	Dark surface
MA956	0	Clean surface
321	0	Clean surface

Table 7.5. Weight loss data for alloys (Run 43HP) after 100-h exposure at 593°C and 600 psi (41 atm) in Gas 11.

Alloys	Mass loss (mg/cm^2h)	Visual examination
253MA	0	Clean surface
310	0	Clean surface
800	1.93	Pits
38815	0	Clean surface
MA956	0	Clean surface
321	0.23	Pits

Alloys 310, 800, and 321 developed pits in both high- and low-pressure experiments (Fig. 7.1). It is reported that formation of pits by metal dusting initiates at defects in oxide scales (Levi et al. 2002). The pits, observed in the present study, were almost perfectly round, and distributed randomly over the surface of the specimens. However, pit density was high at the edges on Alloys 310, 800 and 321, which may be due to the high defect density at the edges. All the pits at the edges of Alloy 800 had coalesced around edges (Fig. 7.2). In contrast with Alloys 310, 800, and 321, the metal dusting corrosion of the silicon-containing alloy 38815 was relatively uniform.

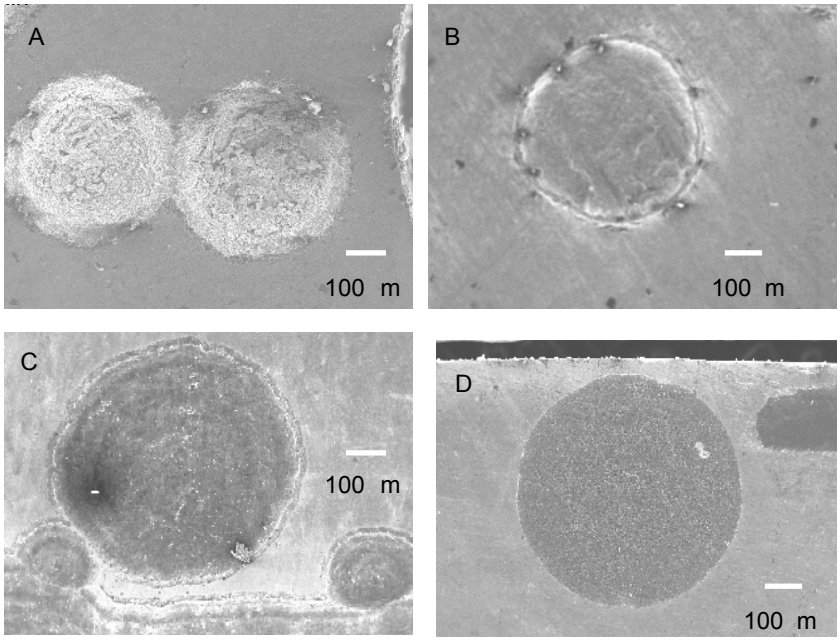

Figure 7.1. SEM micrograph of metal dusting pits on Alloys 800 and 321 after exposure at 593°C. A: Alloy 800 exposed in Gas 10 at 593°C and 210 psi (14 atm) for 1130 h; B: Alloy 321 exposed in Gas 10 at 593°C and 210 psi (14 atm) for 1130 h; C: Alloy 800 exposed in Gas 11 at 593°C and 1 atm for 1280 h; D: Alloy 321 exposed in Gas 11 at 593°C and 1 atm for 1280 h.

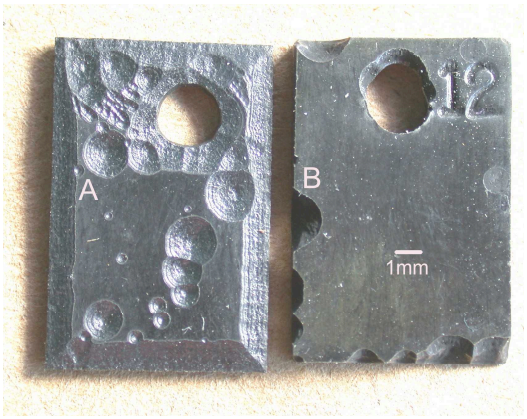

Figure 7.2. Photograph of alloys exposed in Gas 11 at 593°C and 1 atm for 1280 h. Most metal dusting pits appear at edges. Pits at edges of Alloy 800 had coalesced into uniform corrosion; B: Large pits (≈3-mm dia) appear at edges of Alloy 321.

Alloys 253MA, 310, 38815, and 321 lost weight after exposure in Gas 10 at 600 psi (41 atm) for 300 h (Fig. 7.3). Only MA956 and 4C54 alloys were not attacked by metal dusting when exposed under the same conditions. The aluminum addition in MA956 and the high-chromium content in 4C54 (26.7%) may be responsible for their good performance. At 210 psi (14 atm), Alloy 38815 lost weight at a similar rate as Alloy 800 (Fig. 7.4). However, there was almost no weight loss for this alloy when it was exposed to gas with the same carbon activity at 1 atm (Fig. 7.5). The results indicate that silicon and its conversion to silica may not resist metal dusting corrosion at high pressure. No metal dusting corrosion was observed in MA956 after 1100-h exposure in Gas 10 at 593°C and 210 psi (14 atm). Therefore, aluminum addition is superior to silicon addition from the standpoint of protection against metal dusting corrosion at high pressure. Alloy 253MA (1.6 wt.% Si) lost weight at a higher rate at high pressure.

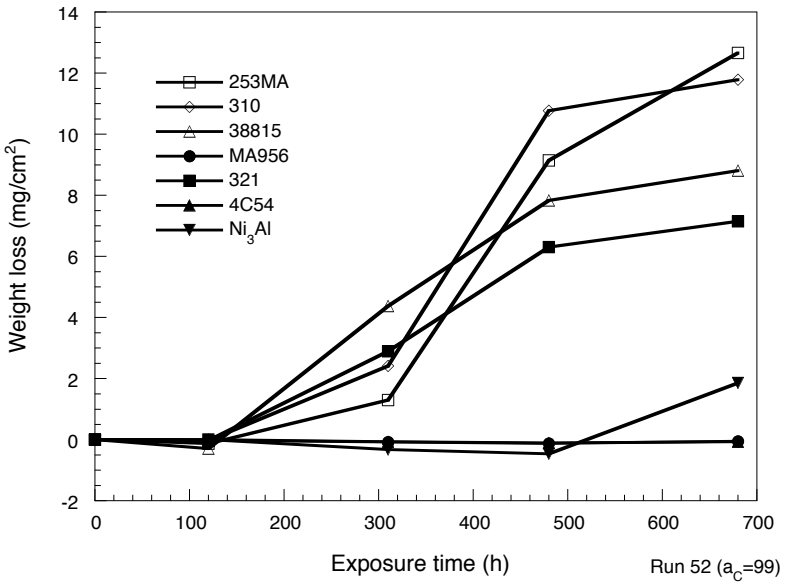

Figure 7.3. Weight loss data for several alloys after exposure in Gas 10 at 593°C and 600 psi (41 atm).

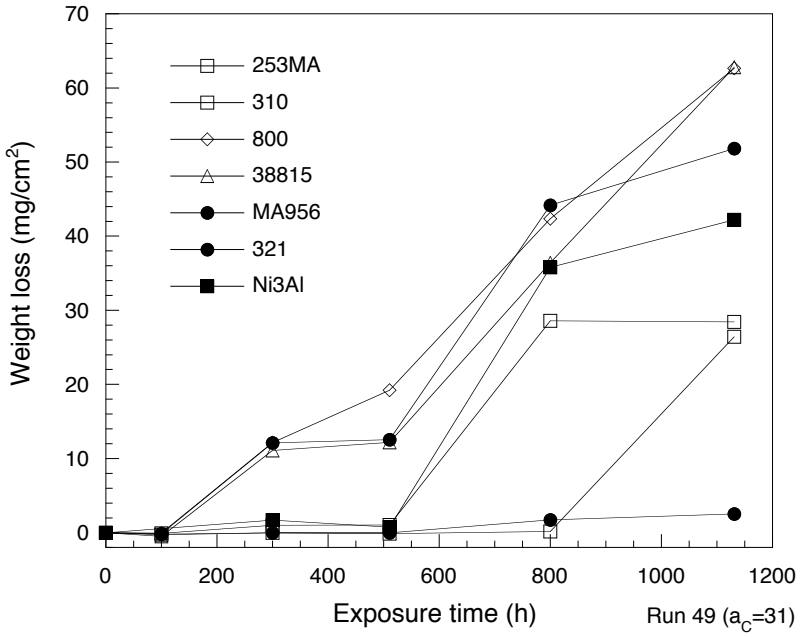

Figure 7.4. Weight loss data for several alloys after exposure in Gas 10 at 593°C and 210 psi (14 atm).

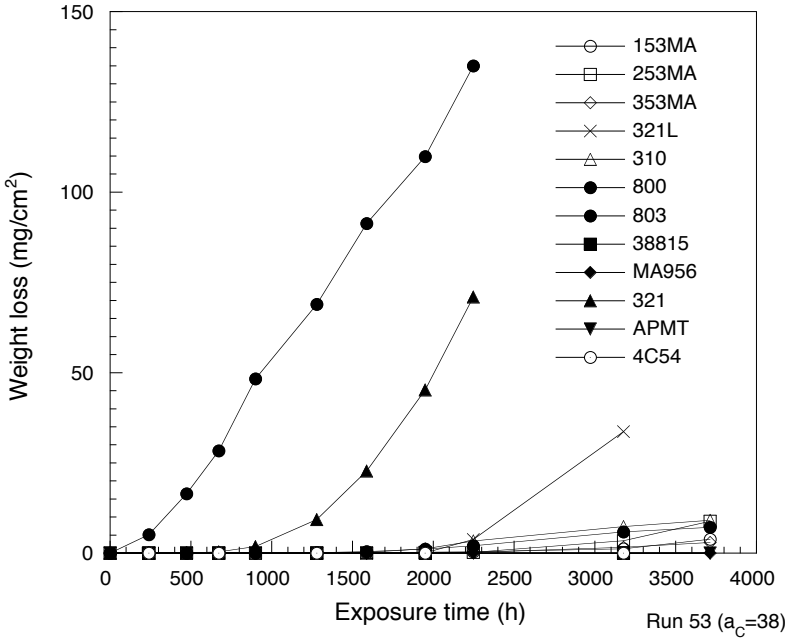

Figure 7.5a. Weight loss data for several alloys after exposure in Gas 11 at 593°C and 1 atm.

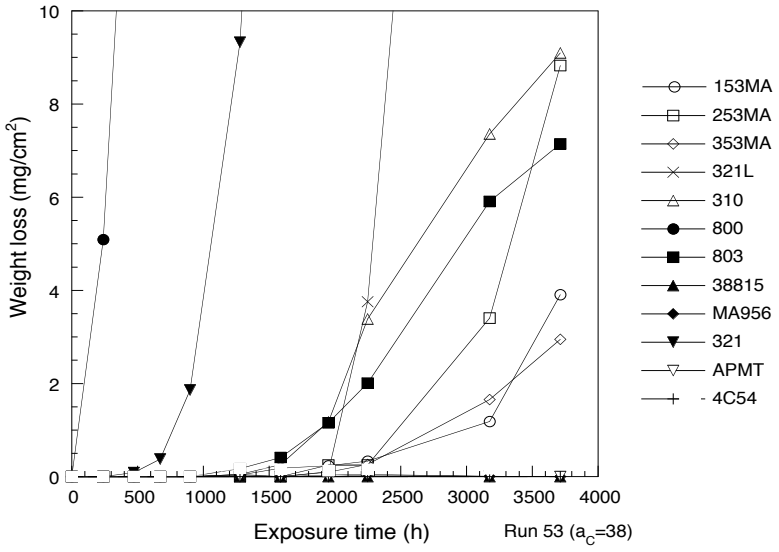

Figure 7.5b. Magnified view of weight loss data for alloys shown in Fig. 7.5a.

7.4 Observations of Oxide Scales and Metal Dusting Pits

Alloy 800 developed an oxide scale with thickness ≈0.6 μm at 593°C and 210 psi (14 atm) in Gas 10 in 1130 h (Fig. 7.6). In the same experimental condition, Alloy 321 developed an oxide scale with a thickness of ≈1.5 μm (Fig. 7.7A). EDX analysis showed that Cr and Fe are the two major metallic elements in the oxide layer (Fig. 7.8). Iron content increased with increasing distance toward the alloy substrate. Chromium content in the oxide layer was higher than that in the alloy substrate because chromium accumulates on the surface after absorbing oxygen. Around defects of oxide scales, carbon penetrated into alloys and led to cracks (Fig. 7.7B). Cracks on the alloy surface will lead to more defects in the oxide scale and accelerate metal dusting attack. Finally, pits were developed (Figs. 7.7 C and D).

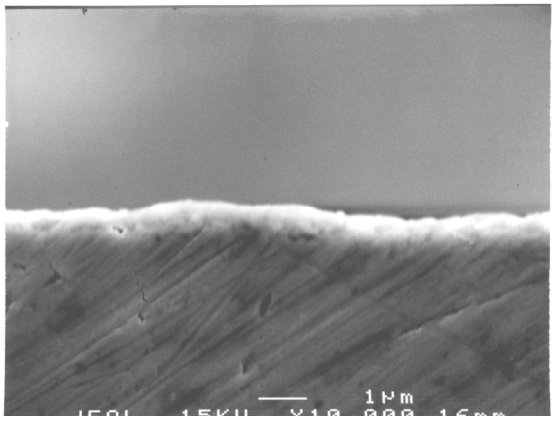

Figure 7.6 SEM micrograph of metallographic cross section of Alloy 800 after 1130-h exposure in Gas 10 at 593°C and 210 psi (14 atm).

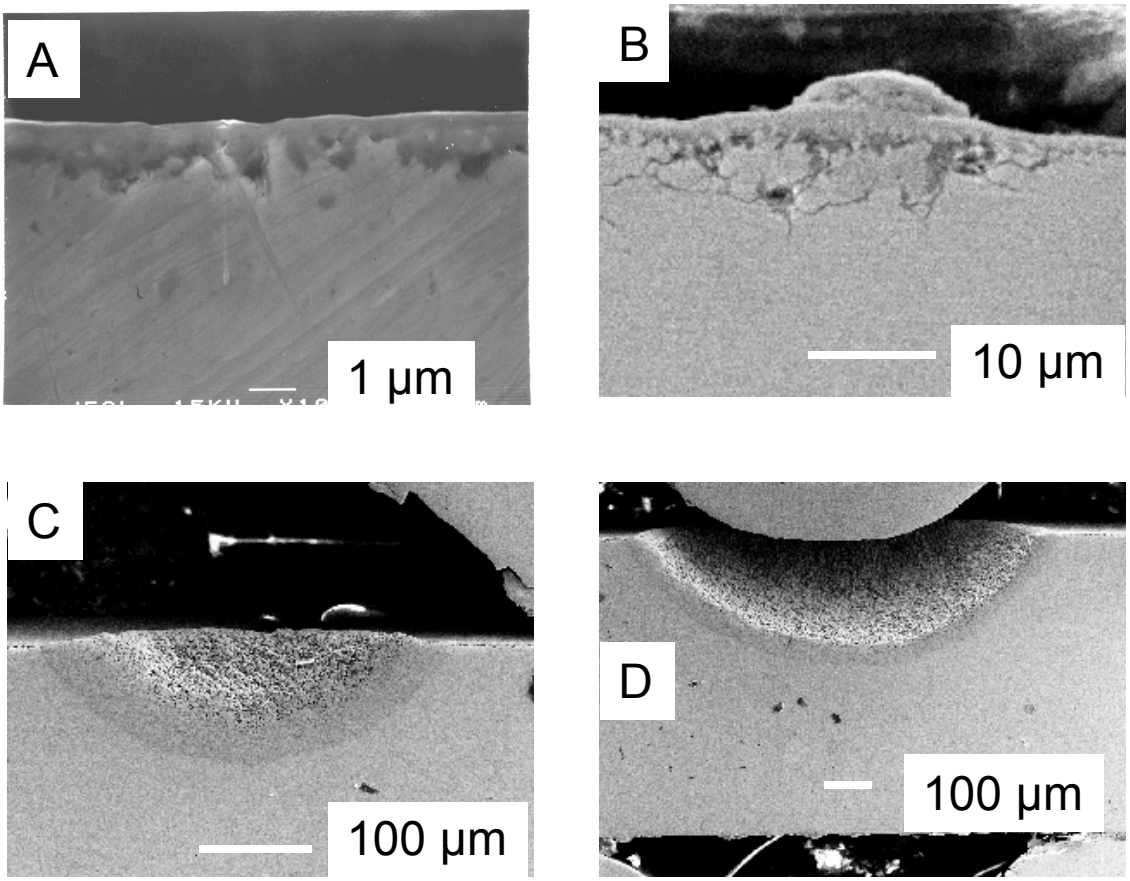

Figure 7.7 SEM micrograph of metallographic cross section of Alloy 321 after 1130-h exposure in Gas 10 at 593°C and 210 psi (14 atm). A: oxide scale in the area without pits; B: oxide scale at the area with defect (alloy substrate cracked after carbon penetration into alloy through the defect); C. a small metal dusting pit; D: a large metal dusting pit.

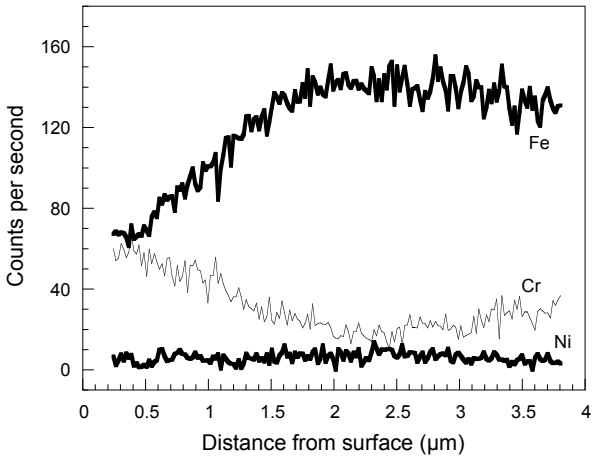

Figure 7.8. EDX analysis results for oxide scale on Alloy 321 at the area without pits after 1130-h exposure in Gas 10 at 593°C and 210 psi (14 am).

Three layers were observed at pits of Alloy 321 (Fig. 7.9). The outer layer was ≈19 μm, and the middle layer was ≈31 μm. EDX analysis showed that the primary elements of the outer layer are Fe and C (Fig. 7.10). The Cr and Ni contents were small in the outer layer. Therefore, the major phase of the outer layer may be Fe_3C and carbon. Carbon bands were observed in Raman spectra at the outer layer (Fig. 7.11). In contrast, there was no iron carbide layer at the non-pit area (Fig. 7.7A). The middle layer contained Fe, but its content was less than that in the outer layer. Contents of Cr and Ni in the middle layer were higher than those in the outer layer and alloy substrate. The middle layer primarily consisted of Cr_2O_3 and spinel. The grain boundary can be observed in the inner layer. Elemental concentrations were constant from the inner layer to alloy. Therefore, the inner layer primarily consisted of metals. The carbon content in both outer and middle layers was almost the same, but its concentration decreased in the alloy substrate. The results indicate that the oxide layer at pits of Alloy 321 cannot prevent penetration of carbon into alloys. In contrast, a dense oxide scale with only 1-2 μm at the non-pit area can stop carbon penetration and further oxidation. The thick middle oxide layer (≈31 μm) at pits may not be a dense oxide scale, and may be a mixture of chromium oxide, spinel, Fe_3C, Ni metal, and carbon, since chromium oxide, spinel, Fe_3C, and Ni metal are all stable phases in Gas 10 and 11. Therefore, carburizing gases can penetrate into alloy at the pit area and lead to further growth of pits.

Figure 7.12 shows the cross section of metal dusting pit in Alloy 800 exposed to Gas 10 at 593°C and 210 psi (14 atm) or 1130 h. In contrast with Alloy 321, only one thin layer (≈3 μm) was observed on the surface of this alloy at pit. EDX analysis showed Fe, Cr, C, and O in this layer. This layer may also consist of a mixture of oxide, carbide, and carbon.

Figure 7.13A shows the Raman spectroscopy of Alloy 800 after being exposed in Gas 10 at 210 psi (14 atm) and 593°C. The most intense Raman band from Cr_2O_3 is the peak at 551 cm^{-1} (Thierry et al. 1988). Two phases, Cr_2O_3 and $(Fe,Cr)_3O_4$, were usually observed for Cr-containing Fe-base alloys. There is also a broad band from 400-800 cm^{-1} with a peak position at ≈660 cm^{-1}. The sharp Cr_2O_3 and spinel bands pile up on the broad band. Figure 7.13B shows a fit to the broad Raman band for Alloy 800. The broad band is possibly due to disordered chromium oxide.

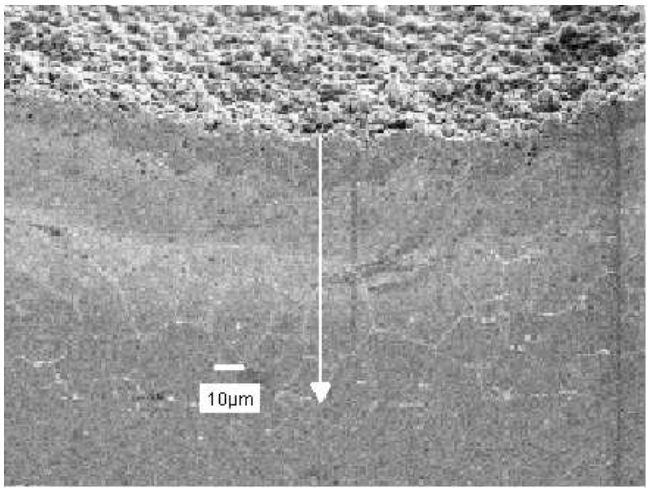

Figure 7.9 SEM micrograph of metallographic cross section of Alloy 321 at a metal dusting pit, which developed during a 1130-h exposure in Gas 10 at 593°C and 210 psi (14 atm).

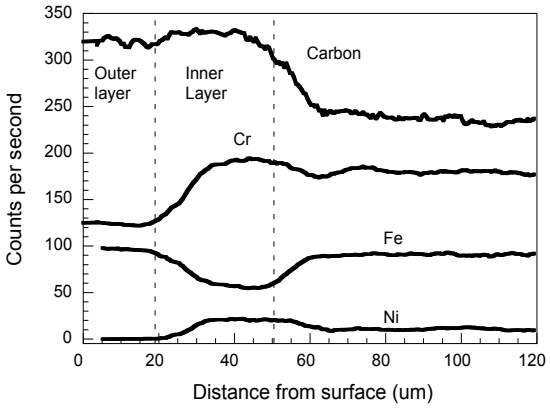

Figure 7.10. EDX analysis results for oxide scale on Alloy 321 in the pit region shown in Fig. 7.9.

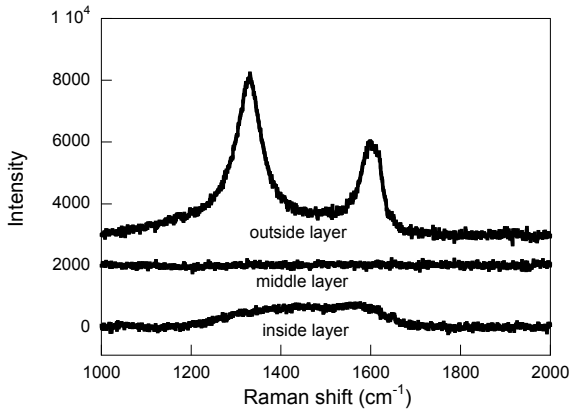

Figure 7.11. Raman spectra at different layers of metal dusting pits of Alloy 321.

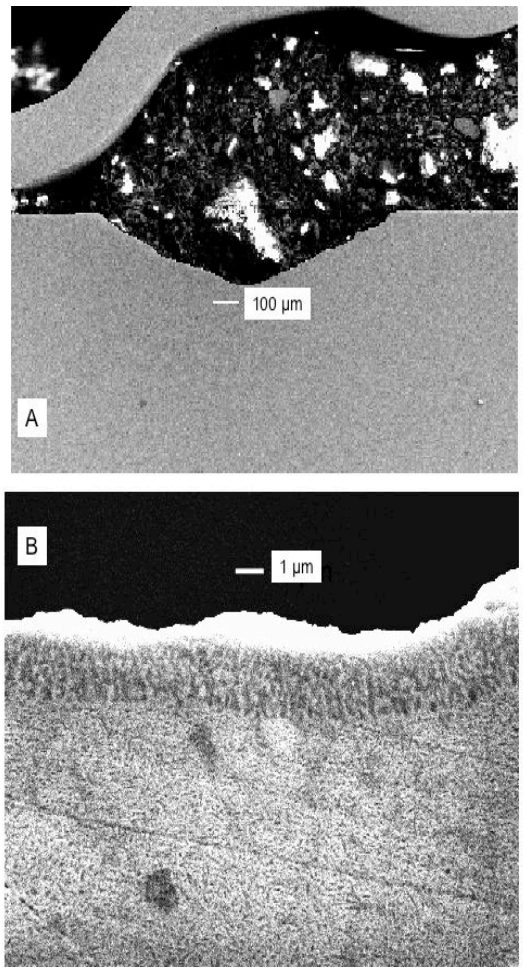

Figure 7.12. SEM micrograph of metallographic cross section of Alloy 800 at a metal dusting pit, developed after 1130-h exposure in Gas 10 at 593°C and 210 psi (14 atm). A: at 90 X; B: at 5000 X.

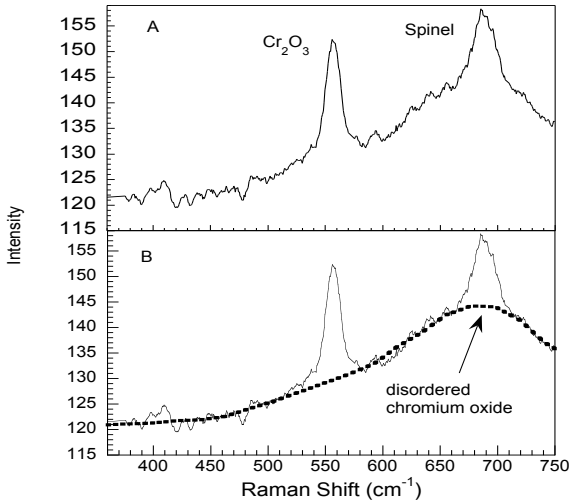

Figure 7.13. A: Raman spectra for Alloy 800 after 1130-h exposure in Gas 10 at 593°C and 210 psi (14 atm). B: Simulated fit of broad spinel region in A. In simulation, Cr_2O_3 and spinel Raman bands superimpose and result in a broad band (dash line) that may be caused by disordered chromium oxide.

Cr_2O_3, disordered chromium oxide, and spinel were also observed in the non-pit area of Alloy 800 exposed in Gas 11 (Fig. 7.14). However, only spinel was observed at the pit area (Fig. 7.15). Since the oxide layer at the pit area is not dense, gases can penetrate into the oxide layer. Cr_2O_3 in pits may be converted to spinel by the following reactions when chromium oxide particles are mixed with Fe_3C particles.

$$6Cr_2O_3 + 2Fe_3C + 3CO_2 = 6FeCr_2O_4 + 5C$$

$$3Cr_2O_3 + Fe_3C + 3CO = 3FeCr_2O_4 + 4C$$

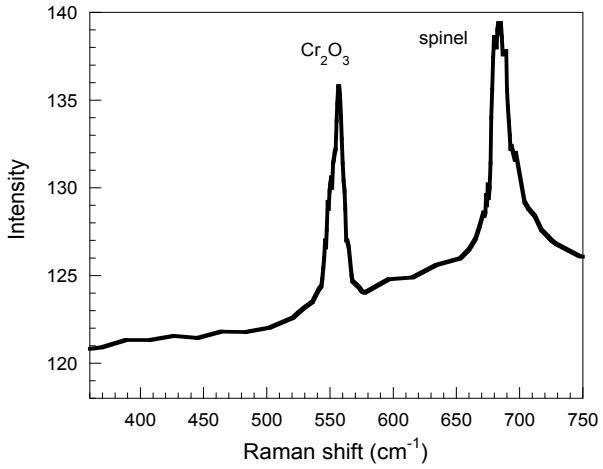

Figure 7.14. Raman spectrum of non-pit area of Alloy 800 after 1280-h exposure in Gas 11 at 1 atm and 593°C.

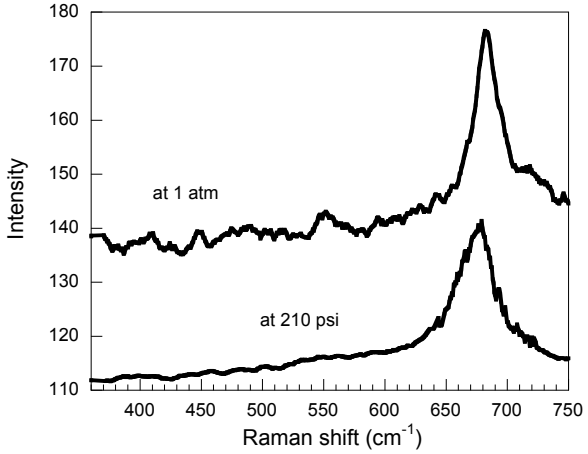

Figure 7.15. Raman spectrum of pit area of Alloy 800 after 1280-h exposure at 593°C in Gas 11 at 1 atm and Gas 10 at 210 psi.

Figure 7.16 shows the Raman spectra of Alloy 321 exposed in Gas 10 at 210 psi (14 atm) and Gas 11 at 1 atm. There are also three phases (Cr_2O_3, disordered chromium oxide, and spinel) on the non-pit area of Alloy 321. At the pit area, the major phase is also spinel; only a small amount of Cr_2O_3 is observed (Fig. 7.17). Even spinel could not be observed at the surface of some pit areas since the oxide layer was covered by a carbide layer, as shown in Fig. 7.9. However, spinel was observed in the cross section of the pit (Fig. 7.18). In the middle layer of the pit in Fig. 7.9, both Cr_2O_3 and spinel were observed. The inner layer may primarily consist of metals. Oxygen pressure was too low to form spinel. Therefore, only Cr_2O_3 was observed in the inner layer.

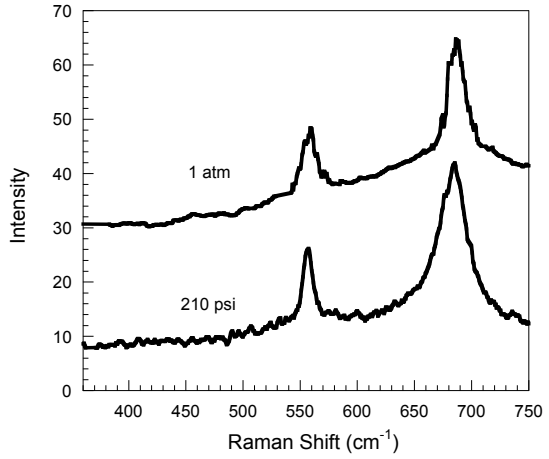

Figure 7.16. Raman spectrum of non-pit area of Alloy 321 after 1280-h exposure at 593°C in Gas 11 at 1 atm and Gas 10 at 210 psi (14 atm).

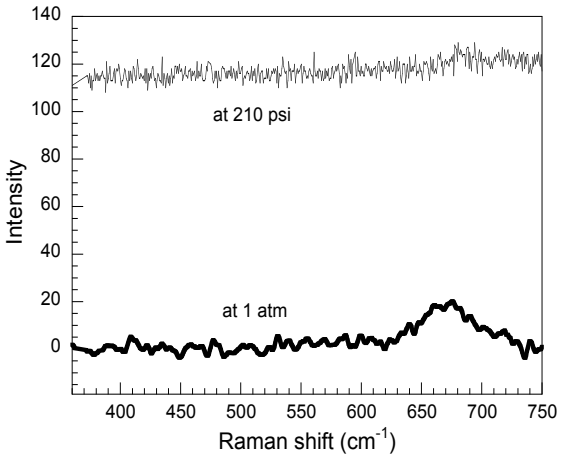

Figure 7.17. Raman spectrum of pit area of Alloy 321 after 1280-h exposure at 593°C in Gas 11 at 1 atm and Gas 10 at 210 psi (14 atm).

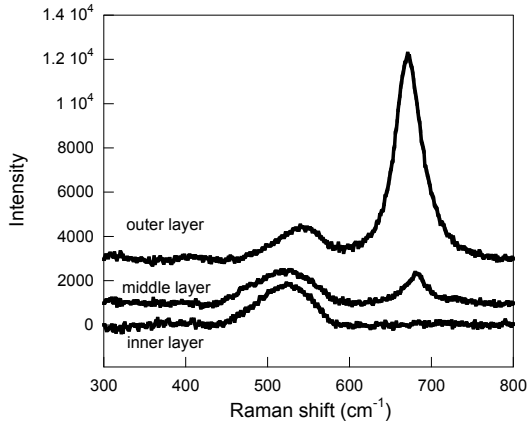

Figure 7.18. Raman spectra at different layers of metal dusting pits of Alloy 321.

7.5 Incubation Time for Metal Dusting at Several System Pressures

Figure 7.19 shows the weight loss of Alloy 800 exposed in Gas 10 at 210 psi (14 atm) and Gas 11 at 1 atm. The metal dusting rate of Alloy 800 was similar at different gas pressures when the carbon activity was similar for the two gases. At high pressure, metal dusting initiated much earlier for Alloy 321 than at low pressure (Fig. 7.20). There is an incubation time beyond which the alloys exhibit weight loss and pitting attack. The incubation time is influenced by the alloy chemistry as well as the exposure conditions such as temperature, system pressure and carbon activity in the gas phase. Severe metal dusting attack starts after the incubation time. Table 7.6 shows the incubation time for Alloys 800, 321 and 253MA at different system pressures. Incubation times for other alloys are much longer than those of Alloys 800 and 321. We did not calculate the incubation times for other alloys since the exposure period was not long enough. However, the incubation time decreases with an increase in system pressure, assuming all other parameters are maintained the same. The incubation time for Alloy 800 is fairly short. Therefore, no significant difference of metal dusting attack was observed for Alloy 800 at different pressures. However, Alloy 321 had a long incubation time at atmospheric pressure. Increasing pressure decreased incubation time for both alloys; the effect was more dramatic for Alloy 321 than for Alloy 800. After subtraction of the incubation time, similar metal dusting rate is observed for different system pressures for both 800 and 321 (Fig. 7.21).

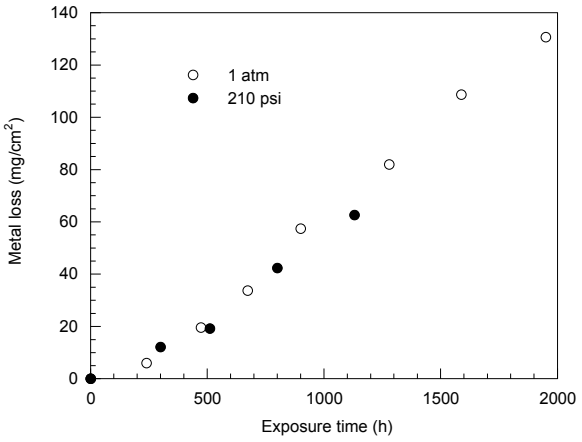

Figure 7.19. Weight loss of Alloy 800 and 321 in gas with similar carbon activity but different pressure.

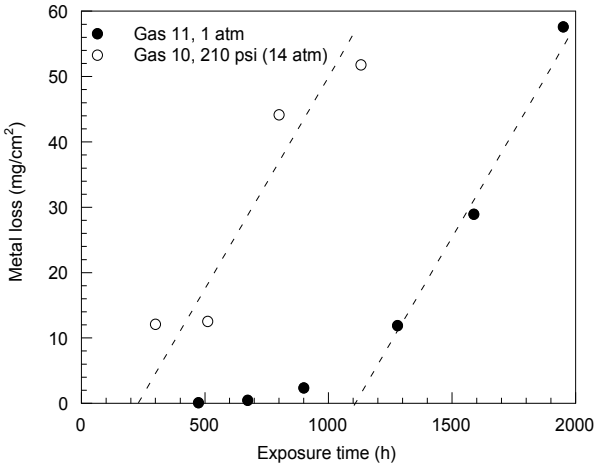

Figure 7.20. Weight loss data for Alloy 321 after exposure in Gases 10 and 11 at 593°C.

Pits were observed on Alloy 310 exposed in Gas 10 at 210 psi (14 atm) and 593°C. The major phase on the area without pits was Cr_2O_3 (Fig. 7.22). However, there was almost no Cr_2O_3 in the pit area. In Alloy 38815, metal dusting corrosion proceeded uniformly at 593°C and 210 psi (14 atm), and only spinel phase was observed in the Raman spectra (Fig. 7.23). At 1 atm, spinel was also the major phase on the surface of Alloy 38815. However, Fig. 7.24 shows that a disordered chromium oxide phase may protect this alloy from metal dusting corrosion. SiO_2 can form on the surface of Alloy 38815, but was not observed in the analysis by Raman scattering. At 1 atm, Si addition in Alloy 38815 was helpful in resistance to metal dusting, but at the

concentration level present in the alloy, it had no beneficial effect at high pressure. Additional effort is needed to establish the critical Si level needed to obtain a beneficial effect of this element at high pressure. Figure 7.25 shows the presence of Cr_2O_3 phase in the Raman spectra for Alloy 253MA tested at 1 atm and 593°C, but no Cr_2O_3 phase was found at 210 psi (14 atm). This difference may also affect the metal dusting corrosion rate.

Table 7.6. Incubation time for initiation of metal dusting in environments with similar carbon activity but with different system pressures.

	Incubation time (h)		
Alloy	41 atm	14 atm	1 atm
800		78	120
321	50	230	1100
253MA	150	800	>2830

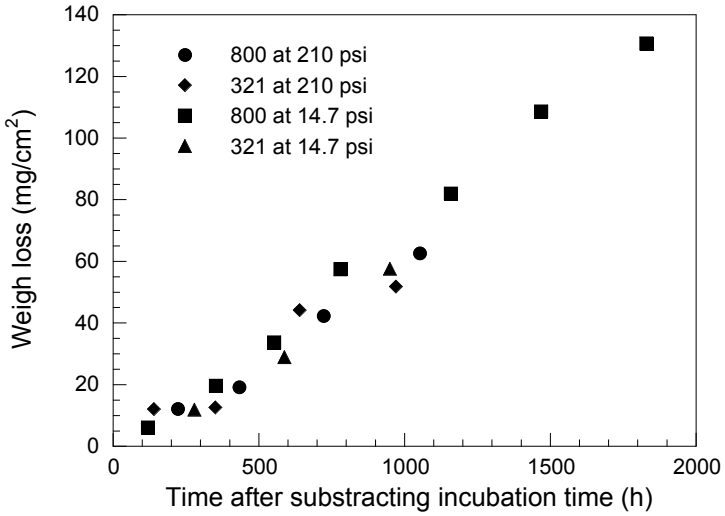

Figure 7.21. Weight loss data for Alloy 800 and 321 in gases with similar carbon activity but different pressure.

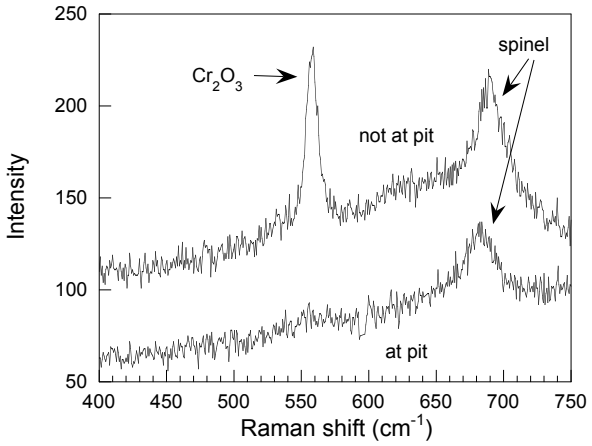

Figure 7.22. Raman spectra of Alloy 310 after 1100-h exposure in Gas 10 at 210 psi (14 atm) and 593°C.

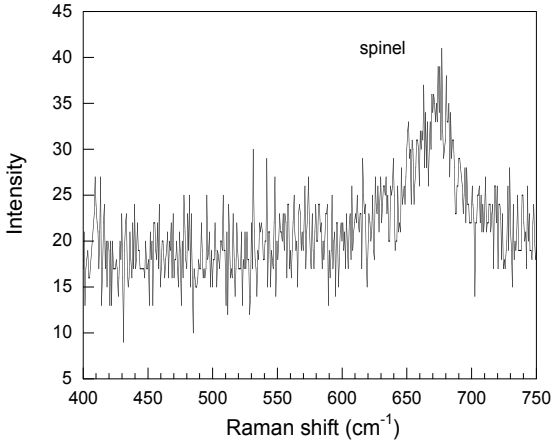

Figure 7.23. Raman spectra of Alloy 38815 after 1100-h exposure in Gas 10 at 210 psi (14 atm) and 593°C.

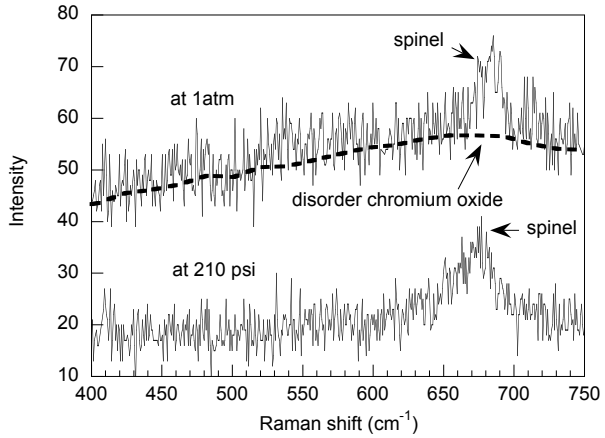

Figure 7.24. Raman spectra for Alloy 38815 after exposure in a carburizing atmosphere at different pressures.

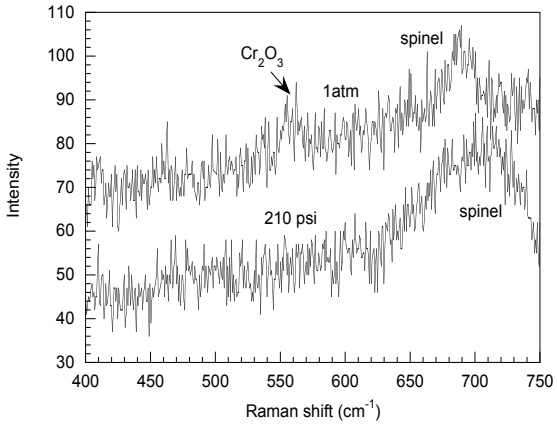

Figure 7.25. Raman spectra for Alloy 253MA after exposure in a carburizing atmosphere at different pressures.

The results presented thus far indicate that the system pressure can have a significant effect on the incubation time for the onset of metal dusting degradation of metallic alloys. If the exposure environment is such that an alloy can develop an oxide scale (due to high H_2O content in the gas), then the initiation of metal dusting will be influenced by the time necessary to break down and/or create defects in the oxide scale so that the deposited carbon can have a degrading effect on the underlying alloy. The pitting and metal dusting data show that creation of defects in the oxide occurs much earlier under high-pressure conditions, as evidenced by the shorter incubation time. Once the integrity and protective nature of the oxide is breached, albeit locally, the further propagation of attack seems to be independent of the system pressure as was seen from the weight loss data presented above for Alloys 800 and 321. Data for other alloys are being examined to evaluate the role of system pressure and alloy chemistry (translates to the integrity of oxide developed) on metal dusting degradation from the incubation and propagation standpoint.

7.6 Conclusion

Oxide scales that develop on alloys exposed to metal dusting environments consist of three phases: Cr_2O_3, disordered chromium oxide, and spinel. These oxides offer, at different degrees, protect the alloys against metal dusting attack. There exists a time called "incubation time" for the onset of metal dusting attack in metallic materials. The incubation time is strongly dependent on the integrity of the oxide that develops on the alloy surface. In turn, the oxide integrity, from the standpoint of chemical and mechanical stability, will be dependent on the alloy chemistry. The incubation time is also dependent on the process parameters such as temperature and system pressure. Experimental results showed that the incubation time decreases as the system pressure increases for a similar carbon activity and temperature in the exposure environment. The results also showed that the breakdown of the oxide scale occurs locally on the surface, as evidenced by the pitting type attack on the alloy surfaces. Once the integrity and protective nature of the oxide is breached, albeit locally, the further propagation of

attack seems to be independent of the system pressure as was seen from the weight loss data presented above for Alloys 800 and 321. Additional analysis is underway for several of the other alloys which will examine the relationship between the oxide integrity, incubation time, and metal dusting propagation.

8. WASTAGE RATES FOR NICKEL-BASE ALLOYS

8.1. Objectives

It has been reported that Ni-base alloys possess better resistance against metal dusting attack than the Fe-base alloys (Grabke et al. 1993, 1996, Maimer and Norton 1999). The reason has not been clear thus far. In Section 4 of this report, we indicated that the difference in the lattice mismatch in catalytic crystallization of carbon may be one reason. The misfit between the Ni and graphite lattice (3.6%) is much higher than that between Fe_3C and graphite (0.28%). The lattice of Fe_3C almost perfectly matches the lattice of graphite. This finding indicates that the movement of carbon atoms from the lattice of Fe_3C to graphite is easier than that from Ni to graphite. Therefore, the precipitation of carbon on surface of Ni has a higher energy barrier than that on the surface of Fe_3C. This difference leads to lower carbon precipitation rate, smaller crystallite size, and lower metal dusting rate. The observed crystallite size of coke on nickel is smaller than that on iron (Table 3.1). This difference suggests that Fe_3C is better than Ni in serving as a template for the catalytic crystallization of carbon, and may explain why the metal dusting rate of Fe and Fe-base alloys is higher than that of Ni and Ni-base alloys. The other factor that can affect metal dusting rate is the chemical and mechanical integrity of the oxide layer that develops on the surface of alloys. In this Section, we present results from a study on the effect of alloy chemistry and phase composition of oxides on the surface of Ni-base alloys on the metal dusting rate. We also examine the information on metal dusting rate for several Ni-base alloys in various gas environments to establish the best candidate alloys for resistance to metal dusting corrosion.

8.2. Experimental

Ni-base alloys were tested in gas mixtures 4, 10, 11, 14, 15, and 17 (Table 1.1) at 593°C for periods in the range of 100-5300 h. System pressures in the tests were 1 atm, 210 psi (14 atm), 400 psi (27 atm), and 600 psi (41 atm). Carbon deposits were collected from several of these tests and were analyzed by Raman spectroscopy. The exposed specimens from were examined by SEM and Raman spectroscopy.

8.3. Weight Loss and Surface Analysis of Alloys Exposed to Carburizing Atmosphere

No metal dusting attack was observed for Ni-base alloys in the relatively short exposure time of 246-300 h at 1 atm (Tables 8.1 and 8.2). However, pits were observed on Alloys 601, 690, 617, and 214 when exposed in Gas 10 at 210 psi (14 atm) for 100 h (Table 8.3). Similar results were obtained when specimens were tested at 600 psi (41 atm) (Table 8.4). Figure 8.1 shows the surface of several alloys after exposure in Gas 10 at 1 atm and at high pressure.

Metal dusting attack was observed on all the Ni-base alloys when tested for 4100 h in Gas 10 at 593°C and 210 psi (14 atm) (Figs. 8.2 and 8.3). However, the weight loss rates for Alloys 693 and 602CA were very low. Both alloys contain Al and have high Cr content and low amount of Fe. The weight loss rate for Alloy 45TM was the highest among the Ni-base alloys used in the study, although the Cr content in this alloy is fairly high. The iron content in Alloy 45TM is also the highest among these alloys. The weight loss rate of Alloy 601 was also high.

Table 8.1. Weight loss data for alloys after 300-h exposure (Run 48) at 593°C and 1 atm in Gas 4.

Alloys	Mass loss (mg/cm^2h)	Visual examination
600	0	Clean surface
601	0	Clean surface
690	0	Clean surface

Table 8.2. Weight loss data for alloys after 246-h exposure (Run 60) at 593°C and 1 atm in Gas 10.

Alloys	Mass loss (mg/cm^2h)	Visual examination
601	0	Clean surface
690	0	Clean surface
617	0	Clean surface
602CA	0	Clean surface
214	0	Clean surface
45TM	0	Clean surface
HR160	0	Clean surface

Table 8.3. Weight loss data for alloys after 100-h exposure (Run 50) at 593°C and 210 psi (14 atm) in Gas 10.

Alloys	Mass loss (mg/cm^2h)	Visual examination
601	0	Pits
690	0	Pits
617	0	Pits
602CA	0	Clean surface
214	0	Pits
45TM	0	Clean surface
HR160	0	Clean surface

Table 8.4. Weight loss data for alloys after 113-h exposure (Run 51) at 593°C and 600 psi (41 atm) in Gas 4.

Alloys	Mass loss (mg/cm^2h)	Visual examination
601	0	Pits
690	0	Pits
617	0	Pits
602CA	0	Clean surface
214	0	Pits
45TM	0	Clean surface
HR160	0	Clean surface

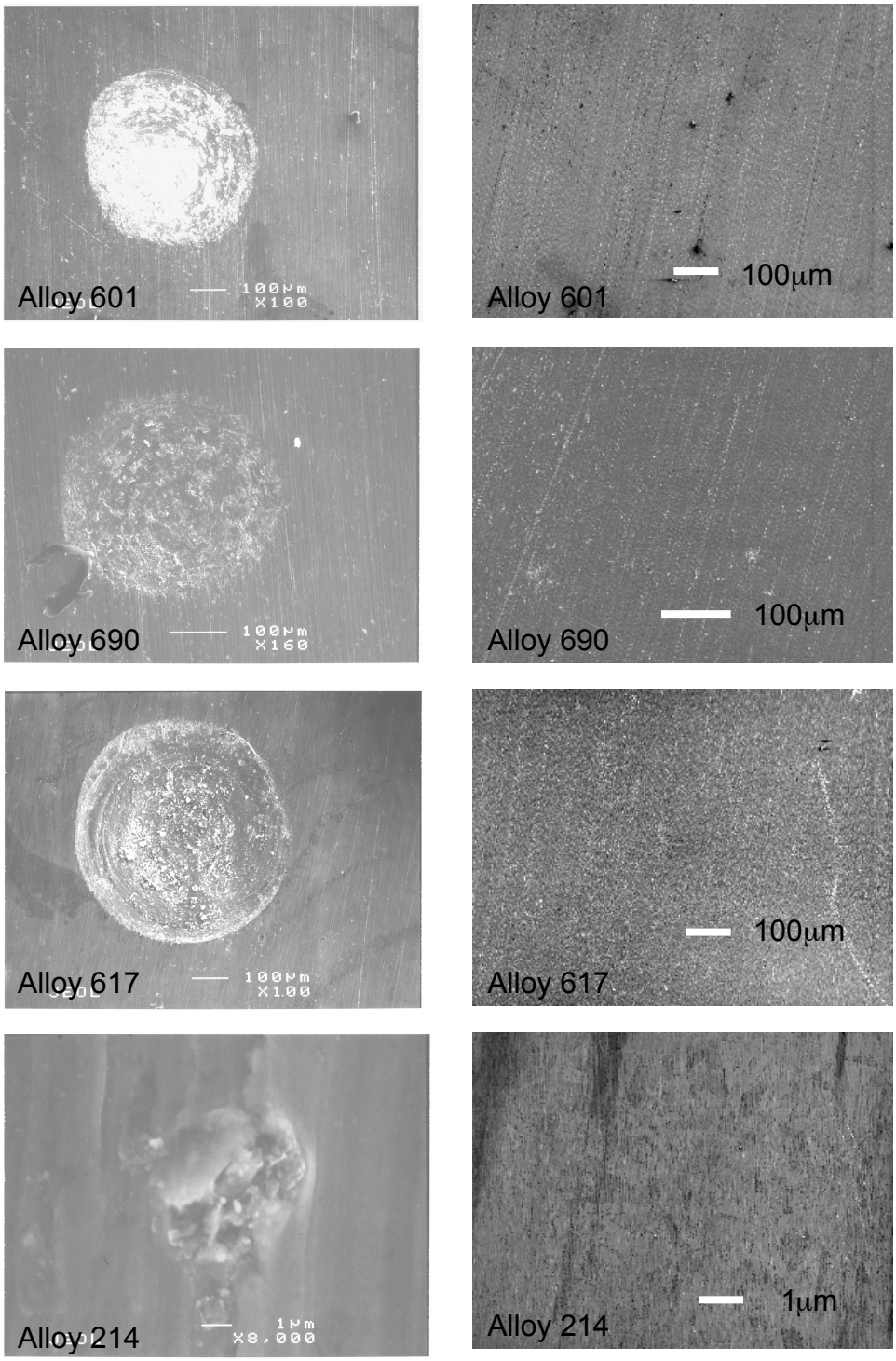

Figure 8.1. SEM micrographs of surfaces of several Ni-base alloys after exposure to a metal dusting environment. Left: exposed at 14 atm and 593°C for 160 h, metal dusting pits were observed. Right: exposed at 1 atm and 593°C for 240 h, surfaces of alloys are smooth, and no metal dusting pits appear.

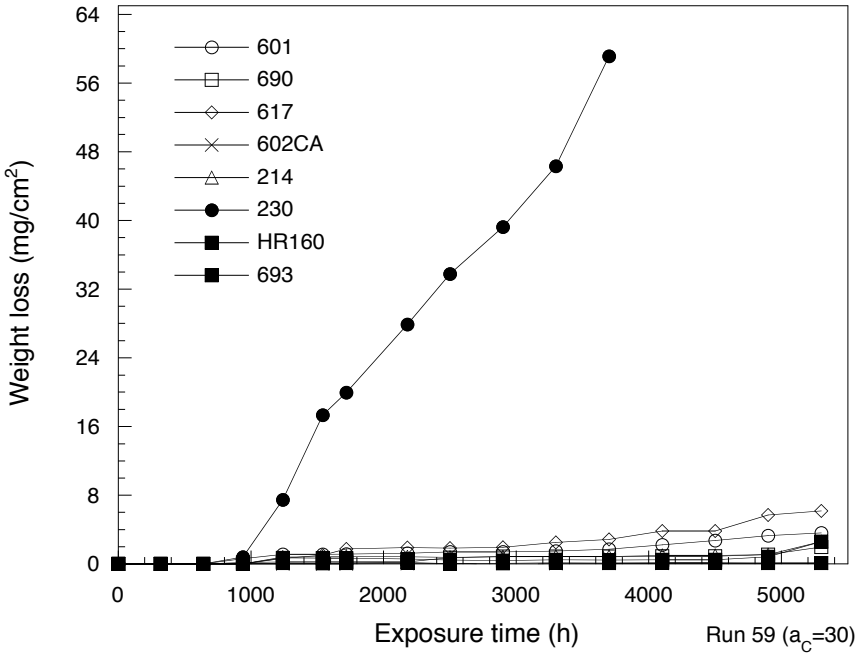

Figure 8.2. Weight loss data for several Ni-base alloys after exposure in Gas 10 at 210 psi (14 atm) and 593°C.

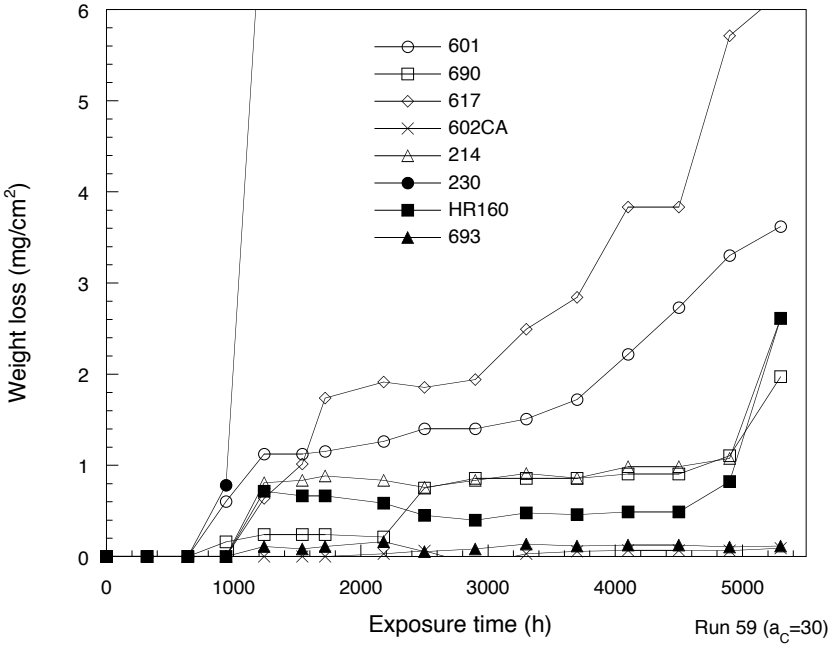

Figure 8.3. Magnified view of weight loss data shown in Fig. 8.2.

The iron content in Alloy 601 is the second highest among these alloys. The results indicate that addition of iron to the Ni-base alloys substantially decreases incubation time for the onset of metal dusting. When Fe content in the alloy is >10%, the alloy is readily attacked, as evidenced by numerous pits on the exposed surfaces of the alloy specimens. The weight loss rate for cobalt-containing Alloy 617 is the second highest among these alloys. Mo addition in this alloy did not improve its resistance to metal dusting corrosion. The other cobalt-containing Alloy HR160 also exhibited metal dusting degradation, although it contained 28% Cr. Therefore, Co addition in alloys is also not beneficial in resisting metal dusting. The Cr content in Alloy 214 is the lowest among these alloys, and its weight loss rate is also high, although it contains aluminum. High Cr content in alloys seems essential but not entirely sufficient for preventing metal dusting corrosion in Ni-base alloys.

8.4 Phase Composition of Scales on Ni-base Alloys in Gas 10 at 14 atm

In the tests with Gas 10 at 210 psi (14 atm) and 593°C, Raman spectra showed that the intensity of the Cr_2O_3 band at ≈560 cm^{-1} was low for both Alloy 214 and 45TM and the relative intensity of spinel is high in both the alloys. As was discussed earlier in this report, spinel phase in the scale is not as good as the Cr_2O_3 scale in preventing alloys from metal dusting corrosion. This low chromium content is probably the cause for metal dusting in these two alloys. The low Cr_2O_3 content on the surface of Alloy 214 may be due to the low Cr content in the alloy. On the contrary, the Cr content in 45TM is relatively high but the Fe content is also high. The presence of high Fe content may stabilize the Fe-containing spinel phase rather than Cr_2O_3, thereby subjecting the alloy to metal dusting. $NiCr_2O_4$ spinel is not thermodynamically stable in the reducing environment used in our study and, therefore, could not form in Gas 10 at 593°C (Fig. 8.4). The results suggest that an alloy with a high Cr content (with or without Al) and low Fe content may stabilize Cr_2O_3 and/or a spinel phase with high Cr content. This stabilization would prolong the incubation period for the onset of metal dusting and subsequent propagation of the process, leading to metal wastage.

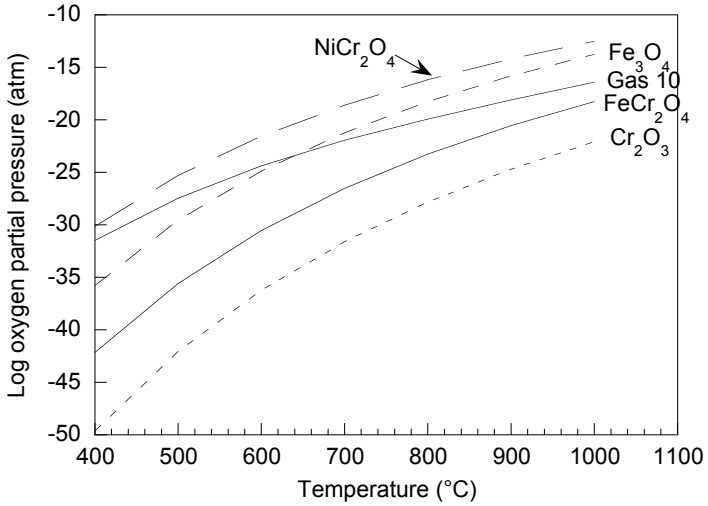

Figure 8.4. Thermal stability of spinel and Cr_2O_3 phases.

8.5 Change in Phase Composition of Scale on Ni-base Alloys in Gas 10 at 14 atm

In tests with Gas 10 at 210 psi (14 atm) and 593°C, phase composition of oxide scales that developed on the surface of alloys changed with exposure time. Figures 8.5 to 8.12 show the intensity differences of Raman bands for Cr_2O_3 and spinel phases in oxide scale on the surfaces of several alloys. When the alloys were exposed for only 100 h, Cr_2O_3 was the major phase in the oxide scales that developed on the surface of alloys. However, after 2900 h exposure, the intensity of the spinel band in Raman spectra increased significantly. On Alloy 214, spinel became the major phase after exposure for 2900 h, whereas Cr_2O_3 was the major phase in the oxide scale when the alloy had been exposed for 100 h (Fig. 8.10).

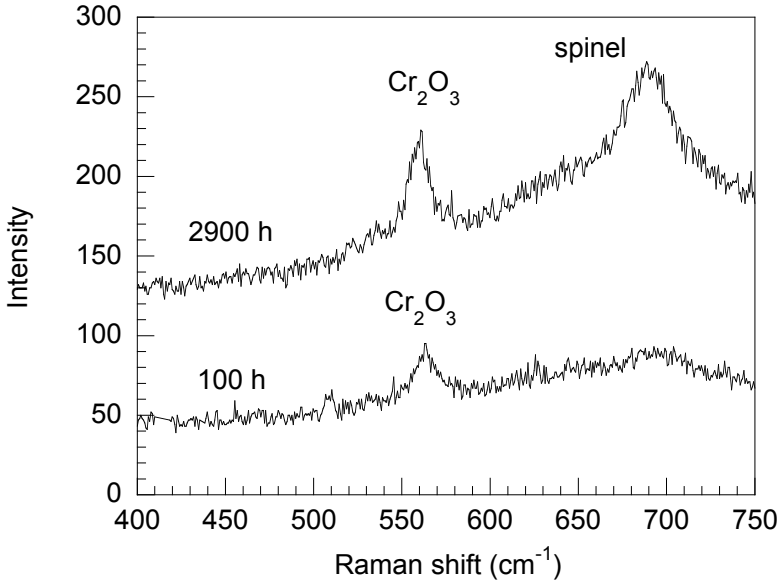

Figure 8.5. Raman spectra of Alloy 601 after 100-h and 2900-h exposures in Gas 10 at 593°C and 210 psi (14 atm).

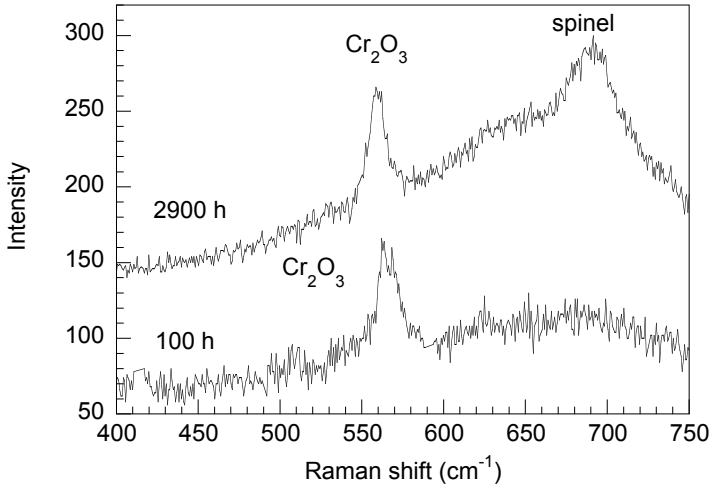

Figure 8.6. Raman spectra of Alloy 690 after 100-h and 2900-h exposures in Gas 10 at 593°C and 210 psi (14 atm).

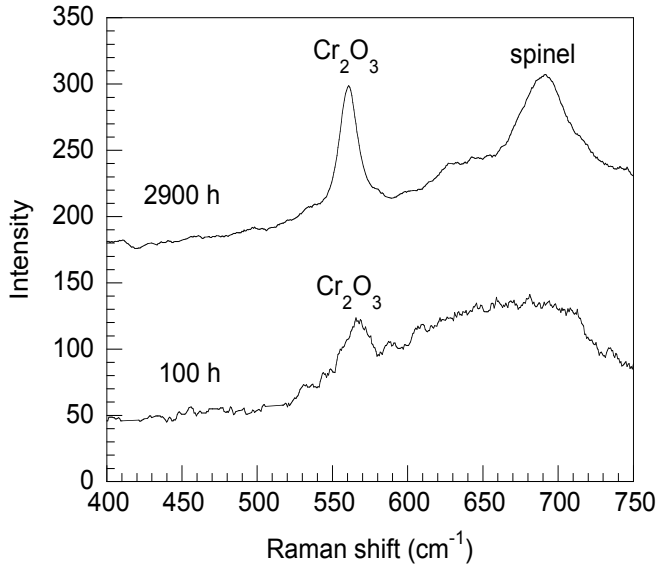

Figure 8.7. Raman spectra of Alloy 617 after 100-h and 2900-h exposures in Gas 10 at 593°C and 210 psi (14 atm).

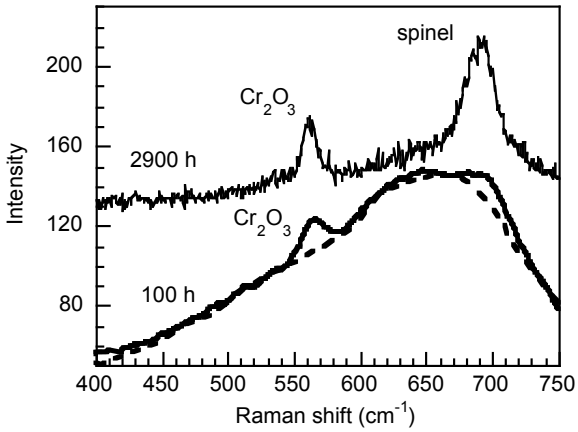

Figure 8.8. Raman spectra of Alloy 45TM after 100-h and 2900-h exposures in Gas 10 at 593°C and 210 psi (14 atm).

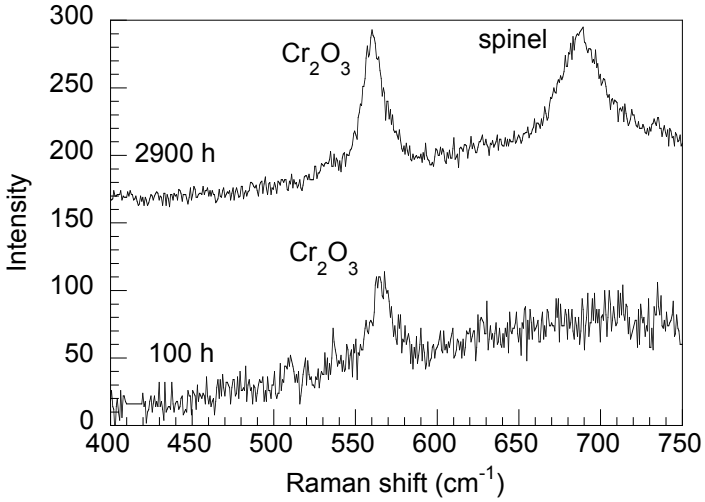

Figure 8.9. Raman spectra of Alloy 602CA after 100-h and 2900-h exposures in Gas 10 at 593°C and 210 psi (14 atm).

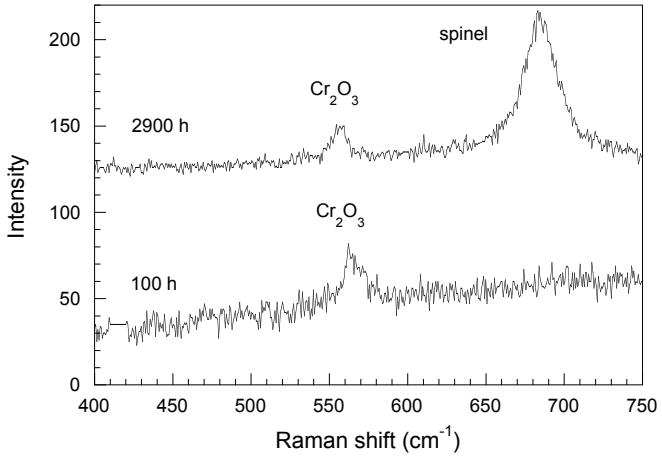

Figure 8.10. Raman spectra of Alloy 214 after 100-h and 2900-h exposures in Gas 10 at 593°C and 210 psi (14 atm).

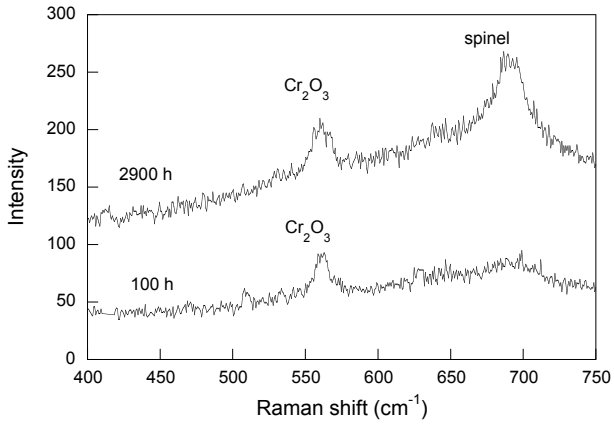

Figure 8.11. Raman spectra of Alloy HR160 after 100-h and 2900-h exposures in Gas 10 at 593°C and 210 psi (14 atm).

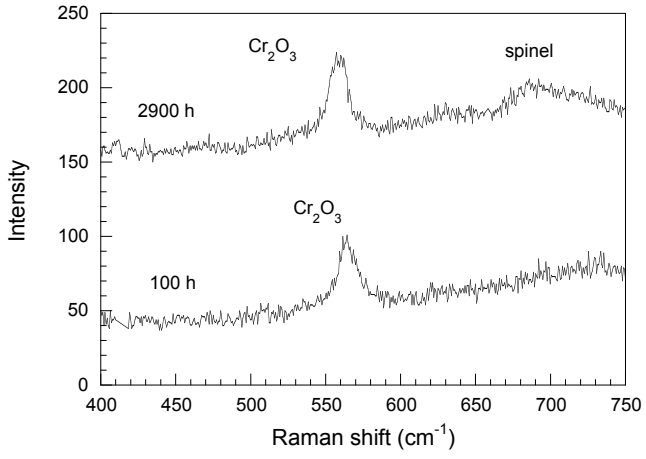

Figure 8.12. Raman spectra of Alloy 693 after 100-h and 2900-h exposures in Gas 10 at 593°C and 210 psi (14 atm).

The increasing amount of spinel phase in oxide scales over longer exposure time can be attributed to the outward diffusion of Fe from the alloy substrate. At early stages, Cr-rich oxide forms on the surface of alloys. However, as the outward transported Fe gets incorporated into the scale, spinel phase becomes dominant, as observed in the Raman spectra. The diffusion rate of Fe and its incorporation in the scale to form the spinel phase would have a pronounced effect on the incubation time for the onset of metal dusting in the alloy. As the transported Fe gets incorporated into the spinel phase, the protective capacity of the spinel is reduced, since the inward migrating carbon can easily reduce the high-iron-containing spinel (as discussed earlier in this report). The Raman analysis showed that the spinel band intensity was the lowest for Alloy 693 after 2900 h exposure in Gas 10 at 210 psi (14 atm) and 593°C. This finding suggests that the incubation time for the onset of metal dusting for this alloy will be significantly greater than most of the others studied in this program.

8.6 Metal Dusting of Ni-base Alloys Exposed to Gas 11 at 1 atm

Figure 8.13 shows the weight loss data for several Ni-base alloys that were exposed in Gas 11 for 1950 h at 593°C and 1 atm. Only Alloys 601 and 214 exhibited pits on the surfaces and correspondingly showed weight loss. None of the other alloys showed any weight loss, and the specimen surfaces were without pits after ultrasonic cleaning. The weight loss rates for Alloy 214 (with low Cr content of 15.9% but with 3.7% Al) and Alloy 601 (with 21.9% Cr and no Al) were similar. The Fe contents in Alloys 214 and 601 were 2.5 and 14.5%, respectively. In contrast, Alloy 45TM (which contained 27.4% Cr and 26.7% Fe) did not exhibit weight loss, and the specimen surface did not develop any pit after exposure in Gas 11.

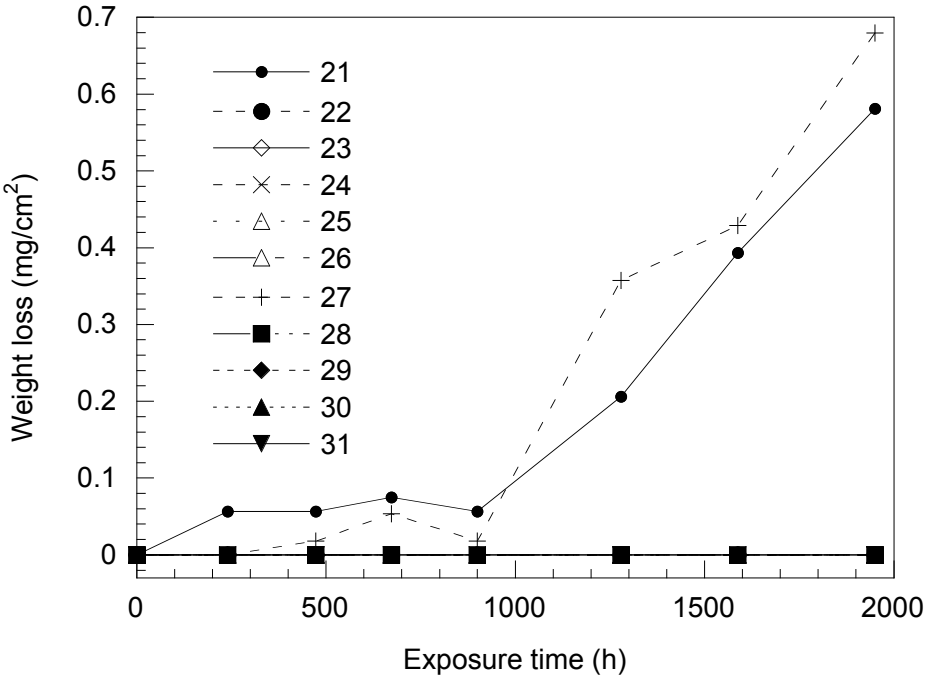

Figure 8.13. Weight loss of Ni-base alloys aferr exposure in Gas 11 at 593°C and 1 atm.

The other alloys did not lose weight, and surfaces were clean. The weight loss rate of Alloy 214 was the highest among these alloys, primarily because of its low Cr content. Although Alloy 214 contains 3.7% Al, metal dusting was not prevented by aluminum in this alloy. Therefore, it is deemed essential for an alloy to contain both Al and a high content of Cr (>20%) to minimize metal dusting corrosion. At 1 atm, Alloy 45TM was not attacked by metal dusting in Gas 11 at 593°C for 1950 h, but its weight loss rate was very high at 210 psi (14 atm) in Gas 10. High Cr content in this alloy protected it at 1 atm (longer incubation time), but did not protect it at high pressure.

8.7 Phase Composition of Scale on Ni-base alloys in Gas 11 at 1 atm

Figure 8.14 shows the Raman spectra for several Ni-base alloys that were exposed for 1950 h in Gas 11 at 1 atm. In contrast with the alloys exposed in Gas 10 at 210 psi (14 atm), the Raman band intensity of spinel phase for these specimens is very low. Cr_2O_3 is the primary

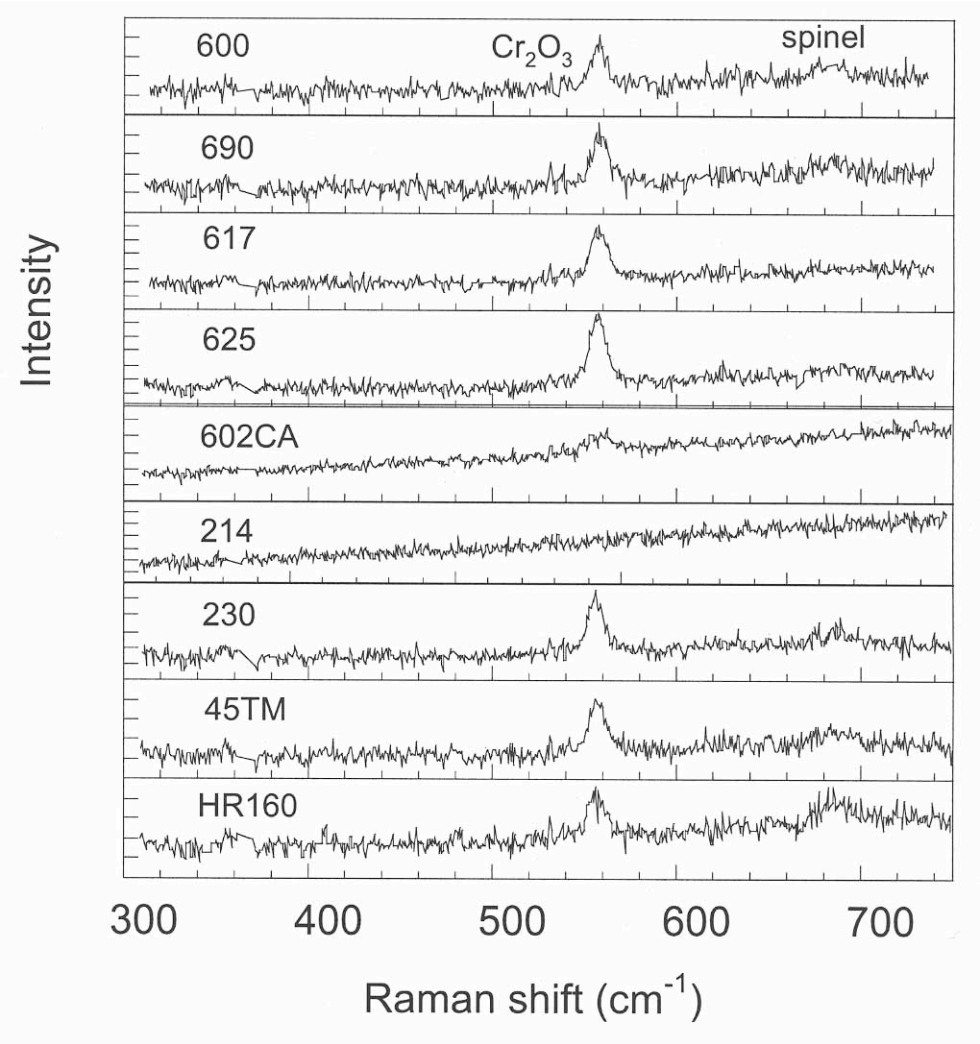

Figure 8.14. Raman spectra for alloys exposed for 1950 h in Gas 11 at 1 atm and 593°C.

phase on the surface of these alloys. This may be one reason that these alloys were less attacked by metal dusting in Gas 11 at 1 atm. Figure 8.15 shows that the Cr_2O_3 band is much stronger than the spinel band for Alloy 45TM exposed in Gas 11 at 1 atm. However, the spinel band is much stronger than that of Cr_2O_3 if this alloy is exposed in Gas 10 at 210 psi (14 atm). Alloy 45TM lost weight heavily when it was exposed in Gas 10 at 210 psi (14 atm), but it was not attacked when exposed in Gas 11 at 1 atm, although the carbon activity was similar in both tests. The observed performance difference of the alloy in the two tests can be attributed to the difference in the phase composition of oxide scales that develop on the alloy surface. The cobalt-containing alloy 617 also performed similarly to Alloy 45TM. Almost no spinel phase was observed by Raman spectroscopy on the surface of Alloy 617 exposed to Gas 11 at 1 atm and 593°C (Fig. 8.16), and the alloy was not attacked by metal dusting. However, pits were observed on the surface of this alloy, and the intensity of the spinel band in the Raman spectra was stronger than that of the Cr_2O_3 band when tested in Gas 10 at 210 psi (14 atm) (Fig. 8.16).

When Al-containing alloys 214 (3.7% Al) and 602CA (2.3% Al) were exposed to Gas 11 at 1 atm and 593°C, Alloy 214 exhibited strong fluorescence from Al_2O_3 in Raman spectroscopy (Fig. 8.17). The γ-phase Al_2O_3 (which will be stable alumina at low temperature) is almost featureless, with a broad fluorescence background. The fluorescence masks the Raman lines of Cr_2O_3 and $(Fe,Cr)_3O_4$ spinel. However, Cr_2O_3 and $(Fe,Cr)_3O_4$ spinel phases can be observed from the alloy exposed to Gas 10 at 210 psi (14 atm) and 593°C. Raman spectra for Alloy 602CA (after exposure in Gas 11 at 1 atm) primarily showed Cr_2O_3 phase, and spinel phase was virtually absent (Fig. 8.18). The difference in behavior of these two alloys can be attributed to the difference in Cr content between the two alloys (25% in 602CA versus 15.9% in 214). The beneficial effect of higher Cr content is also evident in the tests conducted in Gas 10 at 210 psi (14 atm). The spectra in Figs. 8.17 and 8.18 show that the spinel phase dominates in Alloy 214, whereas Cr_2O_3 phase is dominant in 602CA, even though the exposure condition was the same for both the alloys at 210 psi (14 atm).

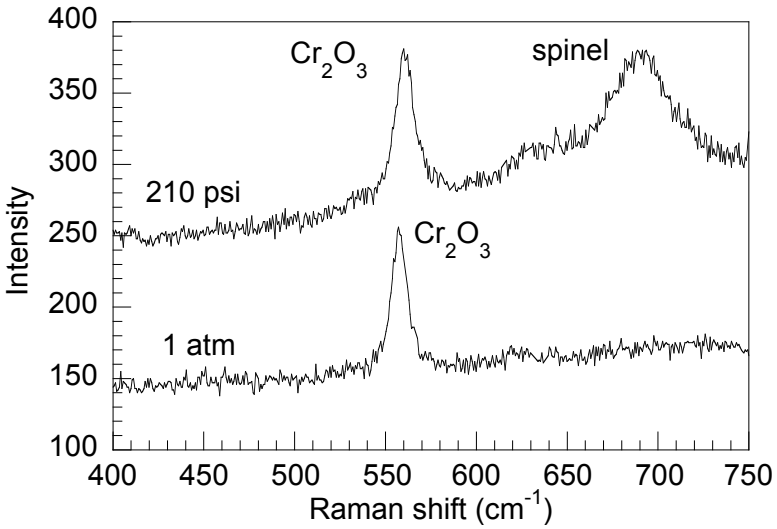

Figure 8.15. Raman spectra of Alloy 45TM exposed at 593°C in Gas 10 at 210 psi (14 atm) and Gas 11 at 1 atm.

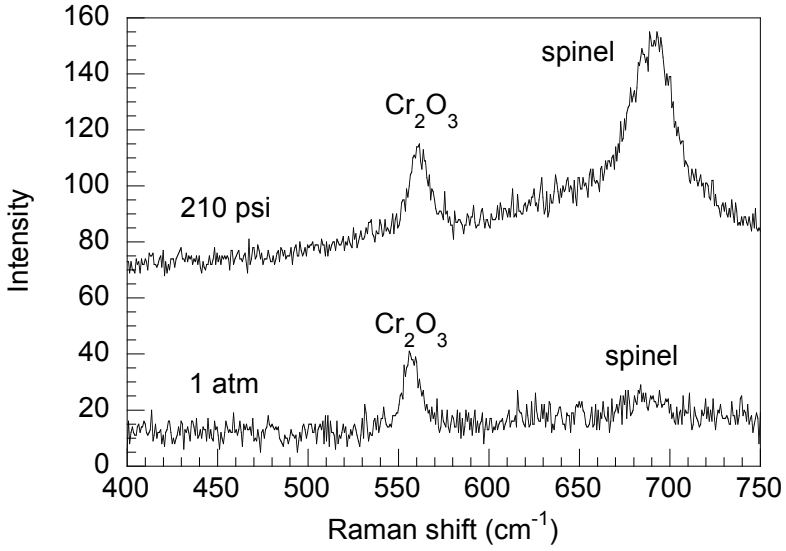

Figure 8.16. Raman spectra of Alloy 617 exposed at 593°C in Gas 10 at 210 psi (14 atm) and Gas 11 at 1 atm.

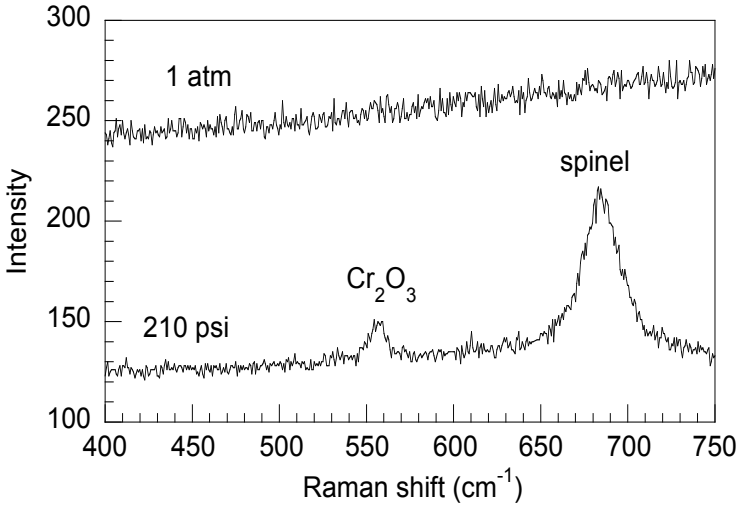

Figure 8.17. Raman spectra of Alloy 214 exposed at 593°C in Gas 10 at 210 psi (14 atm) and Gas 11 at 1 atm.

8.8 Metal Dusting of Ni-base Alloys Exposed to Gas 14 at 1 atm

When Ni-base alloy specimens were exposed in Gas 14 ($a_C \approx 9$) at 593°C and 1 atm for 5300 h, pits were observed on the surface of Alloys 214 and 600. These two alloys exhibited an incubation time ≈1100 h. The weight loss for both these alloys increased with continued exposure (Fig. 8.19). The Cr content of both these alloys was 15.4-15.9 wt%, which is low to offer protection against metal dusting as we discussed earlier in this report. The other alloys did not show any weight loss or much pitting attack.

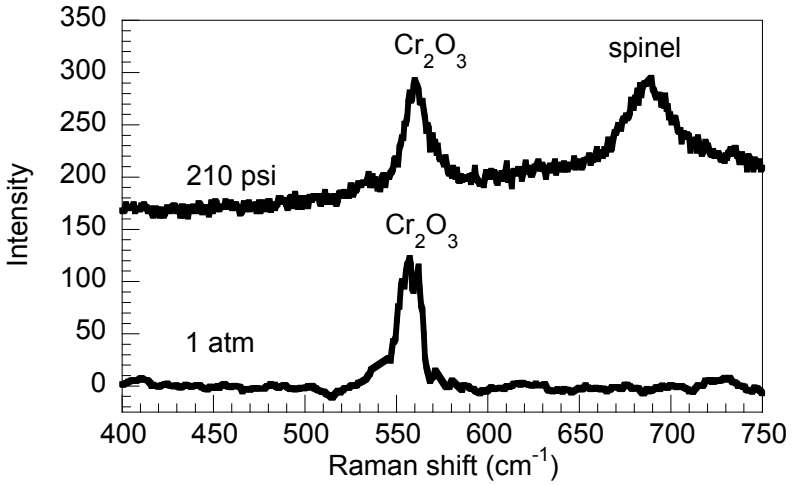

Figure 8.18. Raman spectra of Alloy 602CA exposed at 593°C in Gas 10 at 210 psi (14 atm) and Gas 11 at 1 atm.

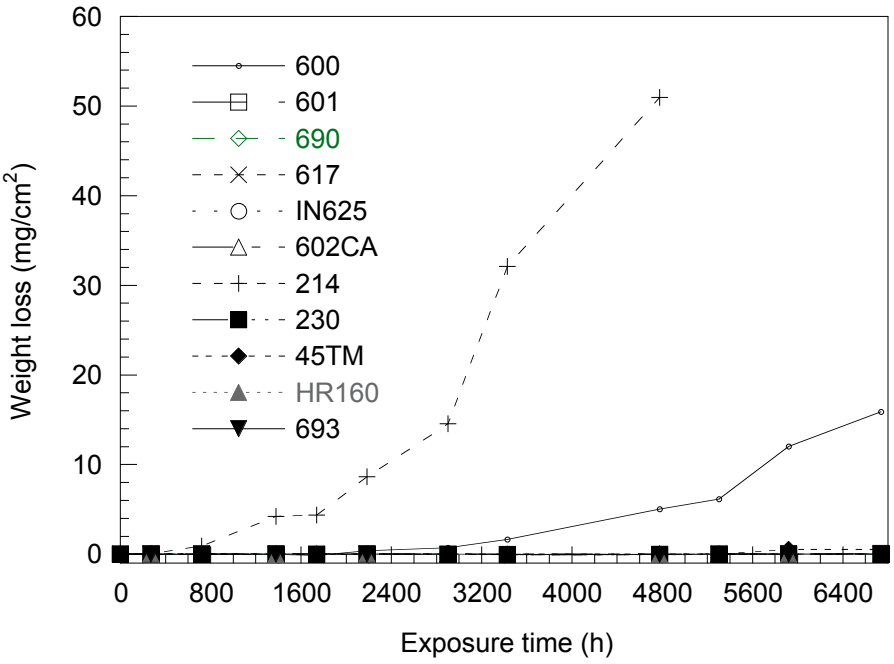

Figure 8.19. Weight loss of Ni-base alloys in Gas 14 at 593°C and 1 atm.

8.9 Metal Dusting of Ni-base Alloys Exposed to Gas 15 at 1 atm

Alloys 214 and 600 were the only two alloys that had been attacked by metal dusting corrosion in Gas 15 at 593°C and 1 atm (Fig. 8.20). Gas 15 contained less H_2 and more CO than did Gas 14. Carbon activity of Gas 15 was ≈6.5 at 593°C and 1 atm and is a little lower than that of Gas 14. However, metal loss rates for Alloys 214 and 600 were significantly less in Gas 15 than those observed in Gas 14. This enormous difference cannot be attributed to a small

decrease in carbon activity values that were calculated based on Reaction 1. It is possible that the relative ratio of H_2 to CO in the gas mixture (0.9 for Gas 14 and 0.3 for Gas 15) may have an influence at the macroscopic level on the catalytic crystallization of carbon. Further experiments are needed to clarify this point.

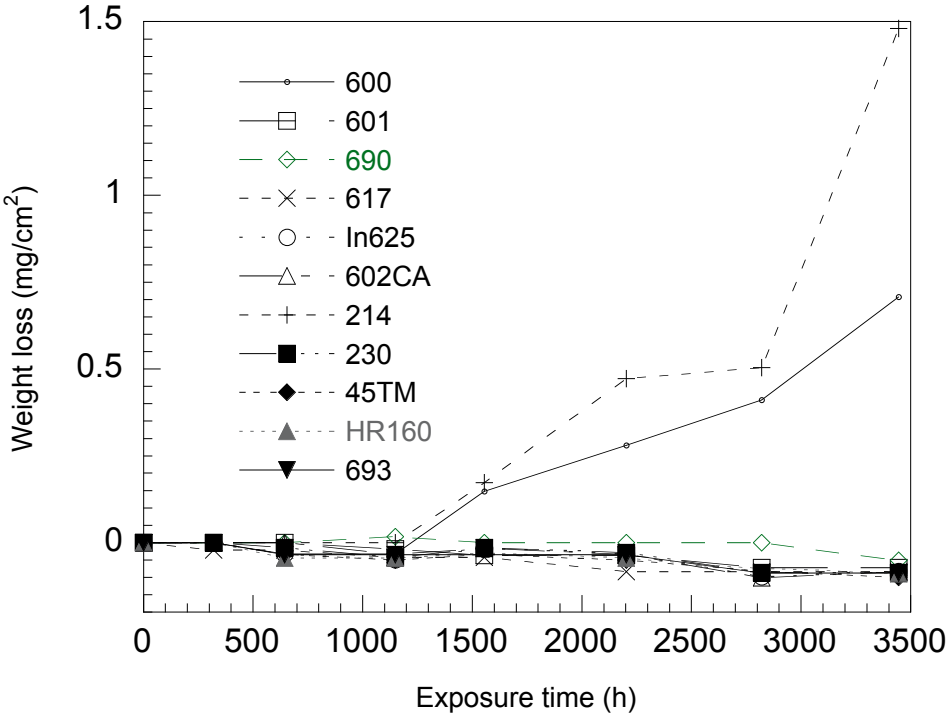

Figure 8.20. Weight loss of Ni-base alloys in Gas 15 at 593°C and 1 atm.

8.10 Metal Dusting of Ni-base Alloys Exposed to Gas 17 at 1 atm

When alloys were exposed in high carbon activity Gas 17 (a_C=148) at 593°C and 1 atm (Fig. 8.21), Alloy 45TM lost weight as fast as observed for Gas 10 (a_C=38) at 593°C and 210 psi. The weight loss rate for Alloy 600 exposed in Gas 17 at 593°C and 1 atm was higher than that of Alloy 600 exposed in gases with low carbon activities such as Gas 11 (a_C=31), Gas 14 (a_C=9), and Gas 15 (a_C=6.5). Alloy 602CA was the best alloy to resist metal dusting in Gas 10 at 593°C and 210 psi (14 atm). However, this alloy also was attacked by metal dusting when it was exposed in high carbon activity Gas 17 (a_C=148) at 593°C and 1 atm. Its weight loss rate was even higher than that of Alloy 214, although the Cr content in Alloy 602CA (25.1%) is much higher than that in Alloy 214 (15.9%). This may be due to the higher iron content in 602CA (9.3%) than that in Alloy 214 (2.5%). Alloys 690, IN625, 230, HR160, and 693 were not attacked by metal dusting in Gas 17 at 593°C and 1 atm for 4700 h of exposure.

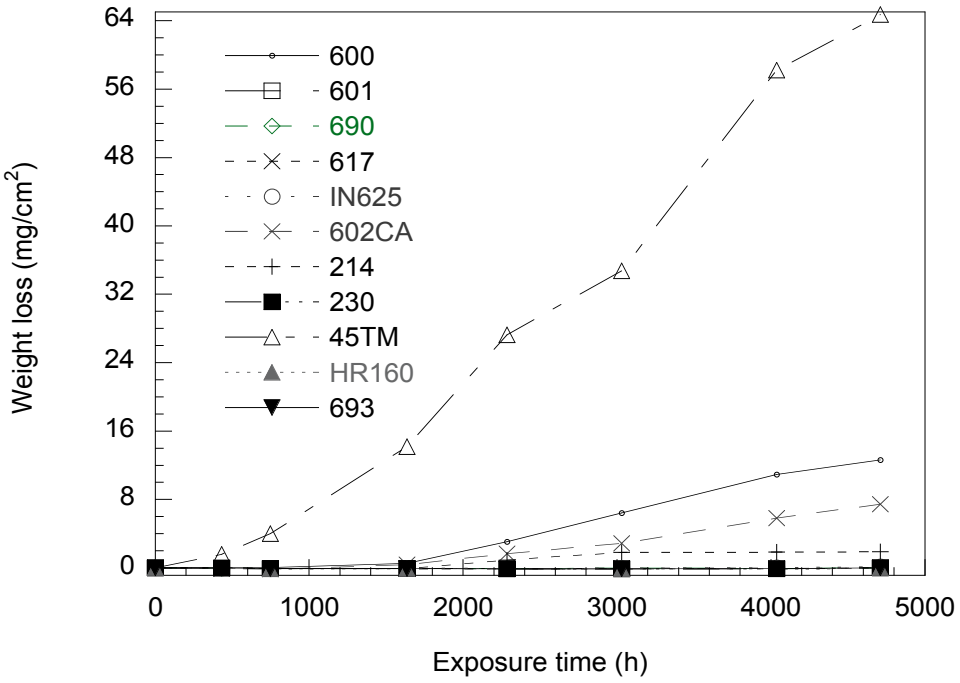

Figure 8.21a. Weight loss of Ni-base alloys in Gas 17 at 593°C and 1 atm.

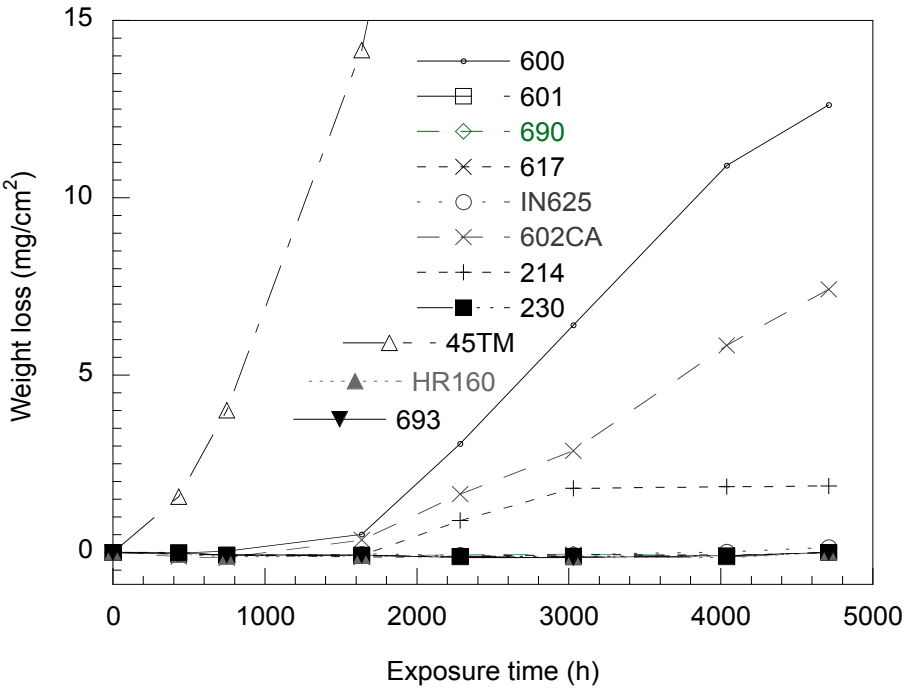

Figure 8.21b. Magnified view of data in Fig. 8.21a.

8.11 Difference in Performance Between Fe- and Ni-base Alloys

Based on our study, MA956, APMT, and 4C54 are the best three Fe-base alloys to resist metal dusting. Two of the three alloys contain Al (4.5% in MA956 and 4.9% in APMT), and this element seems to be beneficial from the standpoint of incubation time for metal dusting. The third alloy 4C54 contains 26.7% Cr, the highest among the alloys investigated in the present study.

In general, the performance of Ni-base alloys was better than that of Fe-base alloys in metal dusting atmospheres. Among the Ni-base alloys, the performance of Alloy 693 was the best since the Cr and Al contents of this alloy are very high. Alloy 602CA was good in most tests, but it was attacked in high-carbon-activity Gas 17.

Figures 8.22 and 8.23 show the differences in Raman spectra for two pairs of alloys: Alloy 253MA and 601, and Alloy 310 and 602CA. These alloys were exposed for 1000 h to Gas 10 at 593°C and 210 psi (14 atm). The Cr content in Alloy 253MA (20.9%) and 601 (21.9%) is similar. However, the Fe-base alloy 253MA has a much stronger spinel peak than that of the Ni-base alloy 601 (Fig. 8.22). Pits were observed on Alloy 253MA, but not on Alloy 601 when exposed under the same experimental conditions. The Cr content in Alloy 310 (25.5%) and 602CA (25.1%) is also similar. Figure 8.23 shows the strong spinel peak for the Fe-base alloy 310, but almost no such peak for the Ni-base alloy 602CA. Pits were again observed only on Alloy 310, but not on Alloy 602CA. Less spinel in the oxide scale of Ni-base alloys may be a possible reason that the performance of the Ni-base alloys is superior to that of the Fe-base alloys.

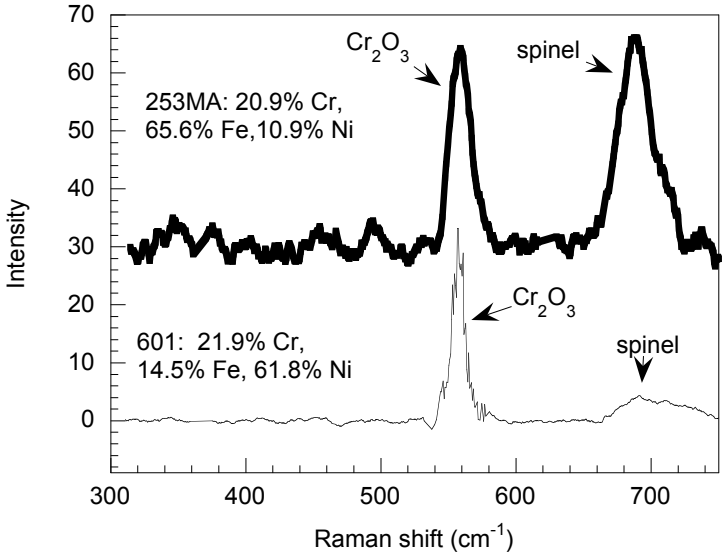

Figure 8.22. Raman spectra of Alloys 253MA and 601 exposed for 1000 h to Gas 10 at 593°C and 210 psi (14 atm).

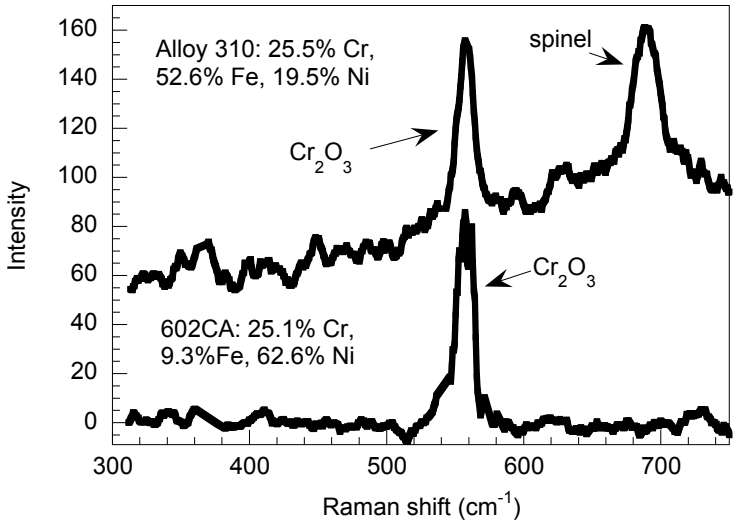

Figure 8.23. Raman spectra of Alloys 310 and 602CA exposed for 1000 h to Gas 10 at 593°C and 210 psi (14 atm).

A similar comparison can be made for several Fe- and Ni-base alloys that were exposed in Gas 13 at 593°C and 1 atm. Figures 8.24-8.26 show Raman spectra for three pairs of alloys that were exposed for 300 h in Gas 13 at 593°C and 1 atm. The Cr content in each pair of alloys is similar. However, the relative ratios of intensity of the Cr_2O_3 band over the spinel band in the Raman spectra for the Ni-base alloys are always higher than those for the Fe-base alloys. Pits were observed on all three Fe-base alloys, but not on any of the three Ni-base alloys. Therefore, Fe-base alloys can form more spinel phase in the oxide scale. This spinel phase is responsible for the breakdown of the protective capacity of the scale. This effect leads to metal dusting attack much earlier in Fe-base alloys than in Ni-base alloys.

8.12 Conclusion

Phase composition on the surface of Ni-base alloys is one of the deterministic factors for the alloys to resist metal dusting degradation in carburizing atmospheres. Cr_2O_3 is a better phase than spinel to resist metal dusting. Increasing Cr content in alloys suppressed and/or delayed the formation of spinel phase on the alloy surface and, thereby, increased the ability of alloys to resist metal dusting. However, increasing the iron content of the Ni-base alloys favors the formation of spinel phase, which is predominantly attacked by carbon and accelerates metal wastage. Aluminum addition is beneficial for resisting metal dusting in most cases. Especially, in high-pressure carburizing gas environment, aluminum addition in the alloy successfully suppressed metal dusting. Based on our study, Alloy 693 was judged superior to resist metal dusting since it contains the highest Cr and Al content among the alloys tested. Cobalt addition does not increase the ability of alloy to resist metal dusting.

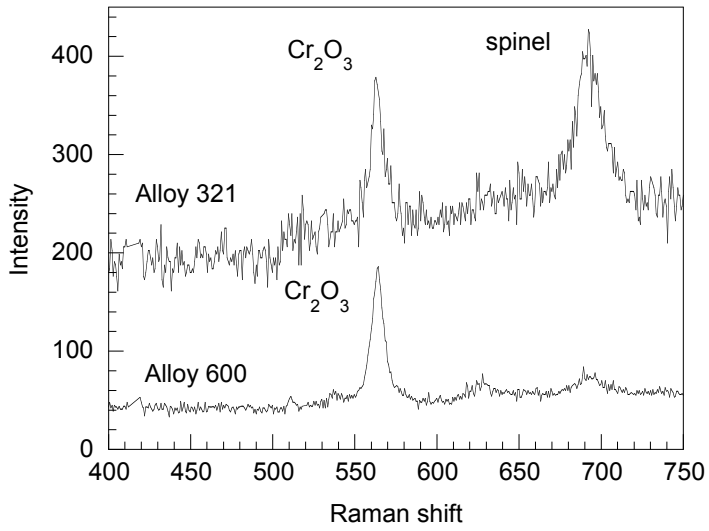

Figure 8.24. Raman spectra for Alloys 321 and 600 exposed for 300 h in Gas 13 at 593°C and 1 atm.

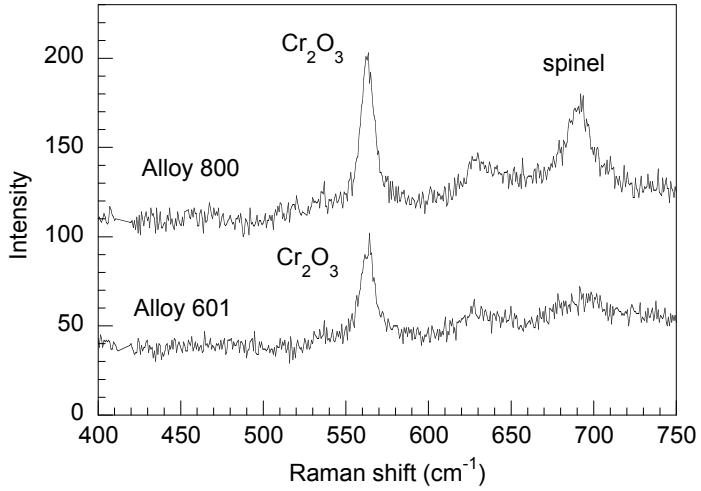

Figure 8.25. Raman spectra for Alloys 800 and 601 exposed for 300 h in Gas 13 at 593°C and 1 atm.

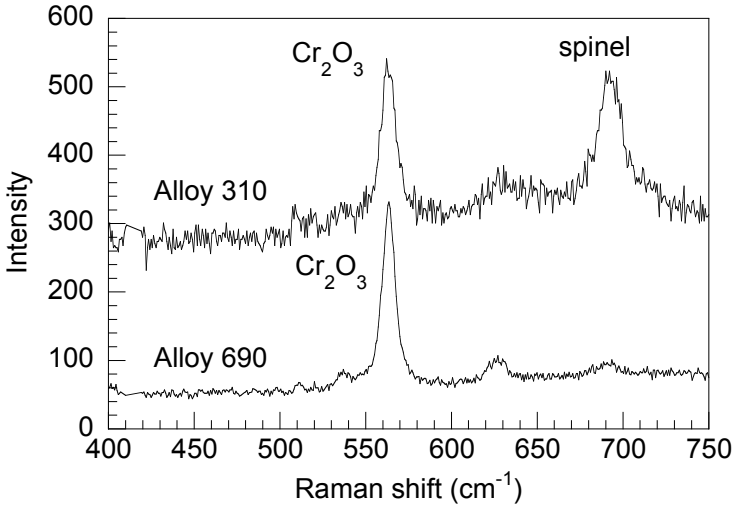

Figure 8.26. Raman spectra for Alloys 310 and 690 exposed for 300 h in Gas 13 at 593°C and 1 atm.

9. ANALYSIS OF METAL DUSTING FAILURES

Metal dusting degradation of structural metallic materials has been observed in the production of syngas, a step used in the manufacture of hydrogen, ammonia, methanol, and a variety of liquid hydrocarbons. The failures are generally observed in the temperature range of 400-700°C in complex gas environments that contain a carbon activity >>1. Further, these systems operate at elevated pressures. This condition also exacerbates metal dusting degradation, since the carbon activity increases with an increase in system pressure. During the course of this project on metal dusting, we examined failed components from two systems that were used in the production of hydrogen and ammonia.

9.1 Analysis of Bypass Line from a Syngas Plant

We received a liner material from a syngas plant, operated by Air Products and Chemicals, Inc., for the production of hydrogen. The bypass line was from a process gas boiler, which is located downstream of the reformer. The gas from the reformer outlet enters the process-gas boiler at ≈843°C (1550°F), and gas gets cooled as it flows through the boiler with an outlet temperature of ≈593°C (1100°F).

The bypass line that we analyzed was from the process gas boiler, and the flow through this section was not always maintained. Therefore, the actual service temperature or the temperature history of the line is not known. The bypass line was made of Alloy 800HT, and the gas chemistry at the reformer outlet was reported as similar to Gas 1 (Table 1.1), which had a composition of $43.8H_2$-$7.2CO$-$5.7CO_2$-$39.2H_2O$-$4.1CH_4$. The bypass line was in service for 10 years and experienced a significant attack by metal dusting.

Figure 9.1 shows several views of the bypass line, indicating failures at different locations along the pipe. The line had a helically wound wire wrap on the outer side of the pipe. These areas acted as fins and would have resulted in lower temperatures, making these regions susceptible to metal dusting degradation. It is evident from Fig. 9.1 that several of these wire-wrapped regions exhibited large holes, indicating that the material underlying the wire wrap had been completely corroded. The ruptured end of the bypass line was very thin, and corrosion rates were highest in this region.

Figure 9.2 shows the locations from which the pipe was cut for microstructural analysis. The locations A, B, and C exhibited huge pits reminiscent of those observed in Alloy 800 after long exposures in laboratory experiments. A visual examination of these regions showed that the pits had coalesced and the material had thinned away to form large holes. The uncut edges of the material in locations E and F showed substantial thinning (to razor sharp), indicating that the gas flow velocity might have some tendency to exacerbate the metal dusting attack. The cut pieces were mounted in several metallographic mounts, polished, and analyzed using SEM and EDX.

Figure 9.3 presents SEM photomicrographs of several corroded regions. The microphotograph B shows a pit that is in the early stage of formation. The oxide scale is fragmented, and the underlying pit region still has similar granular morphology to that of the

Figure 9.1. Several views of a failed bypass line from a syngas/hydrogen production plant after 10 years of service.

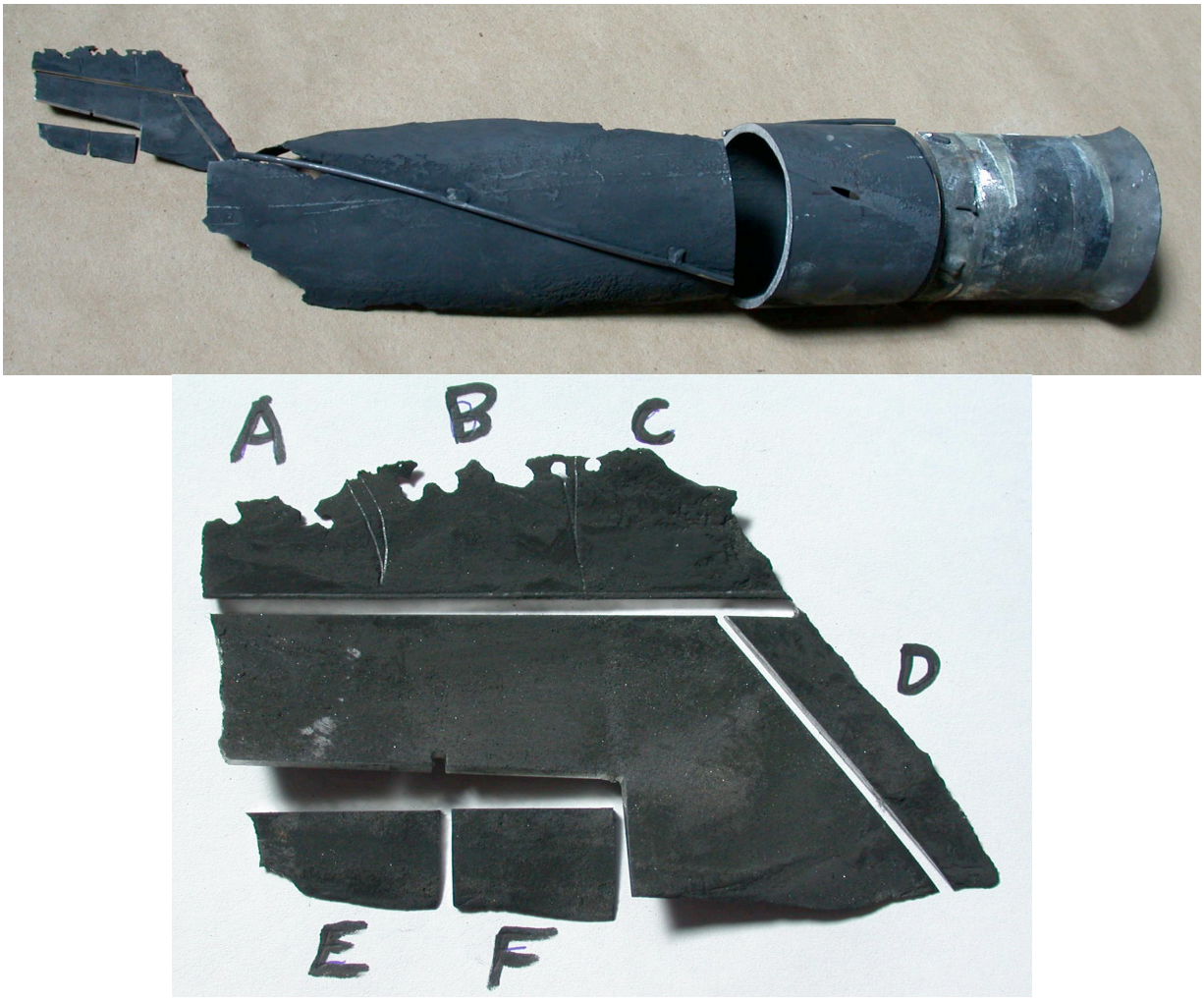

Figure 9.2 Sections of the bypass line that were used in analysis.

oxide scale. The dark area of this region showed only carbon, whereas the lighter region showed (Fe,Cr) oxide. The microphotograph D shows a pit that is fully developed, but the surrounding area is covered with (Fe,Cr) oxide, based on EDX analysis. The time for the nucleation of pits seems to vary since the observed pit sizes covered a wide range. For example, the microphotograph E shows several large pits that have grown and coalesced to cover a large area of the specimen surface, but two small pits can be seen on the top left region of the micrograph. These pits have nucleated much later in service, indicated by their size. The growth of these pits is uniformly hemispherical, indicating that the progression of the attack laterally on the surface and depth-wise into the alloy is almost similar.

Surfaces of the failed bypass line were analyzed by Raman spectroscopy. The cut specimens were ultrasonically cleaned to remove the residual carbon from the pits. Raman spectra were excited with 60 mW of 476-nm radiation from a Kr-ion laser. The scattered light was analyzed with a triple Jobin-Yvon grating spectrometer. All of our spectra were acquired in 300 sec at room temperature. Figure 9.4 shows the typical Raman spectra obtained on the specimen surface at locations near and away from the pit. The spectra showed only spinel phase

and no chromia phase. These results validate the information presented earlier that Alloy 800H is not only susceptible to metal dusting, but also that the predominant phase (especially after 10 yr service) expected is a spinel, which seems to exacerbate the degradation process.

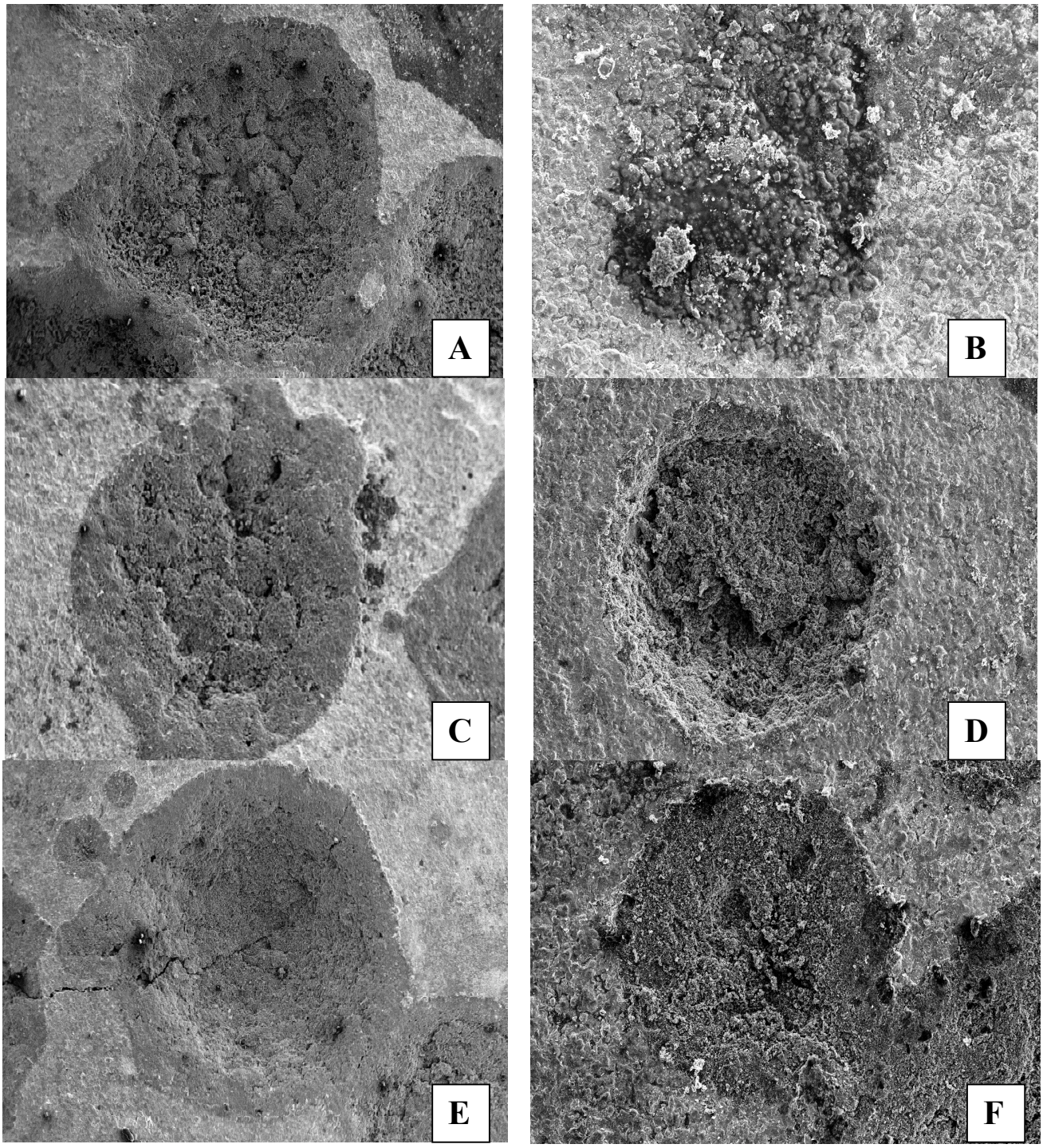

Figure 9.3. SEM photomicrographs of pit morphology in several regions of the Alloy 800H bypass line.

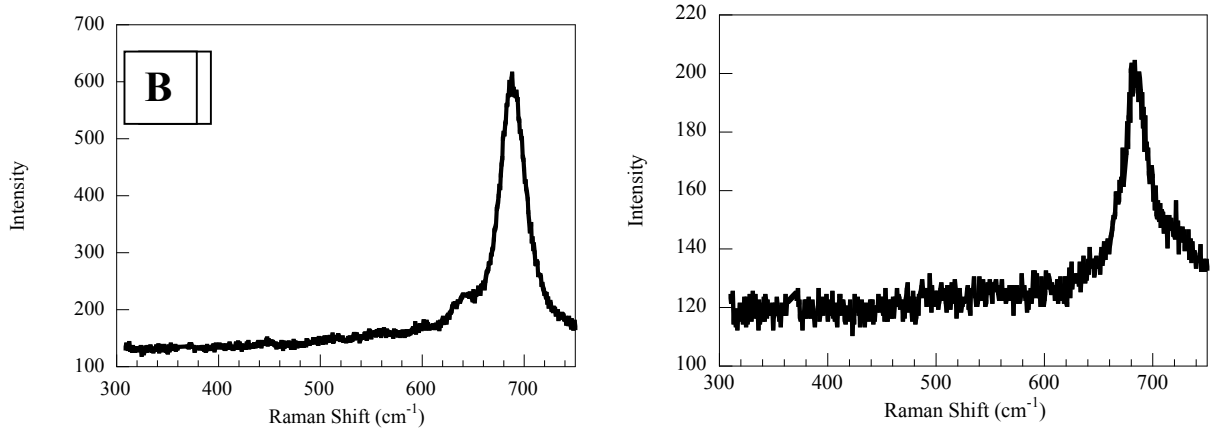

Figure 9.4. Raman spectra for Alloy 800H liner from bypass line after 10 years of service. A: away from pit; B: in the pit.

9.2 Analysis of Shroud from an Ammonia Reformer

The phenomenon of severe metal dusting – through the full thickness of affected components – was observed in the two primary waste heat boilers (WHBs) of an ammonia-producing plant (Hopewell, VA). This plant is owned and operated by Honeywell International. Its capacity now exceeds 1350 mt/d of ammonia, a 50% increase over its original design capacity. The plant was designed and constructed by M. W. Kellogg Co., and was commissioned in 1967.

For the Hopewell ammonia plant, observed metal dusting has been limited to the process outlet end (top end) of the primary waste heat boilers, and appears to have increased with production rates. The Hopewell primary WHB shell liners and tube bundles have always been replaced in less than 10 years and 9 years, respectively. The replacement decision was usually based on scheduled inspections rather than shutdown-forcing shell or tube ruptures. At the end of these periods, portions of the 800HT shrouds were no longer capable of retaining the refractory liner, resulting in a risk of shell rupture.

Sections of metal dusted parts of Alloy 800HT shroud material, which had been is service for 9 years and 2 months, were analyzed at Argonne National Laboratory (Fig. 9.5). The RA-330 baffle support rods in the associated 9 year old tube bundle suffered equally severe metal dusting, but the corresponding 1.25 Cr-0.5 Mo ferritic steel tubes did not suffer any metal dusting. The tubes, cooled by boiler feed water, operated at much lower metal temperatures. The incoming gas was at a nominal pressure of 31 atm (455 psig) and a temperature of about 978 ± 22°C (1,790 ± 40°F), while the gas outlet temperature was 477 ±17°C (890 ± 30°F). The composition of the input gas was (in vol.%) 8.5 CO-4.8 CO_2-36.3 H_2-0.14 CH_4-14.5N_2-35.6H_2O. Metal dusting attack was observed in all regions of the shroud operating in the temperature range between about 477°C and 642°C. The temperature where the most severe metal dusting occurred was at ≈477°C in and near the outlet nozzle.

Figure 9.5. Photomacrograph (plan view) of the WHB shroud section with the severest level of metal dusting. WHB shroud material: Alloy 800HT. Locations marked "C" and "A" are the spots where the 1/4-in. metal was wasted away in 9 years and 2 months of service. Location "A" and "F" are at the weldment region. Weld metal: Alloy 625.

Typical micrographs collected from the SEM studies are shown in Figs. 9.6-9.11. The details of the inside surface region at this location are shown in Figs. 9.6-9.8. Similarly, the morphology of the outside surface is shown in Figs. 9.9 and 9.11.

The specimens were also analyzed by EDX. The corrosion layers decreased in carbon and increased in Cr from the outer edge of the layer to the alloy base. The outermost layer, on the inside surface consisted of pure graphite. The next layer, going inwards, consisted of a mixture of pure graphite and chromium carbide. The next layer consisted of chromium oxide and chromium carbide, in a 50-50 mixture. The next layer consisted of chromium carbides, iron carbides, and traces of chromium oxide. The outermost layer on the alloy side was, as expected, depleted in chromium. The chromium depletion or migration followed two directions: one was toward the nearest grain boundary – where it formed a carbide – and the other was toward the outer surface, as noted above. Carbon was observed in the grain-boundary regions within the substrate alloy.

The corrosion layer on the outside surface was similar to that of the inside surface, with two major exceptions. The first concerns the absence of a graphite/carbon-rich layer, and the second, the total thickness of the layer. The outside layer, for most part, was an order of magnitude less in thickness. The morphology was also quite different. The outermost sub-layer was mostly chromium oxide. The next sub-layer was chromium-rich oxide and carbide; this was followed by another sub-layer, which was the grain-boundary affected zone. The absence of a graphite or carbon layer clearly indicated that supply of carbon was limited. In other words, the available carbon was transported/diffused inwards – through the oxide and the oxide-carbide region. The rate-limiting step appeared to be the availability of the carbon. This hypothesis seems to be reasonable, given the near stagnant nature of the gas flow on the outside surface.

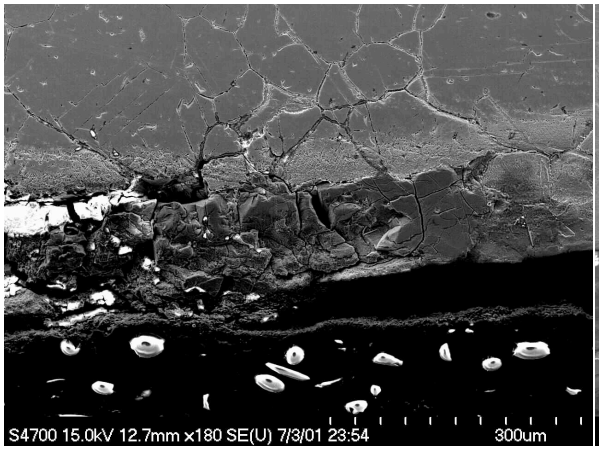

Figure 9.6. Inside surface region of the base Alloy 800HT.

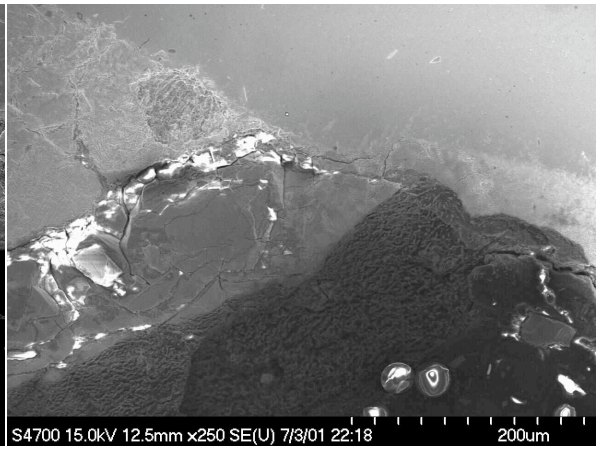

Figure 9.7. Second inside surface region of the base Alloy 800HT.

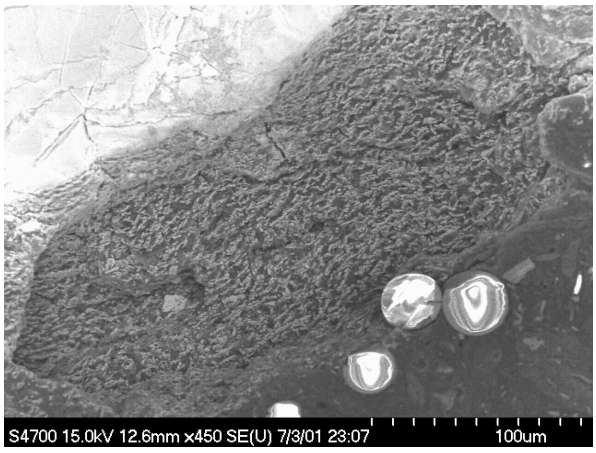

Figure 9.8. Third inside surface region of the base Alloy 800HT.

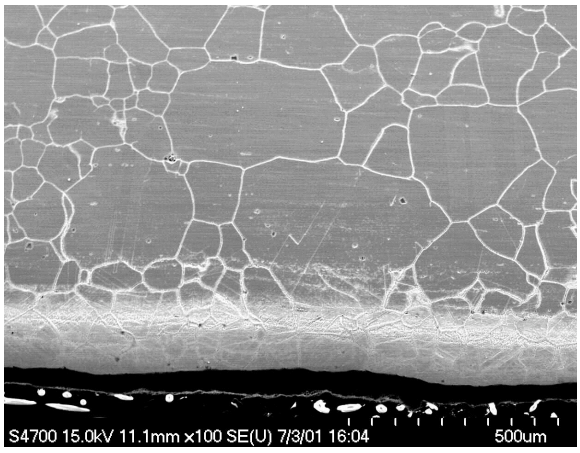

Figure 9.9. Outside surface region of the base alloy.

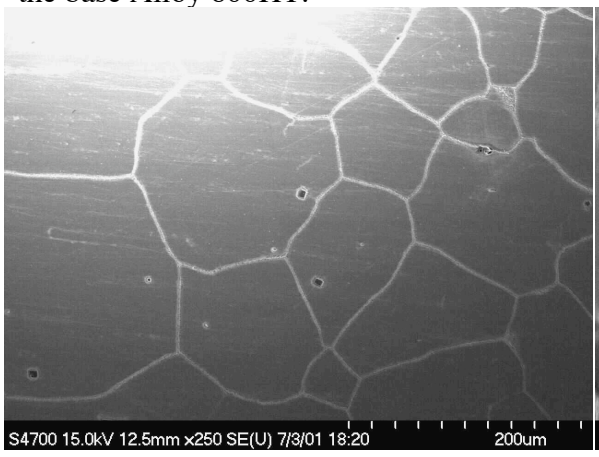

Figure 9.10. Second outside surface region of the base alloy.

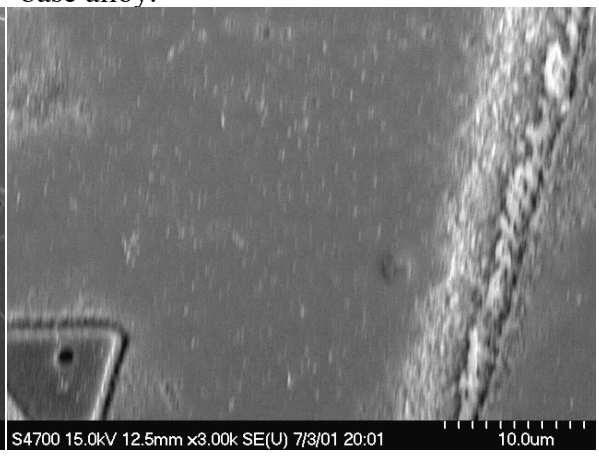

Figure 9.11. Third outside surface region of the base alloy.

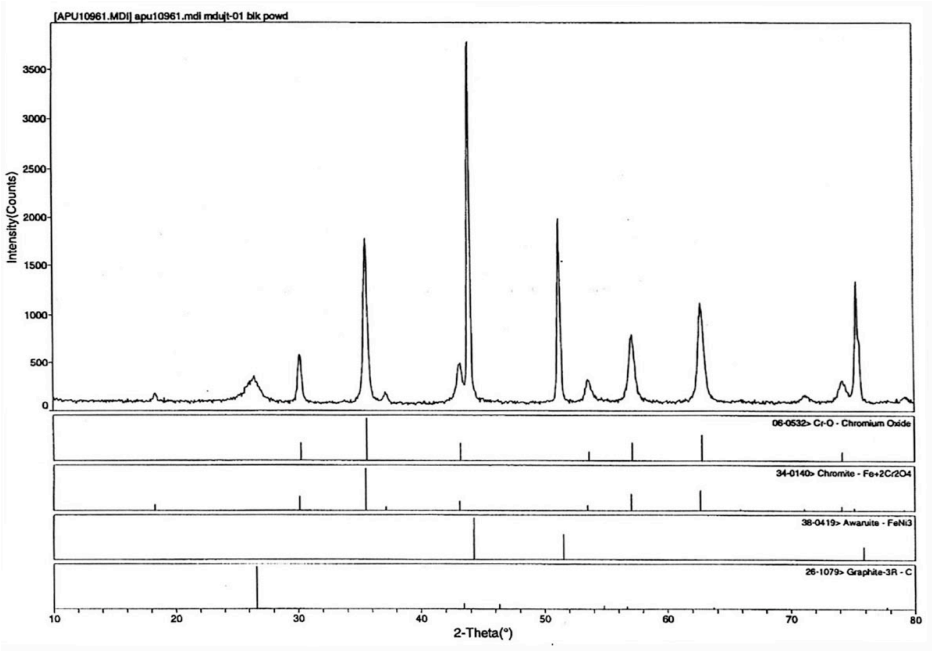

Figure 9.12. XRD analysis of the corrosion layer on the inside surface of the shroud of the WHB: intensity vs. 2θ angle.

XRD analysis was performed on the corrosion layer from the inside surface. The results are presented in Figure 9.12. The phases and compounds that were detected include: Cr_2O_3 (chromium oxide); (Fe,Cr) oxide spinel; Fe_3Ni_3 (awaruite); and C (graphite). The metal wastage rate (for Alloy 800 HT) was calculated to be equal to about 27.5 mil/yr. The weld metal wastage rate was one order of magnitude less than this rate. The weld metal (Inconel 625) corroded at a rate of about 2.5 mil/yr. The maximum metal wastage rate was found to occur at a temperature of about 677°C.

The optical and SEM photomicrographs indicated a complex metal wastage process. Chemical analyses revealed that the corrosion layer consisted of five distinct regions. The outermost region was nearly pure graphite followed by a mixture of graphite and chromium-rich oxides and carbides. A mixture of chromium and iron oxides and carbides followed this region. The final region was the alloy layer, which was depleted in chromium and mostly composed of carbide growth in the grain boundary region. However, based on this observation and coupled with general knowledge of the progression of metallic corrosion, it was reasonable to assume that the metal wastage process consisted of periodic growth of the above-noted five part corrosion layer, followed by mechanical breaking/flaking caused by cyclical thermal and mechanical stresses. Once the total corrosion layer reached a thickness of about 150 μm, it became mechanically unstable and broke off. A fresh layer then formed which also broke off after reaching about 150 μm in thickness. The value of 150 μm is reasonable because we did not find any region with corrosion layer >150 μm anywhere on the failed shroud piece, even though the total metal wastage after 9 years and 2 months amounted to about 6.35 mm.

10. SUMMARY

The deposition of carbon from cabonaceous gaseous environments is prevalent in many chemical and petrochemical processes, such as reforming systems, syngas production systems, iron reduction plants, and others. An extensive program has been conducted at Argonne National Laboratory to establish the mechanisms for metal dusting degradation in metallic materials exposed to carbon-bearing gaseous environments, to identify the key parameters that influence the onset of metal dusting and propagation of degradation, to establish the metal wastage under a variety of exposure conditions, to characterize the morphology of degradation using a wide variety of analytical techniques, and to assess the effect of alloy chemistry and the extent of metal dusting.

Several conclusions can be drawn from the study:

- One of the major consequences of carbon deposition is the degradation of structural materials by a phenomenon known as "metal dusting." There are two major issues of importance in metal dusting. First is formation of carbon and subsequent deposition of carbon on metallic materials. Second is the initiation of metal dusting in the alloy and subsequent propagation of the degradation. The first is influenced by a_C in the gas mixture and availability of the catalytic surface for carbon-producing reactions to proceed. There may be a threshold in a_C (>>1) for carbon deposition. Metal dusting of the alloy in the reformer environments is determined by a competition between the oxide scale development and access of the virgin metal surface to the carbon deposit.

- A new metal dusting mechanism was proposed in this study. Mechanisms for degradation of both Fe- and Ni-base alloys are related to the catalytic crystallization of carbon that deposits from the gaseous environment. The only difference is that iron carbide acts as a catalyst in Fe-base alloys, whereas nickel metal instead of nickel carbide acts as a catalyst in Ni-base alloys. To achieve good crystallinity, carbon dissolves, diffuses through, and precipitates at defects of iron carbide or nickel metal. The accumulation of carbon leads to separation of carbide or nickel grains into nano-size particles. The growth of carbon nano-filaments is the final step in metal dusting. The free energy difference between poorly and well-crystallized carbon is the driving force for both metal dusting and the growth of carbon nano-filaments. We believe that the proposed mechanism can explain more of the experimental observations made on Fe- and Ni-base alloys subjected to metal dusting degradation.

- We have tested alloys at 482, 593, and 704°C. The metal dusting rate at 593°C is the highest. However, further study is needed to establish the temperature dependence of metal-dusting rates in different alloys. It is also necessary to relate the metal wastage rates to the carbon activity in the exposure environment and system pressure, in addition to temperature.

- The local nature of dusting (initiated by pits on the alloy surface) on structural alloys shows that defects in the oxide scales play a large role in initiation. Oxide scaling may not occur if a_C is >>1 and/or if the H_2O content in the environment is very low.

Laboratory experiments have clearly indicated the effect of gas chemistry (in particular H_2O content) in the scaling, carbon deposition, and dusting initiation. It is evident that the environment in reformers is high enough in pO_2 that a Cr-rich alloy can develop a chromia scale (given enough exposure time) before carbon deposition. The presence of an oxide scale may not prevent metal dusting but can delay its initiation, thereby slowing the overall attack.

- Raman spectra show the existence of spinel, Cr_2O_3, and disordered chromium oxide in the scale grown on high-chromium Fe-base alloys. All three phases act, to different degree, as protective layers to prevent alloys from metal dusting corrosion. The spinel phase is not as stable as Cr_2O_3. The deposited carbon could reduce it, and metal dusting corrosion would initiate from the reduced defects.

- Phase composition of the oxide scale is important in the process of metal dusting corrosion. Cr_2O_3 is better than spinel at resisting metal dusting since spinel can be reduced. If alloys can generate more Cr_2O_3 and less spinel on the surface, their abilities to resist metal dusting will increase. Therefore, alloys with more Cr and less iron content performed well in a carburizing atmosphere. Phase composition of oxide scale changes with exposure time. Spinel content increases and chromium oxide content decreases with exposure time. Therefore, alloys are easy to be attacked by metal dusting after long exposures since the spinel content increases.

- Metal dusting degradation involves two steps; the incubation period and the propagation. The incubation period is determined by the carbon activity in the gas phase, alloy chemistry, system pressure, and probably the exposure temperature. For the same exposure conditions, the incubation period for the onset of metal dusting is significantly greater for the Ni-base alloys when compared with that for Fe-base alloys.

- Higher carbon activity may increase the metal loss rate since higher carbon activity provides higher driving force to form highly disordered carbon on the surface of metal.

- High system pressure not only increases the carbon activity but also seems to accelerate the carbon transport into the alloy and to reduce the incubation time for onset of metal dusting.

- Both aluminum and silicon additions increased the ability of alloys to resist metal dusting. However, silicon addition failed to protect alloys from metal dusting at high pressure, although it was beneficial in the 1-atm pressure tests. High Cr content in alloys is necessary but not sufficient to resist metal dusting. Iron content (especially in Ni-base alloy) is detrimental and should be maintained as low as possible to extend the life of the alloy. Cobalt addition is not beneficial to resist metal dusting.

- MA956, APMT, and 4C54 are the best three Fe-base alloys to resist metal dusting. Two of the three alloys contain Al (4.5% in MA956 and 4.9% in APMT). Alloy 4C54 contains the highest Cr level of 26.7%.

- Ni-base alloys performed better than that of Fe-base alloys when exposed in similar atmospheres. Among the Ni-base materials, Alloy 693 was the best. This performance can be attributed to its high Cr and Al contents. Alloy 602CA was good in most of the tests, but it was attacked in high-carbon-activity Gas 17.

- Surface modification by preoxidation and/or coatings and alternative materials are being examined at ANL to alleviate the metal dusting problem. Oxide coatings have the advantage in that they can minimize carbon-producing reactions (by reducing the availability of catalytic surface) and can also act as a barrier to minimize carbon ingress and pitting of the substrate alloy. Preliminary tests showed beneficial effect, but long-term tests are needed to substantiate the results.

- We have examined in-situ development of oxide scales as a means to prevent or minimize metal dusting attack. Preliminary tests showed that the performance of pre-oxidized samples was worse than that of the samples without pre-oxidation. There was more spinel phase on the surface of alloys that were pre-oxidized. The spinel phase, especially if it contained a high Fe content, was detrimental and led to an increase in metal dusting corrosion.

ACKNOWLEDGEMENTS

This work was sponsored by the U.S. Department of Energy, Office of Industrial Technologies. Dr. Charles Sorrell was the program manager for the project. H. L. Craig, Jr. of MTI and K. Baumert of Air Products and Chemicals, Inc. and others were involved in the steering committee for the project. Haynes International, AvestaPolarit, Sandvik Steel, Special Metals, Allegheny Ludlum, and Krupp VDM supplied specimens of various alloys. Alon Surface Technologies supplied specimens with pack-diffusion layers.

REFERENCES

Abrahamson, J., 1973, Carbon 11, 337.

Al-Jishi, R., 1982, Phys. Rev. B, 26, 4514.

Austin, A. E., and W. A. Hedden, 1956, Ind. Eng. Chem., 46, 1520.

Baker, R. T. K., M. A. Barber, F. S. Feates, and R. J. Waite, 1972, J. Catal., 26, 51.

Bermejo, E., T. Becue, C. Lacour, and M. Quarton, 1997, Powder Technology, 94, 29.

Blayden, H. E., H. L. Riley, and A. Taylor, 1940, J. Am. Chem. Soc., 62, 180.

C. Liu, Y. Y. Fan, M. Liu, H. T. Cong, H. M. Cheng, and M. S. Dresselhaus, 1999, Science, 286, 1127.

Chun, C. M., T. A. Ramanarayannan, and J. D. Murnford, 1999, Mat. Corros., 50, 634.

Deheer, W. A., A. Chatelain, and D. Ugarte, 2001, Science, 270, 1179.

Dillon R. O., and J. A. Woollam, 1984, Phys. Rev. B, 29, 3482.

Farrow, R. L., R. E. Benner, A. S. Nagelberg, and P. L. Mattern, 1980, Thin Solid Film, 73, 353.

Franklin, R. E., 1951, Acta Cryst., 4, 253.

Grabke, H. J., 1998, Mater. and Corros., 49, 303.

Grabke, H. J., 2000, Mater. High Temp. 17, 483.

Grabke, H. J., and E. M. Muller-Lorenz, 1998, Mater. Corrosion, 49, 317.

Grabke, H. J., R. Krajak, and E. M. Muller-Lorenz, 1993, Werkst. Korros. 44, 89.

Grabke, H. J., R. Krajak, E. M. Muller-Lorenz, and S. Strauss, 1996, Mater. Corrosion, 47, 495.

Grabke, H. J., R. Krajak, E. M. Muller-Lorenz, and S. Strauss, 1998, Mater. Corrosion, 49, 328.

Hochman, R. F., 1977, Proc. Symp. Properties of High-Temperature Alloys with Emphasis on Environmental Effects, Z. A. Foroulis and F. S. Pettit, eds., The Electrochemical Society, Pennington, NJ, p. 715.

Iijima, S., 1991, Nature, 354, 56.

Kinney, C. R., 1956, Proc. Conference on Carbon, U. of Buffalo, p. 83.

Knight, D. S., and W. B. White, 1989, J. Mater. Res., 4, 385.

Krebs, H., 1968, Fundamentals of Inorganic Crystal Chemistry, McGraw-Hill, London, p. 150.

Lee, M., and G. Simkovich, 1988, Metall. Trans., 19A, 2115.

Lefrancois, P. A., and W. B. Hoyt, 1963, Corrosion 19, 360t.

Levi, T. P., N. Briggs, I. E. Minchington, and C. W. Thomas, 2002, Mater. Corros., 53, 239.

Lewis, D. C., M. A. Frisch, and J. L. Margrave, 1965, Carbon, 2, 431.

Lide, D. R., 1999, CRC Handbook of Chemistry and Physics, 80th Ed., CRC Press, Boca Raton, LA, P12-14.

Maier, M., J. F. Norton, and P. D. Frampton, 1998, Mater. Corros., 49, 330.

Maimer, M., and J. F. Norton, 1999, Mater. Corros., 50, 640.

Maroni, V. A., C. A. Melendres, T. F. Kassner, R. Kumar, and S. Siegel, 1990, J. Nucl. Mater., 172, 13.

McCarty, K. F., and D. R. Boehme, 1989, J. Solid State Chem., 79, 19.

Nakamizo, M., H. Honda, and M. Inagaki, 1978, Carbon, 16, 281.

Nakamizo, M., H. Honda, M. Inagaki, and Y. Hishiyama, 1977, Carbon, 15, 295.

Natesan, K., 2002, Study of Metal Dusting Phenomenon and Development of Materials Resistant to Metal Dusting: Annual Report, Argonne National Laboratory Report, ANL-02/05.

Natesan, K., Z. Zeng, V. A. Maroni, W. K. Soppet, and D. L. Rink, 2004, Proc. Intl. Workshop on Metal Dusting, Sept. 24-26, 2001, in press.

Natesan, K., A. Purohit, D. L. Rink, and W. Salot, 2004, Proc. Intl. Workshop on Metal Dusting, Sept. 24-26, 2001, in press.

Nemanich, R. J. and Solin, S. A., 1979, Phys. Rev. B, 20, 392.

Peacock, T. E., 1960, J. Chem. Phys. 57, 844.

Pippel, E., J. Woltersdof, H. J. Grabke, and S. Strauss, 1995, Steel Research, 66, 217.

Renusch, D., B. Veal, K. Natesan, and M. Grimsditch, 1996, Oxid. Met., 46, 365.

Rostrup-Neilson, J. R., 1975, Steam Reforming Catalysts, Danish Technical Press, Inc., Copenhagen.

Schaeffer, W. D., W. R. Smith, and M. H. Polley, 1953, Ind. Eng. Chem., 45, 1721.

Strauss, S., and H. K. Grabke, 1998, Materials and Corrosion, 49, 321.

Thibeau, R. J., C. W. Brown, and R. H. Heidersbach, 1978, Appl. Spec. 32, 532.

Thierry, D., D. Persson, C. Leygraf, D. Delichere, S. Joiret, C. Pallotta, and A. Hugot-Le Goff, 1988, J. Electrochem. Soc. 135, 305.

Tuinstra, F., and J. L. Koenig, 1970, J. Chem. Phy, 53, 1126.

Van Vuuren, C. P. J., J. J. Bodenstein, M. Sciarone, and P. Kestens, 1992, Proc. of 6th Inter. Ferroalloys Congress, Cape Town, Volume 1, Johannesburg, SAIMM, pp. 51-55.

Vidano, R., and D. B. Fischbach, 1978, J. Amer. Ceram. Soc. 61, 13.

Wei, Q., E. Pippel, J. Woltersdorf, S. Strauss, and H. J. Grabke, 2000, Mater. Corrosion, 51, 652.

Yang, R. T., and J. P. Chen, 1989, J. Catal. 115, 52.

Zeng, Z., K. Natesan, and V. A. Maroni, 2004, Proc. Intl. Workshop on Metal Dusting, Sept. 24-26, 2001, in press.

Zeng, Z., and K. Natesan, 2003, Chemistry of Materials, 15, 872.

DISTRIBUTION LIST FOR ANL-03/33

Internal

V. A. Maroni
K. Natesan (30)
R. B. Poeppel
W. W. Schertz
W. J. Shack
Z. Zeng
TIS Files

External

DOE/OSTI, for distribution (2)
ANL-E Library
ANL-W Library
S. Dillich, DOE Office of Industrial Technologies, Washington, DC 20585
L. Elgin, Materials Technology Institute, St. Louis, MO 63141 (25 copies)
R. Jain, DOE Office of Industrial Technologies, Washington, DC 20585
D. Ozokwelu, DOE Office of Industrial Technologies, Washington, DC 20585
C. Russomanno, DOE Office of Industrial Technologies, Washington, DC 20585
D. Salem, DOE Office of Industrial Technologies, Washington, DC 20585
P. Scheihing, DOE Office of Industrial Technologies, Washington, DC 20585
C. Sorrell, DOE Office of Industrial Technologies, Washington, DC 20585
B. Valentine, DOE Office of Industrial Technologies, Washington, DC 20585